Imperial College London
Department of Earth Science and Engineering

Investigation of Hydrogen based Redox Flow Batteries

Harini Minoka Hewa Dewage

Submitted in part fulfilment of the requirements
for the degree of Doctor of Philosophy at
Imperial College London, June 2016

I hereby declare that this thesis and the work reported herein was composed by and originated entirely from me. Information derived from the published and unpublished work of others has been acknowledged in the text and references are given in the list of sources.

Harini Minoka Hewa Dewage (2016)

Abstract

Large scale energy storage is crucial for effective integration of intermittent renewable energy sources such as solar and wind. Redox flow batteries are a promising grid scale energy storage technology and understanding their losses is key to further optimisation. This thesis investigates a novel class of RFBs which utilises a conventional liquid based cathode in combination with a hydrogen anode, similar to that used in a Proton Exchange Membrane Fuel Cell (PEMFC).

Firstly, a new Reference Electrode (RE) positioning method was developed in order to decouple anode and cathode processes in RFBs. Unlike other methods presented in literature, the approach described here can generate reliable measurements, without noticeably affecting the performance of the cell. This set-up was used to further understand the Regenerative Hydrogen-Vanadium Fuel Cell (RHVFC), which revealed that cathode diffusion and ohmic losses were the limiting processes of this cell. Catholyte crossover was also observed, which resulted in vanadium adsorption onto the catalyst of the hydrogen electrode.

Secondly, the feasibility of a novel Regenerative Hydrogen-Cerium Fuel Cell (RHCFC) was validated. Using the same RE set-up, further investigation was carried out on an optimised cell, which yielded energy efficiencies in the range of 70 to 85 % when charging/discharging at current densities up to 20 $\mathrm{mA\,cm^{-2}}$. A combination of electrochemical impedance spectroscopy and polarisation tests allowed the decoupling of many of the processes occurring at each electrode. In addition, imaging and surface characterisation techniques revealed the presence of carbon deposits on the fresh electrode surface, which increased with use; the nature of these deposits and their implication on cell operation will be the subject of further investigation. Finally, it was established that the performance of the cell is currently limited by the cerium cathode, which suffers from poor kinetics and large diffusion losses.

Acknowledgements

First and foremost, I would like to express my gratitude to my main supervisor Prof. Nigel Brandon for giving me the opportunity and the freedom to lead my project according to my preferences. I would also like to thank him for his support, advice and patience especially when it comes to my written work! His experience and diplomacy skills have taught me over the years more than I could have wished for.

I would also like to extend my gratitude to my associate supervisor Dr Vladimir Yufit. His extreme kindness and helpfulness largely makes up for his comical pessimism expressed at times. His wealth of ideas have always sparked interesting conversations and has always motivated me to pursue my own. His electrochemistry knowledge is a gift and a curse when it came to my constant pestering with questions.

Over the last three years, Billy Wu has been a friend, an unofficial supervisor and my favourite nemesis. I would struggle to overstate how grateful I am for his advice in and out of the lab and for giving me fantastic opportunities such as teaching, supervising and entering health threatening sport challenges. Supervising Anthony Tsoi and Gwen Owen-Jones has been a highlight of my PhD. Hopefully I have taught them as much as they have taught me. I would also like to thank Fred Marquis and Guillermo Rein for their friendliness and support when it came to demonstrating ME2 labs for the past three years.

The Electrochemical Science and Engineering group has certainly offered great entertainment and a friendly environment to work in over the past couple of years. Great laughter has been shared with my fellow experimentalists from the group and outside: Max Naylor-Marlow, Alex Lama-Noujaim, Dany Nir and Xinhua Liu; making LG27 the brightest place at Imperial despite the lack of windows.

Ecaterina Ware and Ignacio Villar Garcia have kindly helped me with SEM imaging and XPS analysis of my samples and I look forward to working more with them in the future.

My thanks go to Samuel Cooper for lighting up my life with his charm and humour and whose scientific curiosity always inspire me to become a better researcher. An additional thanks for humouring me during this writing process and creating a thesis template that saved me many hours of work.

My dear friends Louise Eber, Victoire de Marcillac, Gabriel de Bousquet, Josh McNicoll, Bart Nutton and Robert Schlee for entertaining me the last few years and lovingly pretending they were interested when I would ramble about my work.

Finally, words cannot describe how grateful I am to my parents Sunil and Roshini for embracing my achievements and failures with love. Without their emotional and financial generosity I would have never got this far. Lastly to my beautiful late grandmother Somawathie, a woman ahead of her times, who was a sister, a friend and a third parent to me when growing up.

To my parents, Sunil and Roshini.

With four parameters I can fit an elephant, and with five I can make him wiggle his trunk.

- John von Neumann

Contents

List of Tables

List of Figures

Nomenclature

A	Active surface area [cm^2]
C_O	Oxidant concentration [M]
C_R	Reductant concentration [M]
$Diff$	Diffusion
E	Potential [V]
P	Power[W]
E_0	Standard cell potential [V]
I	Current [A]
N	Number of moles of active species
Q	Capacity [Ah]
R	Resistance [Ω]
S	Series
dl	Double layer
equ	Equilibrium
f	Frequency [Hz]
j	Current density [$mA\,cm^{-2}$]
j_0	Exchange current density [$mA\,cm^{-2}$]
j_l	Limiting current [A]
n	Number of electrons
t	Time [s]

Greek Symbols

α_a	Anodic transfer coefficient

α_c Cathodic transfer coefficient

η Overpotential

ω Angular frequency

ϕ Phase shift

List of Abbreviations

AC Alternating Current

CCS Carbon Capture Storage

CT Charge Transfer

CV Cyclic Voltammetry

DC Direct Current

DHE Dynamic Hydrogen Electrode

EDA Energy Development Association

EDX Energy Dispersive X-ray Spectroscopy

EIS Electrochemical Impedance Spectroscopy

GDL Gas Diffusion Layer

GHG Greenhouse Gases Emissions

LDL Liquid Diffusion Layer

MEA Membrane Electrode Assembly

NMR Nuclear Magnetic Resonance

OCV Open Circuit Voltage

PEMFC Proton Exchange Membrane Fuel Cell

PFSA Perfluorosulfonic acid

PTFE Polytetrafluoroethylene

PVDF Polyvinylidene fluoride

RE Reference Electrode

RFB Redox Flow Batterie

RHCFC Regenerative Hydrogen-Cerium Fuel Cell

RHVFC Regenerative Hydrogen-Vanadium Fuel Cell

SCHE Self-Contained Hydrogen Electrode

SEI Sumitomo Electric Industries

SEM Secondary Electron Microscopy

SHE Standard Hydrogen Electrode

SS Stainless Steel

UK United Kingdom

USA United States of America

UV-vis Ultraviolet-visible

VRB All Vanadium Battery

XPS X-ray photoelectron spectroscopy

Chapter 1

Introduction

1.1 Overview

Projections have been made that the world energy consumption will grow by 56 % between 2010 and 2040.[1] Currently 80 % of the worlds energy is generated from fossil fuels and its combustion contributes to 62 % of the global greenhouse gases emissions (GHG), the main cause for global warming.[2] Climate change being one of the greatest challenge of the century, the scientific community and governmental authorities are attempting to move toward renewable energy generation by decarbonising their electricity grids.

Renewable energy sources such as solar and wind have been deployed across the world. In 2012, a total of 318 and 102 GW of wind and solar power capacity was installed respectively.[3] However these sources of energy are intermittent. In order to implement smart-grids in the future, large scale energy storage has become vital.[4] A comparison between different energy pathways to 2050, including grassroots, nuclear and carbon capture storage (CCS), has shown that regardless of the scenario taking place the value of storage is not negligible.[4] Indeed having any amount of storage installed means that an equivalent amount of capacity does not have to be generated using conventional energy supply.[4] Strbac *et al.* identified that in 2050, 10 GW of bulk storage installed would lead to £8 bn/year savings for a grassroots pathway, £1 bn/year for a nuclear pathway and £0.2 bn/year for a CCS pathway.[4] Energy storage has the potential to be used for renewables storage but also for peak shaving, short term system regulation and

Table 1.1: Storage time required for different applications in the grid.[6]

Storage time	Application
milliseconds to seconds	quality of supply
seconds to minutes	frequency stabilisation
minutes to hours	peak load displacement
hours to weeks	long term storage
months	seasonal storage

load levelling.[5] The required storage time can vary depending on the on the application in the grid as detailed in Table 1.1. Several types of energy storage exist: mechanical, kinetic, thermal and electrochemical. Pumped hydro is currently the main form of installed grid scale storage,[3] but future growth in its capacity is often limited by the availability of suitable sites.

Electrochemical energy storage offers a wide range of technologies: e.g. supercapacitors, lithium ion batteries, lead acid batteries, redox flow batteries, etc.[7] These offer many advantages such as geographic location independence, short response time, modular power, high efficiencies (>80 %) and low environmental footprint.[7,8] Malhotra *et al.* have discussed the spread of energy storage using batteries by compiling databases from various organisations and the split of these projects by technology is displayed in Fig. 1.1.[9] In early 2015, there were 1279 energy storage installations in the world out of which 612 were using battery technology across 42 countries.[9] As it can be observed, currently lithium ion batteries represent over half of these projects, possibly due to their ability to deliver for both energy and power.[9] Redox flow batteries (RFBs), which is the topic of interest of this work, comes in third place where its appeal is more for energy demanding applications rather than power.

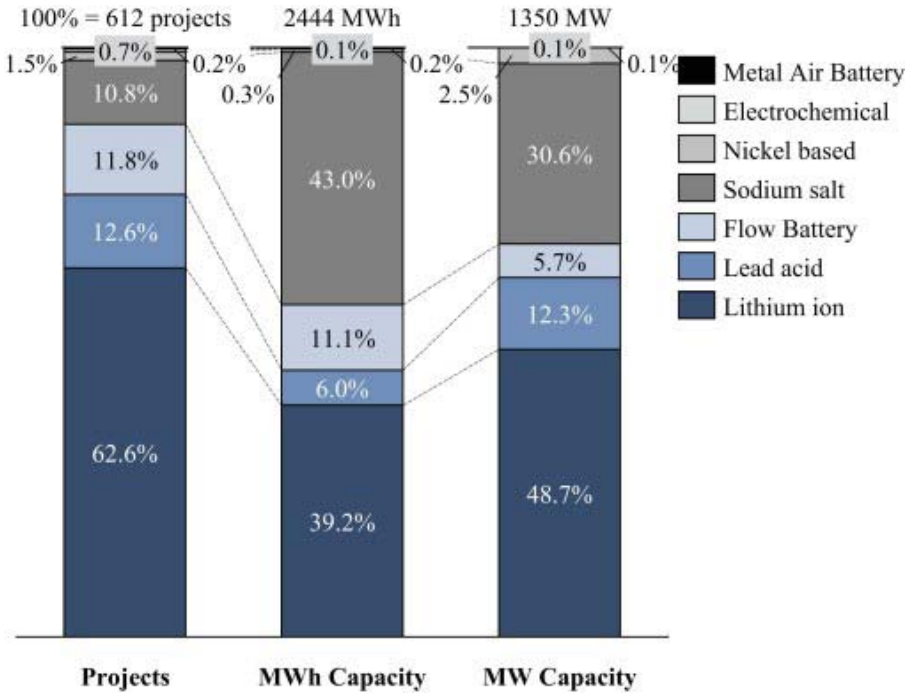

Figure 1.1: Splits of the worldwide energy storage projects by technology. Reproduced from[9] with permission from Elsevier.

This work is focussed on the understanding and development of a novel class of RFBs that will be further described in the following Chapters.

1.2 Motivation

The aim of this work is to investigate hydrogen based redox flow batteries, more specifically a novel Regenerative Hydrogen Vanadium Fuel Cell (RHVFC) and Regenerative Hydrogen Cerium Fuel Cell (RHCFC). This work seeks to understand further the RHVFC developed initially by Yufit *et al.* by identifying the processes and losses occurring in the cell.[10] A novel reference electrode positioning method has been developed in order to decouple anode and cathode processes in the RHVFC. Additionally, the RHCFC was developed in this study, and similar characterisation work was carried out. This Chapter presents the energy debate and the need for energy storage which allows to contextualise the work that will follow. Chapter 2 offers an overview on RFB technology and explains where the work of this thesis fits into the literature. The fundamental theory necessary to understand RFBs is also discussed followed by a short discussion of the characterisation techniques used in this work. Chapter 3 details

the general experimental methods used throughout this work. Other specific protocols will be discussed in the relevant Chapters. Chapter 4 introduces the development of an alternative reference electrode positioning method, inspired from that presented by Hinds *et al.* for a Proton Exchange Membrane Fuel Cell (PEMFC).[11] This method has been adapted for RFB applications, and unlike other options available, it does not hinder the operation of the cell, nor the validity of the measurements. Chapter 5 presents initial work done on the RHVFC and the challenges faced with cell design and characterisation. Limitations of whole cell measurements are described, highlighting the necessity of decoupling the cathode and anode performance during cell operation. The second half of the Chapter presents these decoupled measurements using the alternative reference electrode positioning method presented in Chapter 4. Chapter 6 introduces the development of the RHCFC and the results obtained with a proof-of-concept cell. Moreover a further study on the RHCFC with decoupled measurements is discussed offering deeper insights into the RHCFC operation. Finally Chapter 7 presents the conclusions of this thesis and suggestions for the continuation of this work.

References

[1] U.S. Energy Information Admnistration and Office of Integrated and International Energy Analysis, *International Energy Outlook 2014*, 2014.

[2] M. Höök and X. Tang, *Energy Policy*, 2013, **52**, 797–809.

[3] S. Rehman, L. M. Al-Hadhrami and M. M. Alam, *Renewable and Sustainable Energy Reviews*, 2015, **44**, 586–598.

[4] G. Strbac, M. Aunedi, D. Pudjianto, P. Djapic and F. Teng, *Strategic Assessment of the Role and Value of Energy Storage Systems in the UK Low Carbon Energy Future Report for Carbon Trust*, Imperial College London Technical Report June, 2012.

[5] R. Dell, *Journal of Power Sources*, 2001, **100**, 2–17.

[6] J. Noack, N. Roznyatovskaya, T. Herr and P. Fischer, *Angewandte Chemie (International ed. in English)*, 2015, **54**, 9776–809.

[7] M. Skyllas-Kazacos, M. H. Chakrabarti, S. a. Hajimolana, F. S. Mjalli and M. Saleem, *Journal of The Electrochemical Society*, 2011, **158**, R55.

[8] B. Dunn, H. Kamath and J.-M. Tarascon, *Science (New York, N.Y.)*, 2011, **334**, 928–35.

[9] A. Malhotra, B. Battke, M. Beuse, A. Stephan and T. Schmidt, *Renewable and Sustainable Energy Reviews*, 2016, **56**, 705–721.

[10] V. Yufit, B. Hale, M. Matian, P. Mazur and N. P. Brandon, *Journal of the Electrochemical Society*, 2013, **160**, A856–A861.

[11] G. Hinds and E. Brightman, *Electrochemistry Communications*, 2012, **17**, 26–29.

Chapter 2

Introduction to Redox Flow Batteries

2.1 Types of RFBs

A RFB, also referred to as a regenerative fuel cell, exploits two soluble redox couples stored in separate external electrolyte tanks to the energy converting device (single cell or stack) as depicted in Fig. 2.1. During charge/discharge, each electrolyte is pumped through its respective half-cell where an oxidation/reduction reaction takes place in order to release/store energy. These half-cells are separated by an ion exchange membrane only allowing selective ions to pass through, while electrons are forced to pass through an external circuit. The negative and positive electrodes are respectively the anode and cathode only during discharge. However they will often be referred to as such for a given system.

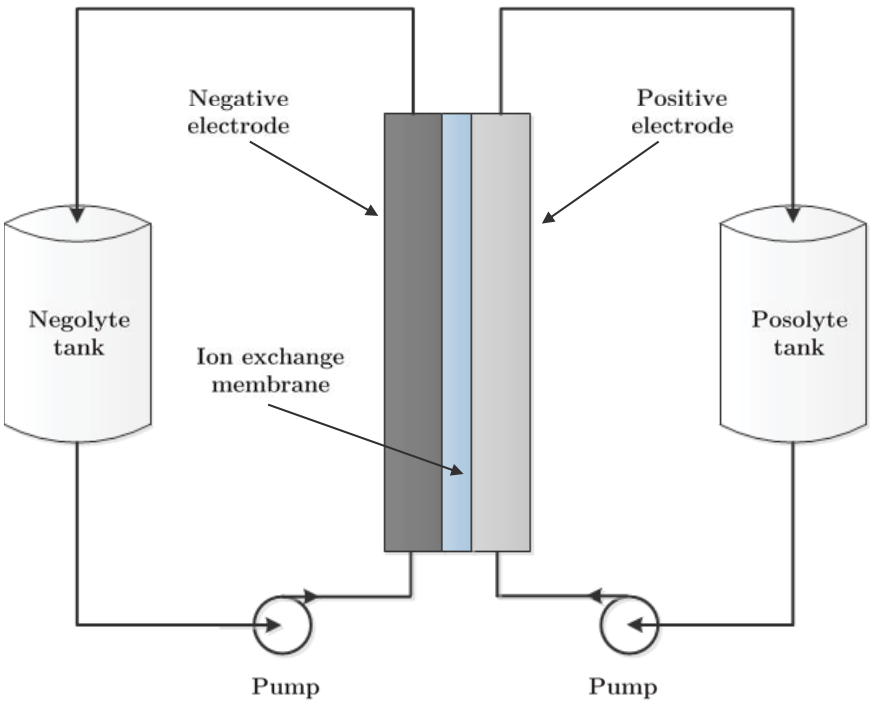

Figure 2.1: Schematic illustration of an RFB.

The first RFB, an iron/chromium (Fe/Cr) system was developed by Thaller at the National Aeronautics and Space Administration (NASA) in the 1970s, focussed on bulk energy storage, peak shaving, load levelling, and combination with intermittent energy sources (ie.: solar power, wind power).[1,2] In parallel, a zinc-chlorine (Zn/Cl) RFB was researched by the Energy Development Association (EDA) however no pilot plant to test the concept was built.[3,4] Currently out of the various RFBs chemistries available, the two most popular commercialised systems are the all-vanadium (VRB) and zinc bromine (Zn/Br).[5]

Since 1988, when the first VRB was developed by Skyllas-Kazacos *et al.*, its performance has been improved through various means: electrode and membrane materials, modified electrolytes, and better cell design.[6–10] Utilising all four oxidation states of vanadium, having a V(II)/V(III) and a V(IV)/V(V) redox couples on the anode and cathode respectively, offers the major benefit of not suffering irreversible capacity losses through cross-contamination, unlike many other RFBs.[6,7] Although some electrolyte can crossover to the opposite electrode, by regularly

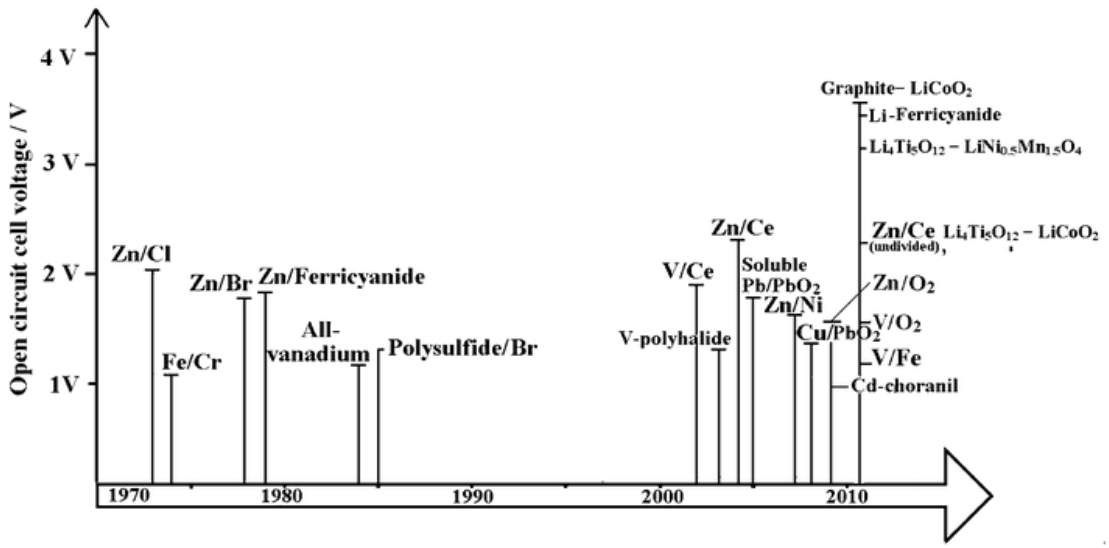

Figure 2.2: Timeline of the development of redox couples in RFB research. Reproduced from[4] with permission from the Royal Society of Chemistry.

mixing both electrolytes, the full initial capacity of the VRB can be retrieved.[5] Moreover, high performance has been reported in the literature with peak power density up to 2588 mW cm^{-2} under some conditions.[11]

The Zn/Br system is categorised as a hybrid RFB, which refers to all systems where at least one half-cell involves the use of either gaseous or deposited solid species.[12] At the cathode, bromine ions are transformed into bromine and back, whereas at the anode zinc metal is dissolved and redeposited.[13] A key advantage of this RFB is its high cell potential and energy density (1.82 V and 65-75 W h kg^{-1}), compared to the VRB which operates at 1.26 V and has a much lower energy density of 25-30 W h kg^{-1}.[14]

A plethora of different redox couple combinations has been investigated in the past 40 years as displayed in Fig. 2.2. Due to the popularity of the VRB, many vanadium based chemistries have been tested and each present some benefits as explained in Table 2.1.

From Fig. 2.2, it can be noted that since the early 2000s, interest has been sparked in redox combinations that deliver higher open circuit potential, thus potentially delivering higher energy density. Moreover a new class of lithium based RFBs have appeared in recent years associating the high energy density of lithium ion batteries and the energy capacity and power flexibility offered by RFBs.[14,20] An initial system presenting a Li-metal anode and an aqueous catholyte was developed in parallel by Goodenough and Zhou's groups.[21,22] Furthermore, a novel semi-

Table 2.1: Details of vanadium based RFBs.[15–19]

Chemistry	**Year**	**Benefit**
V/Ce	2002	Higher cell voltage (1.87 V) Low self-discharge rate
V/Polyhalide	2003	Higher energy density (up to 50 $W\,h\,kg^{-1}$)
V/Mn	2008	Higher cell potential (1.51 V)
V/Fe	2011	Cheaper catholyte Potential for low-cost separator use
V/H_2	2013	Fast hydrogen kinetics Crossover can be collected and pumped back

solid flow cell was presented by Chiang *et al.* which utilises electrolytes containing lithium ion suspensions, offering energy density capacities up to 10 times higher than typical RFBs.[23]

2.1.1 Hydrogen based RFBs

Expertise gained on PEMFCs led to the arrival of RFBs combining a liquid catholyte with a hydrogen anode. This configuration allows the typical parasitic hydrogen evolution reaction to become the main anodic process. Although a platinum based catalyst is necessary for the hydrogen oxidation reaction to take place, PEMFC research has demonstrated that the platinum loading can be now reduced below 0.4 $mg\,cm^{-2}$, thus making the electrodes more affordable.[24–26] In Table 2.2, the current existing hydrogen based RFBs are listed: H_2/Br_2, H2/Fe and H_2/Cl.

Table 2.2: Current hydrogen based RFBs and challenges faced.[27–32]

	Hydrogen/Bromine	Hydrogen/Iron	Hydrogen/Chlorine
Cell Potential	1.098 V	0.77 V	1.36 V
Challenges	Toxicity and safety issue if bromine leaks Membrane corrosion Risk of catalyst contamination on H_2 side	Iron sulphate: High viscosity Poor charge polarisation Iron chloride: High acid vapour pressure Risk of toxic chlorine vapour formation	Platinum and ruthenium are both unstable in the system environment Highly corrosive environment with chlorine reactant and HCl product Water management difficulties

The H_2/Br_2 RFB shows promising results with lifetime performance up to 10,000 cycles and a maximum power density of 1400 mW cm^{-2}.[27,28] However it raises safety concerns due to the toxicity of bromine fumes as well as a highly corrosive environment which would have dramatic effects on the membrane and the H_2 side catalyst.[27,28] Regarding the H_2/Fe RFB, two different systems have been reported: 1 M $FeSO_4$, and 0.9 M $FeCl_3$ with 0.9 M HCl, achieving a maximum peak power density of 257 mW cm^{-2} and 270 mW cm^{-2} respectively.[29,30] The literature presents divergent opinions on which electrolyte composition is best suited as the the $FeSO_4$ electrolyte system offers good cyclability but with high viscosity and charge overpotential.[29] Whereas the $FeCl_3$ electrolyte system suffers from operating in a highly corrosive environment which complicates material compatibility.[33] The H_2/Cl_2 RFB has delivered a maximum power density of 500 mW cm^{-2} and low polarisation losses.[26,31,32] The scope of this project is to explore two separate hydrogen based RFBs. The first, reported by Yufit *et al.* in 2013, shares the same cathode as the VRB utilising a V(IV)/V(V) redox couple[19] and is referred to as a Regenerative Hydrogen Vanadium Fuel Cell (RHVFC). The second RFB, a Regenerative Hydrogen Cerium Regenerative Fuel Cell, uses a Ce(III)/Ce(IV) catholyte and was developed in this research.[34] Both of these RFBs will be discussed in more detail further in this work.

2.2 Flow battery components

In this Section the different components used in RFBs will be discussed, for the purpose of this investigation the attention will mainly be oriented toward loss mechanisms associated with those components.

2.2.1 Membrane

The ion selective membrane is an essential component of an RFB, it mainly serves to prevent the anolyte and catholyte from mixing during operation while letting selective ions pass through it, while electrons will be forced to pass through an external circuit.[35] The criteria for a suitable membrane are namely: good stability in an acidic environment, resistance to oxidation, low electronic conductivity, high proton conductivity, low permeability to other ions, good mechanical properties and low cost.[35] Most membranes are made up of cross-linked linear polymer chains that form a three-dimensional network that stops the membrane from dissolving in water.[35]
The most commonly used membrane in many RFB systems is Dupont's Nafion which is formed of perfluorosulfonic acid polymers.[36] The hydrophobic Teflon backbone of the Nafion structure provides excellent mechanical and chemical stability while the perfluorovinyl ether groups terminated with sulfonate groups attached to the backbone ensures ionic conductivity.[36]
However, in the case of VRBs, Nafion has poor selectivity to vanadium ions which leads to diffusion of vanadium across the membrane during charge/discharge cycles; this leads to a temporary loss of capacity.[35,36] For a VRB, the two electrolytes can be mixed at regular interval in order to retrieve the flow cell's initial capacity.[35] Nonetheless crossover reduces coulombic efficiency hence it is important to understand the nature and the mechanism of vanadium ions transport across the membrane.[12,35] Using ultraviolet-visible (UV-vis) spectroscopy Vijayakumar *et al.* showed that only V(IV) ions were absorbed inside the membrane in its hydrated form $[VO(H_2O)_5]^{2+}$, which means that the V(IV) ions are not directly bound to the membrane structure but bound through the hydration shell.[37] Through x-ray photoelectron spectroscopy (XPS) studies they identified the presence of V(V) ions on the surface of the Nafion which could easily be removed by sonication in deionised water, unlike the removal of V(IV) ions

which required boiling of the membrane in water.[37] Nuclear magnetic resonance (NMR) data collected after V(IV) ion removal revealed no structural change of the Nafion.[37] Although the absorption of V(IV) cations implicates the reduction of the hydration level of the membrane.[37] The use of thin Nafion membranes (<100 µm) offers the benefit of low ionic resistance, however crossover is enhanced, hence thicker membranes (>100 µm) are generally used.[36] Additionally, water transfer between the two half-cells in VRBs is a concern as it can lead to the dilution and precipitation of vanadium salts in the electrolytes.

Nafion has a good chemical stability to the oxidising environment of the vanadium catholyte, however Sukkar *et al.* reported that Nafion 112 (51 µm) has a poor stability when immersed in a 0.1 M V(V) ions solution over extended period of time, though it displayed improved stability when soaked in a 1 M V(V) solution, indicating the important role of the V(V) concentration in the membrane degradation.[38] Moreover the study also revealed that the membrane did not display observable signs of degradation during operation in a VRB which can be explained for two reasons: the higher concentration of V(V) during operation compared to the immersion experiments and the absence of continuous exposure of the membrane to V(V) cations during cycling.[38]

There is no specific studies found on the effect of Ce (III) and Ce (IV) on Nafion membranes available.

2.2.2 Electrodes

Carbon based materials such as carbon felt, carbon cloth, carbon-polymer composite and many others are commonly used as electrodes in RFBs. The general requirements for the electrode material are good chemical stability in the electrolyte, adequate porosity, high surface area, low electrical resistivity, wide operating potential range and good mechanical properties when it undergoes compression.[7,39,40] Carbon felt and graphite have been thoroughly investigated in VRB systems where they act as a liquid diffusion layer (LDL), as opposed to a gas diffusion layer (GDL) in a PEMFC.[7] The criteria for choosing an appropriate electrode material for the anode side of the RHVFC are the same with the exception that the carbon felt must not be impregnated with polytetrafluoroethylene (PTFE) as demonstrated by Yufit *et al.*[19] The

authors showed that PTFE increased the hydrophobicity of the electrode which in the case of the RHVFC leads to mass transport limitations, hence it is important that the carbon felt remains untreated.[19]

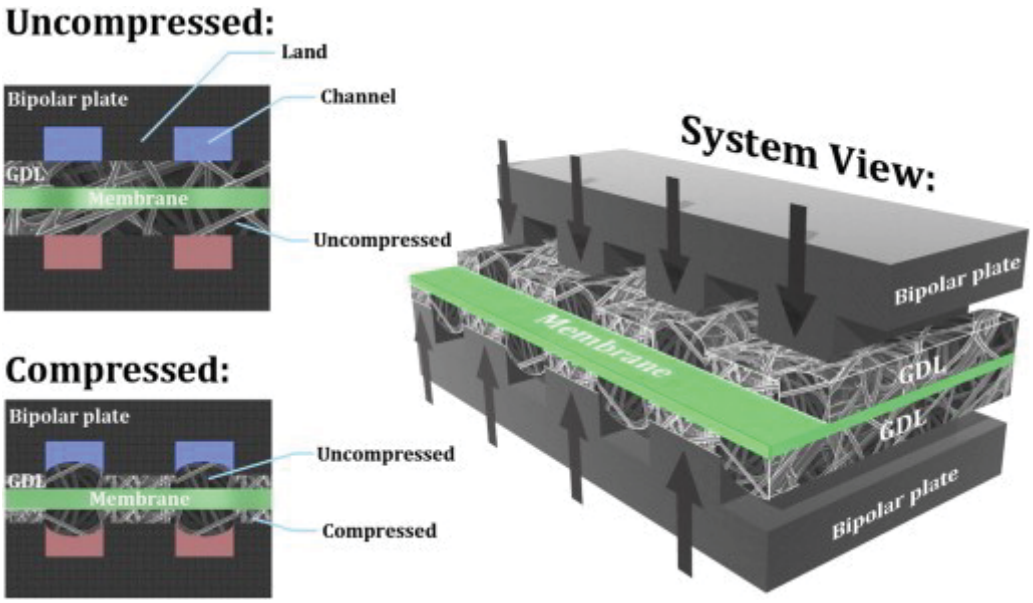

Figure 2.3: Illustration of the effect of compression on the GDL of PEMFC, showing compression under lands and tenting in the open channels. Reproduced from[41] with permission from Elsevier.

The carbon felt material undergoes mechanical compression during cell assembly which allows better contact with the current collectors. However an excessively low or large compression force applied can lead to a decrease of the system efficiency.[14,40] Additionally if the electrode is overly compressed it can suffer from irreversible deformation that alters the pore size and therefore the diffusion of the liquid or gaseous electrolyte.[40,41] Millichamp *et al.* demonstrated that typical GDL used in PEMFC, having soft and brittle structures, would suffer from crushing under the rib of flow channel plates and would display a tenting behaviour under the channel as depicted in Fig. 2.3.[41] Another problem that can occur is oxidation of the carbon material when overcharging the battery which leads to degradation of the electrode; it has been identified that oxidation of graphitic carbon based electrodes leads to the formation of carbon/oxygen functional groups whereas the oxidation of the more reactive carbon black implies formation of carbon dioxide.[7]

In both cells studied in the present work, the RHVFC and the RHCFC, the hydrogen anode requires the use of platinum which is a very stable metal in oxidising environments. However

it has been observed that it can dissolve and migrate in PEMFCs.[42] Chemical degradation of the membrane where the Pt has been redeposited and accumulating has also been observed, although this seems to mainly affect the oxygen side of the PEMFC.[42]

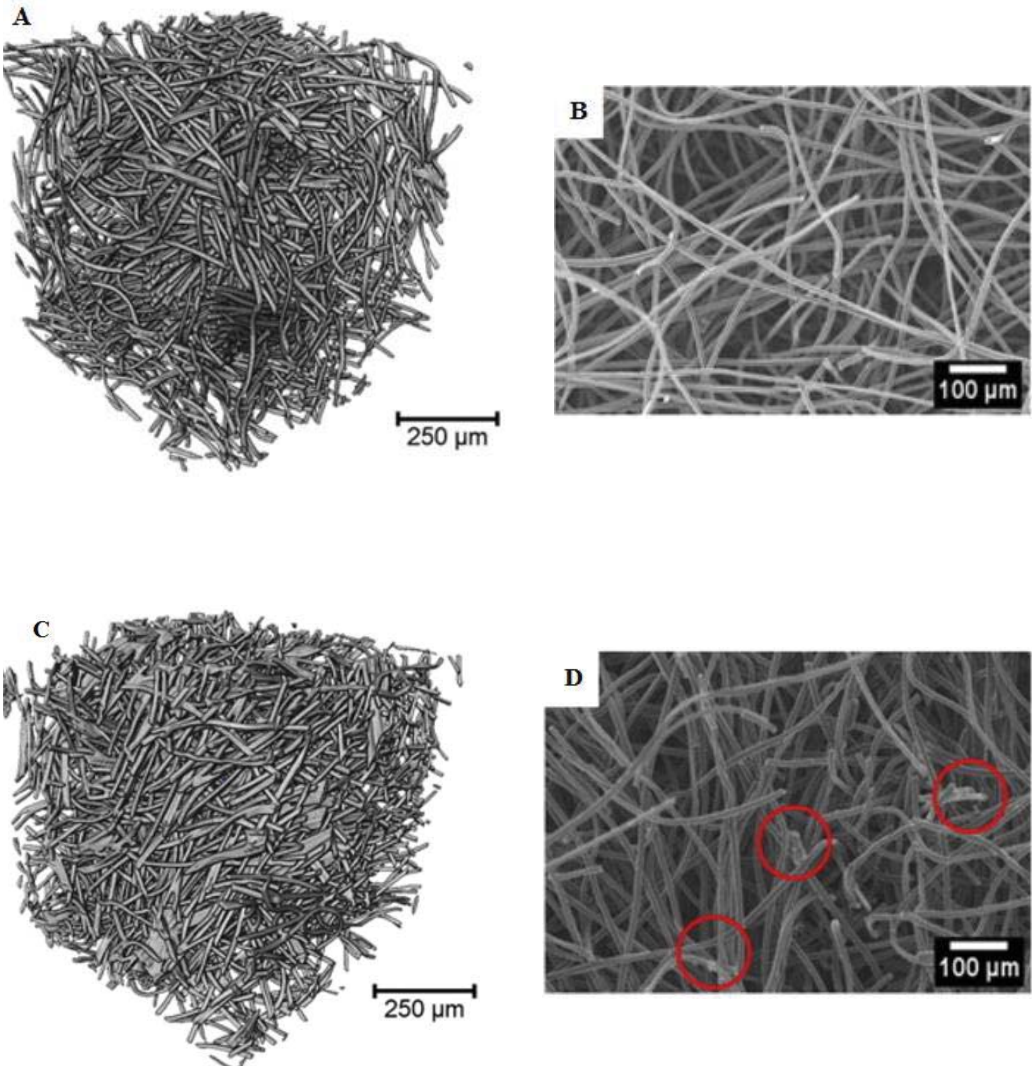

Figure 2.4: A) 3D reconstructed image of fresh graphite felt electrode B) SEM image of the fresh graphite felt electrode C) 3D reconstructed image of the cycled graphite felt electrode D) SEM image of the cycled felt electrode where the circled regions indicate the presence of fibre bundles.[43]

Despite the intensive on-going research in RFBs, degradation of RFB electrode materials has not been widely investigated. This is partly due to the wide range of different chemistries developed which means the electrode degradation will vary from one system to another.[40] However, Trogadas *et al.* have published a study using 3D x-ray tomography as a diagnostic tool to monitor structural changes in carbon felts used in a VRB.[43] As presented in Fig. 2.4A and B,

the fresh felt which was in contact with the VRB catholyte but had not been electrochemically cycled shows the presence of individual fibres ($\sim$ 13 µm diameter each); whereas the felt that underwent 33 charge/discharge cycles as depicted in Fig. 2.4 C and D shows the formation of agglomerated fibre clusters.[43] These fibre bundles are a sign of carbon oxidation in the used felts which is also verified using XPS which reveals the presence of intermediate carbon oxidation products (COOH) on the electrode surface.[43]

Due to the high standard electrode potential of the Ce(III)/Ce(IV) electrolyte (between 1.28 and 1.72 V[44,45]) materials have to be selected carefully. Leung *et al.* have studied the use of different electrode materials on the cerium electrode in a Zinc-Cerium RFB.[46] The results show that whenever carbon based materials are used, they would degrade (due to corrosion) leaving carbon particles in the cerium electrolyte whereas platinised titanium based electrodes would display no observable changes.[46] However, the majority of electrodes reported in the literature for the cerium electrode contain platinum, which is also a good catalyst for the parasitic oxygen evolution reaction.[47] In recent times, with the surge of 3D printing techniques, it has been suggested that they could be utilised to produce materials in order to improve the mass transport of species and, perhaps, reduce costs.[48] Currently high surface laser sintered titanium scaffolds are available, these could be catalysed so that they could be used in cerium based RFBs.[48,49] Furthermore, using 3D printing, even more complex structures could be designed to meet the needs of different RFBs.

2.2.3 Flow channel design

The flow channel plates deliver the pumped electrolyte uniformly to the whole active surface area of the electrode to minimise mass transport losses in the cell; they are often also used as current collectors.[50]

It was demonstrated that a uniform distribution of electrolyte can be achieved in VRBs at high flow rates as this ensures a large mass transport rate of the reactants to the electrode, but this is at the cost of high pumping power.[50,51] Hence a trade-off must be found between mass transport rate and pressure drop through flow channel design.[50] There are a number of different generic designs such as parallel, interdigitated and serpentine, but for the purpose of this thesis

only the serpentine design and its characteristics will be discussed.

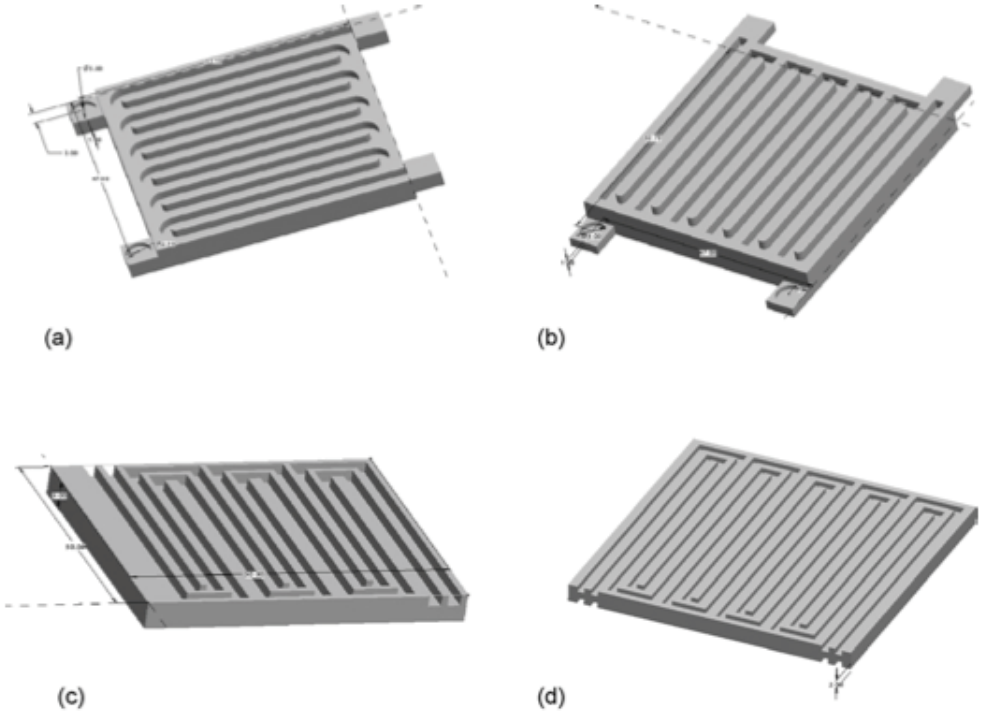

Figure 2.5: Illustration of multiple serpentine flow channel design with (a) single channel curvilinear bends, (b) single channel square bends, (c) dual serpentine channels with width 2 mm, (d) dual serpentine channels with width 1.2 mm. Reproduced from[51] with permission from Elsevier.

Boddu *et al.* have investigated the effect of the shape and size of different serpentine channel configurations for PEMFCs systems.[51] Some of those configurations are displayed in Fig. 2.5. The study showed that the curvilinear bends configuration 2.5 a displays lower pressure drops than the square bends (Fig. 2.5 b).[51] Additionally it was also observed that having parallel serpentine channels (Fig. 2.5 c and d) presents many benefits such as an increase of the contact surface area with the active surface area of the electrode and a further reduction of the pressure drop in the channels.[51] Also, it was pointed out that when designing the double serpentine channels it was best to choose a dimension for the channel width that would allow coverage of most of the flow channel plate, such as in Fig. 2.5 d compared to c, as this leads to a larger surface contact area with the electrode.[51] A recent study by Xu *et al.* looking at numerical modelling of flow field designs for VRBs concluded that the lowest overpotential is achieved using serpentine flow fields due to a more uniform electrolyte distribution at the electrode

surface and enhanced electrolyte diffusion in the through-plane direction.[52]

2.2.4 System construction

The general system assembly is critical in order to ensure high performance of the RFB, hence the system has to be designed in order to limit shunt currents in battery stack, external leakages, series resistance and others.[7]

A

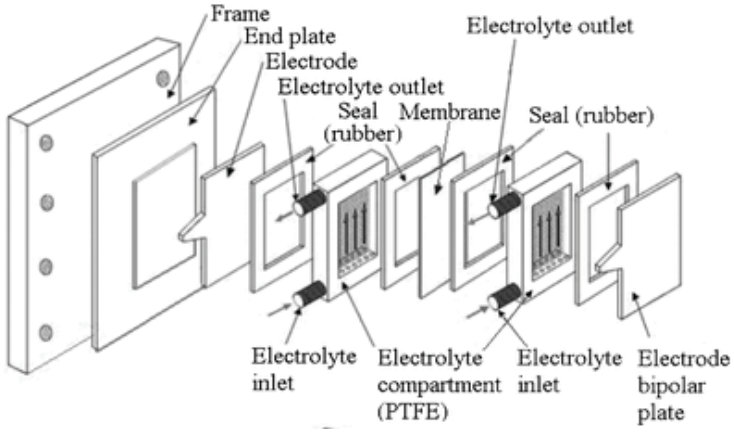

B

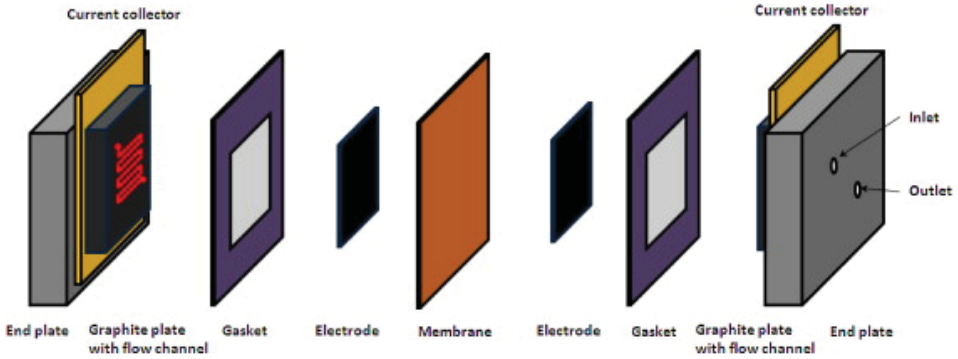

Figure 2.6: RFB assembly A) in a typical system B) in an optimised no gap architecture. Reproduced from[14,53] with permission from the Royal Society of Chemistry and Elsevier.

Fig. 2.6 A depicts a typical RFB assembly set-up, however Aaron *et al.* demonstrated that by using an optimised cell design with a no-gap architecture, as represented in Fig. 2.6B, higher power densities could be achieved in a VRB.[7,14,53] This design allow the membrane, electrodes and current collectors to be in direct contact which effectively remove the electrolyte

compartment needed in the Fig. 2.6A design; additionally they also use thinner carbon felt for the electrodes.[53] Hence this optimised design presents smaller distances for charge transport.[53]

2.3 Critical terms

It is important to define the critical terms used to evaluate and compare RFBs to other electrochemical systems and among themselves.

Firstly energy density is determined by the electrolyte used in the RFB such as the amount of energy stored depends on the solubility of the active species, molecular weight and number of electrons per mole. For example, current lithium-ion and lithium-polymer batteries used in electric vehicles display energy densities of 120-200 $W\,h\,kg^{-1}$ whereas current commercialised RFBs only achieve 30-50 $W\,h\,kg^{-1}$.[54] Another useful parameter that is also dependent on the electrolyte is the capacity expressed in amp-hour. The capacity of a system depends on the solubility of the species and the volume of electrolyte available.

Often for commercialised systems, energy capacity and power output will be given. For example Gildmeister, a German flow battery manufacturer, offers a single unit VRB that has an energy capacity of 400 kWh and a power output of 200 kW, meaning it could give 200 kW for 2 h.[55] By combining these units they can offer up 16 MWh of energy storage capacity with a power output/input of up to 2 MW.[55]

Moreover for lab scale RFB testing, it is common to study the power delivery by discussing the power output for a given operating current density as well as the peak power density. The latter however does not necessarily reflect on the actual operating capabilities of the cell.

2.4 Current state-of-art RFBs

Some of the early RFB deployments were in the 1990s in Japan with a 1 MW/ 4 MWh zinc-bromine battery installed for load levelling applications.[14] This was followed by several more VRB installations in the 1990s and early 2000s by Sumitomo Electric Industries (SEI) for both load levelling purposes and coupled with wind turbines technology.[14,54] SEI also installed a 1.5

MW/1.5 MWh back-up power system at the Tottori Sanyo Electric manufacturing plant in 2001.[54]

In the early 2000s, RWE Innogy had under construction two large scale pilot plants (14 MW/120 MWh each) of their Regenesys® bromine-polysulphide flow batteries, one in Cambridgeshire (UK) and one in Mississippi (USA).[14] The plant in Cambridgeshire, next to a power station, was meant to be one of the first fully integrated demonstration plant for this technology upon completion.[56] Although partially built, neither of the demonstration plants were fully commissioned.[56]

The first zinc-cerium RFB was developed by Plurion Inc. in the United Kingdom which consisted of a 2 kW-1 MW testing facility.[14,57] However the company went into liquidation in 2010, and although academic research has continued to pursue zinc-cerium technology, no further commercialisation attempts have been made.

Table 2.3 summarises some of the active RFB manufacturers around the world.

Table 2.3: Some the currently active RFB manufacturers in the world who attended the International Flow Battery meeting in 2014 and 2015.

Company	**Chemistry**	**Location**
EnerVault Corporation	Iron/Chromium	USA
SCHMID Energy systems	VRB	Germany
UniEnergy Technologies	VRB	USA
Imergy Power Systems	VRB	USA/India
Elestor BV	Hydrogen/Bromine	Netherlands
Sumitomo Electric Industries	VRB	Japan
EnStorage	Hydrogen/Bromine	Israel
Redflow	Zinc/Bromine	Australia
REDT UK	VRB	UK

2.5 RFB fundamentals

The general form of a redox reaction is given by Equ. 2.1, where O is the oxidant, n an integer, e^- an electron and R the reductant. The thermodynamic potential of the cell when no current is flowing, also referred to as the open circuit voltage (OCV), is described by the Nernst equation (Equ. 2.2). Here E^0 is the standard cell potential, R the universal gas constant, T the temperature, F the Faraday constant, C_O the oxidant concentration and C_R the reductant concentration.

$$O + ne^- \rightleftharpoons R \tag{2.1}$$

$$E_{equ} = E^0 + \frac{RT}{nF} ln \left(\frac{C_O}{C_R} \right) \tag{2.2}$$

However a deviation from E_{equ} is observed for the measured potential E when a current is applied, this is referred to as an overpotential and can be obtained using Equ. 2.3.

$$\eta = E - E_{equ} \tag{2.3}$$

This overpotential is the sum of all contributions from various reaction steps as depicted in Fig. 2.7. The following will discuss the nature of those contributions.

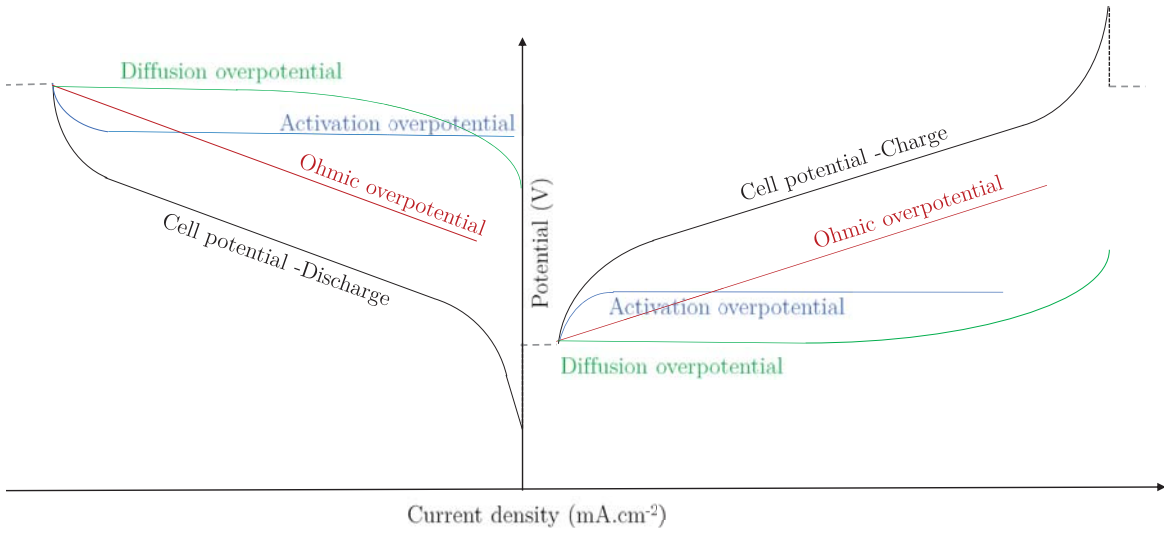

Figure 2.7: Typical I-V curve with the breakdown of the different losses contributions.[58]

2.5.1 Activation losses

The activation overpotential represents the energy required to overcome the activation barrier for the electron transfer reaction to take place at the electrode interface. It is described by the Butler-Volmer equation presented in Equ. 2.4 where j is the current density, j_0 the exchange current density, T the absolute temperature, η the charge transfer overpotential, n the number of electrons involved in the process, and α_c and α_a the cathodic and anodic transfer coefficients respectively.

$$j = j_0 \left[exp\left(\frac{-\alpha_c nF\eta}{RT}\right) - exp\left(\frac{\alpha_a nF\eta}{RT}\right)\right] \tag{2.4}$$

This form of the Butler-Volmer equation is true when the rate of the reaction is dominated by the charge transfer step, and it also assumes that there is a negligible concentration difference (<10 %) between the bulk solution and the reaction site.[59]

2.5.2 Ohmic losses

The voltage drop measured, related to various ohmic resistance sources in the cell (i.e. membrane, electrodes, bulk electrolyte, etc.), is referred to as the IR drop as described by Equ. 2.5 where I is the current and R the resistance. This ohmic polarisation can have severe effects at high current but it can be minimised by better cell design, and by appropriate materials selection.

$$\eta = IR \tag{2.5}$$

2.5.3 Mass transport losses

Mass transport losses refers to the diffusion overpotential that an electrochemical system would suffer when a concentration difference arises between the bulk electrolyte and the electrode surface. It is best described by Equ. 2.6 where j_l is the limiting current density.[59]

$$\eta = \frac{RT}{nF} ln\left(\frac{j_l - j}{j_l}\right) \tag{2.6}$$

2.5.4 Other losses

In addition to electrochemical losses, crossover of species from one electrode to another through the ion exchange membrane, or via physical leaks within the cell, can occur. Although not always leading to a permanent capacity loss, like in the VRB, it still requires extra measures to be taken in order to retrieve the full capacity *e.g.* : re-mixing of catholyte and anolyte, etc. which increases overall system cost and complexity. Similarly RFBs can face additional losses such as pumping losses.

2.5.5 Performance assessment

As mentioned previously, flow batteries offer independent power density and energy storage capacity. The power density is defined as the amount of energy transferred per unit area at a given time and is measured in units of watts per centimetres square $\mathrm{W\,cm^{-2}}$. Its expression is given by Equ. 2.7 where P(t), V(t) and I(t) are the power, voltage and current at a given time and A the active surface area.

$$P(t) = \frac{V(t)I(t)}{A} \tag{2.7}$$

The capacity of the system refers to the amount of energy available which is dependent on the volume and concentration of the active species, it is measured in amp hours (Ah). It can be calculated using Equ. 2.8 where Q is the capacity, I(t) the current at a given time and t_{max} the end time of the charge/discharge step.

$$Q = \int_0^{t_{max}} I(t)dt \tag{2.8}$$

However for a given electrolyte, the theoretical maximum capacity can be calculated using Equ. 2.9 where N is the number of moles of the active species, n the number of electrons per mole, and F the Faraday constant.

$$Q = \frac{1}{3600} \times NnF \tag{2.9}$$

The efficiency of a RFB can be split into its coulombic, voltage and energy efficiencies as given by Equ. 2.10 - 2.12.

$$Coulombic\ efficiency = \frac{\int_0^{t_{max}} I_{discharge} dt}{\int_0^{t_{max}} I_{charge} dt} \tag{2.10}$$

$$Voltage\ efficiency = \frac{\langle V_{discharge} \rangle}{\langle V_{charge} \rangle} \tag{2.11}$$

$$Energy\ efficiency = Coulombic\ efficiency \times Voltage\ efficiency \tag{2.12}$$

2.6 Electrochemical characterisation techniques

Various voltammetry and amperometry techniques are used in this work in order to test and characterise the electrochemical systems. Two key methods are introduced in this section, cyclic voltammetry (CV) and electrochemical imdepance spectroscopy (EIS).

2.6.1 Voltammetry and Amperometry techniques

A cyclic voltammogram plot as presented in Fig. 2.8 can be obtained by applying a linearly increasing then decreasing potential to the cell and measuring its current response.[59] The potential can be swept at different rates (mV/s) between a lower and an upper cut-off limit. The resulting plot can provide useful information such as the anodic and cathodic current peaks ($I_{p,a}$ and $I_{p,c}$) found at their corresponding anodic and cathodic potentials referred to in Fig. 2.8 as $E_{p,a}$ and $E_{p,c}$ respectively.[59] These peaks corresponds to the oxidation and reduction processes occurring in the cell and their separation is an indicator of reversibility.

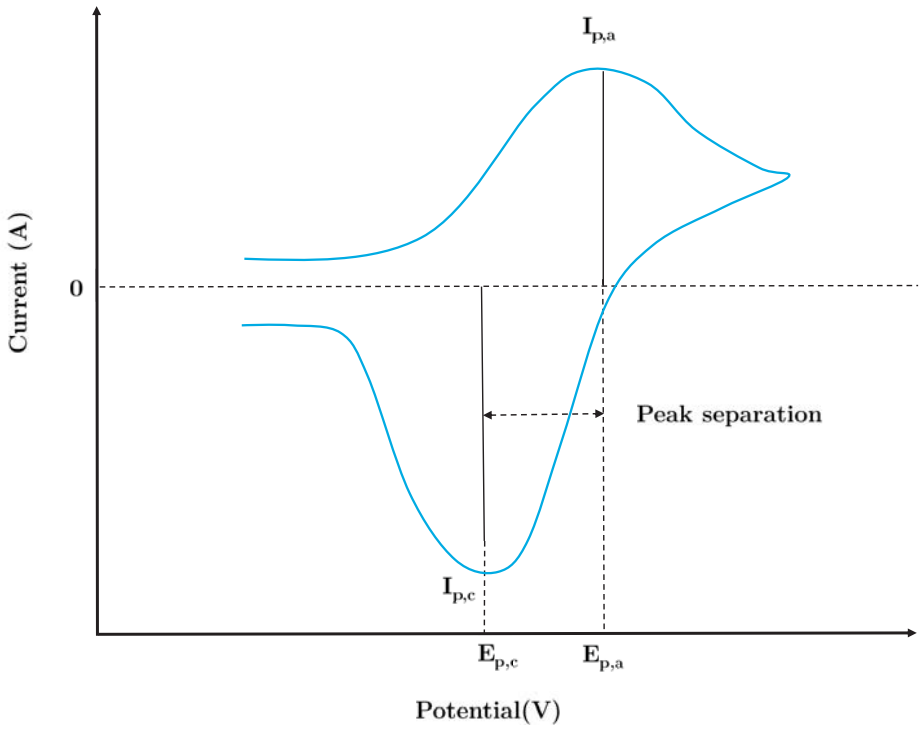

Figure 2.8: A typical cyclic voltammogram plot with the anodic and cathodic peak currents $I_{p,a}$ and $I_{p,c}$ found at their corresponding anodic and cathodic potentials $E_{p,a}$ and $E_{p,c}$.

CV measurements are dependent on several factors such the concentration of species, electrode material, presence of additional reactions, etc. They provide useful information about the operating potential window of the cell as well as the suitability of an electrode material.

2.6.2 Electrochemical Impedance Spectroscopy[60,61]

Electrical resistance is a well-known concept which measures the ability of a circuit element to resist a current flow. While electrical resistance is defined by Ohms law where it is equal to the ratio of the voltage against the current, this only applies to an ideal resistor. Electrochemical impedance spectroscopy (EIS) allow us to assess the resistance of any circuit element to a current flow, it can be described as a complex resistance.

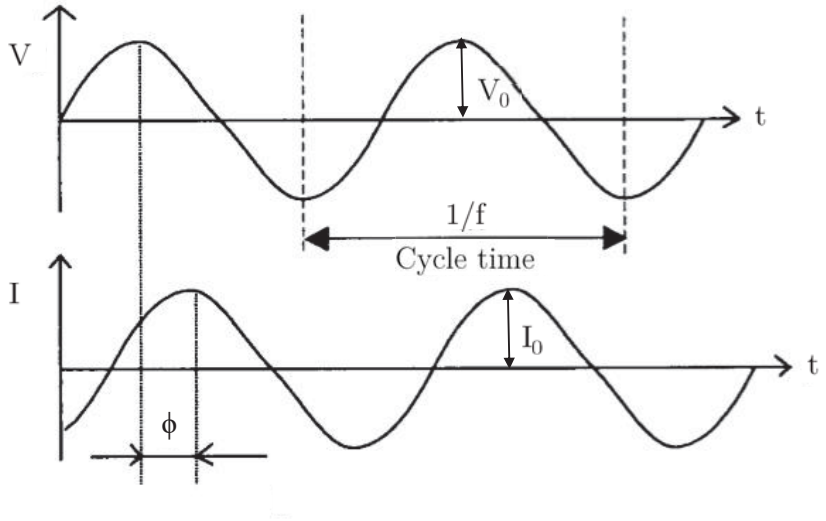

Figure 2.9: Sinusoidal voltage input on a circuit at a frequency f and its current response.[60]

EIS is measured by applying an AC voltage/current signal to the system and measuring its current/voltage response. As depicted in Fig. 2.9, an AC voltage with a small amplitude V_0 is applied at a frequency f and the current response of the system at the same frequency presents an amplitude I_0 and a phase shift ϕ with respect to the voltage signal. Both the voltage and current signal are given by Equ 2.13 and 2.14 where the radial frequency is defined as $\omega = 2\pi f$.

$$V(t) = V_0 sin(2\pi ft) = V_0 sin(\omega t) \tag{2.13}$$

$$I(t) = I_0 sin(2\pi ft + \phi) = I_0 sin(\omega t + \phi) \tag{2.14}$$

Similarly to the resistance defined by Ohms law, the expression for complex impedance is given by Equ. 2.15 where it represents the ratio of voltage and current.

$$Z = \frac{V(t)}{I(t)} = \frac{V_0 sin(\omega t)}{I_0 sin(\omega t + \phi)} \tag{2.15}$$

As a complex function, impedance can be expressed as a combination of its real part Z_R and imaginary part Z_{IM} as given by Equ. 2.16, where its magnitude | Z | and phase angle θ are given by Equ. 2.17 and 2.18.

$$Z = Z_R + iZ_{IM} \tag{2.16}$$

$$|Z| = \sqrt{Z_R^2 + Z_{IM}^2} \tag{2.17}$$

$$\theta = arctan\left(\frac{Z_{IM}}{Z_R}\right) \tag{2.18}$$

This complex number can be represented as a Nyquist plot as shown in Fig. 2.10, where the data is presented as a locus of points and where each point was measured at a different frequency. The convention is to present Z_R as the x-axis and negative Z_{IM} as the y-axis. As demonstrated on the graph, low frequency data points lie on the right hand side while the high frequency ones lie on the left hand side. Often Nyquist plots will be used to help identify the various processes taking place in the system. For example a perfect semi-circle will indicate the presence of a single step process whereas a depressed semi-circle or a multi-loop will indicate the presence of a more complex phenomenon.

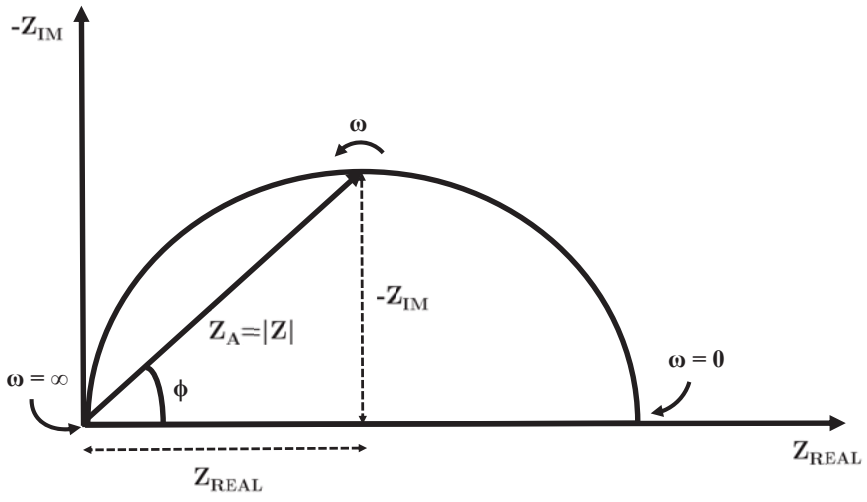

Figure 2.10: Nyquist representation of impedance data.

However with this form of representation, frequency information is hidden. Commonly a few points with characteristic frequencies would be labelled on the Nyquist plot. Moreover, large discrepancies in frequencies would tend to be overlooked between the experimental and simulated data (using an equivalent circuit model), which mostly occur at low impedance values.

Another possible representation of impedance data are Bode plots. As depicted in Figure 2.11, the logarithm of the impedance magnitude and the phase shift are plotted against the logarithm of frequency. Bode representation, unlike the Nyquist one, expose the dependency of impedance on frequency and provides a better insight at lower impedance values (at low and high frequency values).

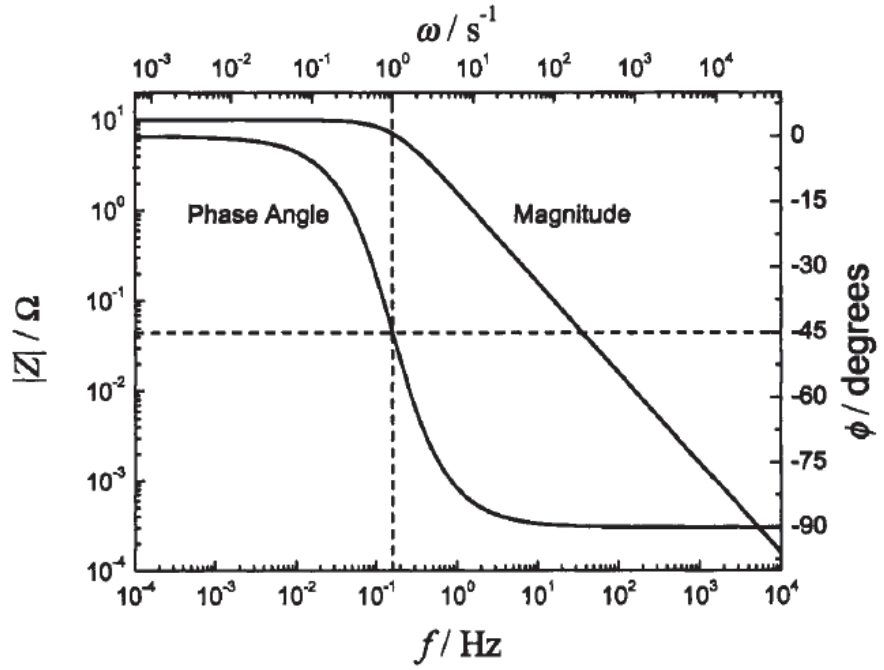

Figure 2.11: Bode representation of the impedance response for a 10 Ω resistor in parallel with a 0.1 F capacitor.[61]

The phase angle plot is the most useful when comparing the experimental data with its equivalent circuit models as the phase angle depends on the capacitive and resistive components of the circuits. Nonetheless for cases where processes are coupled it becomes difficult to determine critical frequencies purely relying on phase angle change. The impedance magnitude plot is far less sensitive to circuit parameters, however the asymptotic values at low and high frequencies provide the direct current (DC) and ohmic resistance respectively. By plotting the real and imaginary part of the impedance as a function of the frequency logarithm, as displayed in Fig. 2.12, some additional information can be extracted. The real part behaves in an analogous way to the impedance magnitude where the same DC and ohmic resistance values can be extracted, while the imaginary part is independent of the ohmic resistance value. Using the Z_{IM} vs log(f) plot, the characteristic frequency value at a Z_{IM} peak can be obtained; the presence of several

Z_{IM} maxima indicates the presence of multiple processes.

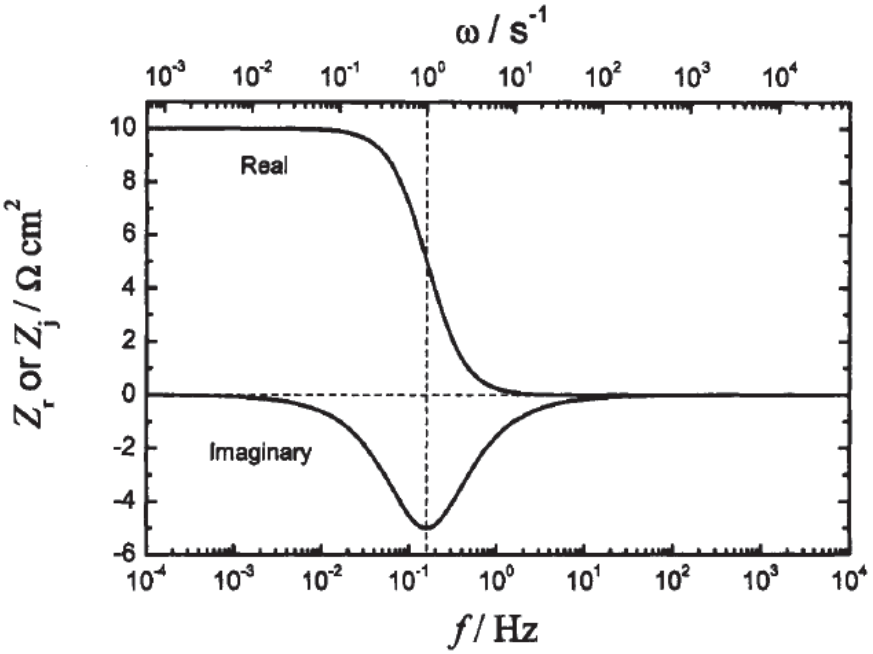

Figure 2.12: Bode representation of the impedance response for a 10 Ω resistor in parallel with a 0.1 F capacitor.[61]

Equivalent circuit fitting

Equivalents circuits can be used to match experimental EIS data in order to extract useful parameters and identify the underlying processes. Circuit elements are usually divided into two categories: ideal and non-ideal.

The ideal circuit elements include resistors, capacitors and inductors. Starting with the resistor, its impedance has no imaginary part and is independent of frequency. Hence in a Nyquist plot, a resistor would be represented by a single point on the real part axis. Its impedance is given by Equ. 2.19 where R is the resistance.

$$Z_R = R \tag{2.19}$$

A capacitor's impedance response is described by Equ. 2.20, where it only has an imaginary component. The current output through a capacitor has a -90° phase shift with respect to the voltage input. Moreover looking at its impedance expression, it is clear that at high frequencies the contribution from a capacitor is small and as the frequency increases so will the impedance.

$$Z_C = \frac{1}{j\omega C} \tag{2.20}$$

An inductors impedance response is described by Equ. 2.21 where, similar to the capacitor, it only has an imaginary component. However this time the current output has a 90° phase shift with respect to the voltage input. The inductor has the opposite impedance behaviour to the capacitor where at high frequency its contribution is at its maximum and will decrease with decreasing frequency.

$$Z_L = j\omega L \tag{2.21}$$

Real electrochemical systems, where complex processes are taking place, rarely behave like ideal circuit elements. Therefore it is often useful to model the impedance behaviour using non-ideal elements such the constant phase element (CPE) which can be considered as a leaky capacitor. Its name implies that the phase angle of the process described is independent of the frequency. The CPE's impedance is given by Equ. 2.22 where the exponent α can vary between -1 and 1 and Q the CPE coefficient has units of $\Omega^{-1}s^{\alpha}$ unless if it is a pure capacitor in which case Q=C [F] and $\alpha = 1$. Other special cases present when:

- α = -1, the CPE behaves as an inductor.
- $\alpha = 0$, the CPE behaves as a resistor
- $\alpha = 0.5$, the CPE behaves as a semi-infinite Warburg element which is explained further below.

$$Z_{CPE} = \frac{1}{Q(j\omega)^{\alpha}} \tag{2.22}$$

Any other intermediate value for α could be explained by the presence of inhomogeneities in the material tested. However non characteristic values makes the interpretation of the physical processes happening in the system more challenging.

Another non-ideal circuit element is the semi-infinite Warburg element which describes diffusion through an infinitely thick diffusion layer, as described by Equ. 2.23 where σ is the Warburg

coefficient. This impedance expression is derived from the solution to Ficks second law for one-dimensional diffusion of a particle in a semi-infinite space.

$$Z_{Win} = \frac{\sigma}{\sqrt{\omega}} - j\frac{\sigma}{\sqrt{\omega}} \tag{2.23}$$

However, as often the diffusion layer cannot be approximated as infinite, two other finite Warburg diffusion cases exist with added boundary conditions. The first one is referred to as the Warburg short element where it is assumed that the diffusive species are consumed instantly (meaning that the flux of species is constant at the boundary). There is also a Warburg open element where it is assumed that the diffusion materiel (i.e. electrode) is blocking the diffusion.

These elements can be combined into circuits, modelling the processes taking place in the system. For elements in series, as represented in Fig. 2.13 A, the impedance sum for all elements is given by Equ. 2.24, and for elements in parallel (Fig. 2.13 B), the impedance is given by Equ. 2.25.

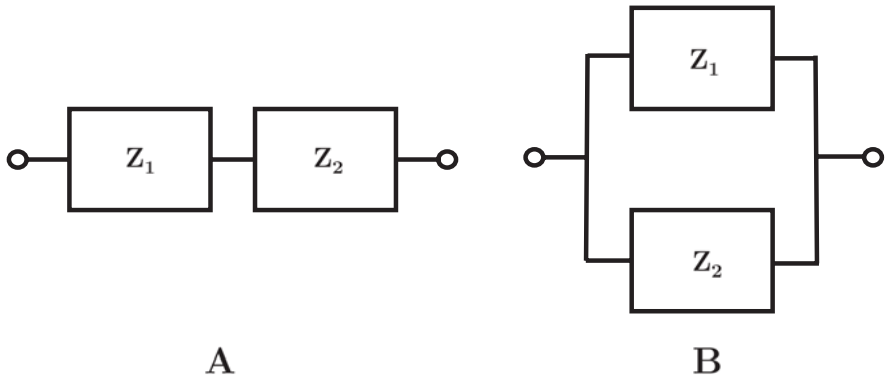

Figure 2.13: Combination of circuit elements A) in series B) in parallel.

$$Z = Z_1 + Z_2 \tag{2.24}$$

$$Z = \left[\frac{1}{Z_1} + \frac{1}{Z_2}\right]^{-1} \tag{2.25}$$

Ambiguity of EIS

Impedance data analysis using equivalent circuit analogues present an inherent ambiguity. It is often possible to get a similar EIS response using different circuit analogues. So to answer the question as to which circuit analogues should be chosen, the following two principles should be applied:

- Knowledge of the physical processes taking place in the system should guide selection of the most appropriate combination of elements. Lower fitting errors may be found using an alternative circuit which has less physical meaning, but this should be avoided as the interpretation and usefulness of such circuits is questionable.
- Simplicity should prevail when choosing circuit models. For similar fitting errors, the simplest circuit should be used.

2.7 Conclusions

This Chapter presented an overview of RFB principles and different chemistries available with a focus on hydrogen based ones given that both RFBs studied in this work have a hydrogen anode. General components (i.e. membrane, electrodes, flow channel design, system construction) properties and challenges were presented in order to understand the current literature. Additionally the specific terms used to characterise and compare RFBs among themselves or with other electrochemical devices were explained. Next an overview of different commercial RFBs was given with examples of current RFB manufacturers in the world. Finally, fundamental electrochemistry concepts and electrochemical techniques needed to investigate and understand RFBs were presented.
Overall, this Chapter has reported the current state of research of RFBs and has defined the concepts necessary to understand the work presented in the following Chapters.

References

[1] L. H. Thaller, *NASA TM X-71540*, 1974.

[2] L. H. Thaller, 1979, **NASA TM-79**, year.

[3] Energy Development Associates, *Development of the Zinc Chloride Battery for Utility Applications*, Electric power research institute technical report.

[4] P. Leung, X. Li, C. Ponce de León, L. Berlouis, C. T. J. Low and F. C. Walsh, *RSC Advances*, 2012, **2**, 10125.

[5] K. Divya and J. Østergaard, *Electric Power Systems Research*, 2009, **79**, 511–520.

[6] M. Rychcik and M. Skyllas-Kazacos, *Journal of Power Sources*, 1988, **22**, 59–67.

[7] A. Parasuraman, T. M. Lim, C. Menictas and M. Skyllas-Kazacos, *Electrochimica Acta*, 2013, **101**, 27–40.

[8] D. Chen, S. Wang, M. Xiao and Y. Meng, *Journal of Power Sources*, 2010, **195**, 2089–2095.

[9] E. Kjeang, R. Michel, D. A. Harrington, N. Djilali and D. Sinton, *Journal of the American Chemical Society*, 2008, **130**, 4000–6.

[10] Q. H. Liu, G. M. Grim, A. B. Papandrew, A. Turhan, T. A. Zawodzinski and M. M. Mench, *Journal of the Electrochemical Society*, 2012, **159**, A1246–A1252.

[11] T. Zawodzinski, International Flow Battery Forum, Ireland, Dublin, 2013.

[12] M. Skyllas-Kazacos, M. H. Chakrabarti, S. a. Hajimolana, F. S. Mjalli and M. Saleem, *Journal of The Electrochemical Society*, 2011, **158**, R55.

[13] A. Z. Weber, M. M. Mench, J. P. Meyers, P. N. Ross, J. T. Gostick and Q. Liu, *Journal of Applied Electrochemistry*, 2011, **41**, 1137–1164.

[14] P. Leung, X. Li, C. Ponce de León, L. Berlouis, C. T. J. Low and F. C. Walsh, *RSC Advances*, 2012, **2**, 10125.

[15] B. Fang, *Electrochimica Acta*, 2002, **47**, 3971–3976.

[16] M. Skyllas-Kazacos, *Journal of Power Sources*, 2003, **124**, 299–302.

[17] F.-Q. Xue, Y.-L. Wang, W.-H. Wang and X.-D. Wang, *Electrochimica Acta*, 2008, **53**, 6636–6642.

[18] W. Wang, S. Kim, B. Chen, Z. Nie, J. Zhang, G.-G. Xia, L. Li and Z. Yang, *Energy & Environmental Science*, 2011, **4**, 4068.

[19] V. Yufit, B. Hale, M. Matian, P. Mazur and N. P. Brandon, *Journal of the Electrochemical Society*, 2013, **160**, A856–A861.

[20] Y. Wang, P. He and H. Zhou, *Advanced Energy Materials*, 2012, **2**, 770–779.

[21] J. Goodenough and Y. Kim, *Journal of Power Sources*, 2011, **196**, 6688–6694.

[22] Y. Wang, Y. Wang and H. Zhou, *ChemSusChem*, 2011, **4**, 1087–90.

[23] M. Duduta, B. Ho, V. C. Wood, P. Limthongkul, V. E. Brunini, W. C. Carter and Y.-M. Chiang, *Advanced Energy Materials*, 2011, **1**, 511–516.

[24] S. Litster and G. McLean, *Journal of Power Sources*, 2004, **130**, 61–76.

[25] J. B. Yadav, J.-W. Park, K.-D. Jung and O.-S. Joo, *International Journal of Hydrogen Energy*, 2010, **35**, 6541–6548.

[26] G. L. Soloveichik, *Chemical reviews*, 2015, **115**, 11533–11558.

[27] K. T. Cho, P. Ridgway, A. Z. Weber, S. Haussener, V. Battaglia and V. Srinivasan, *Journal of the Electrochemical Society*, 2012, **159**, A1806–A1815.

[28] K. T. Cho, M. C. Tucker, M. Ding, P. Ridgway, V. S. Battaglia, V. Srinivasan and A. Z. Weber, *ChemPlusChem*, 2014, **2**, 402–411.

[29] M. Alon, A. Blum and E. Peled, *Journal of Power Sources*, 2013, **240**, 417–420.

[30] M. C. Tucker, K. T. Cho and A. Z. Weber, *Journal of Power Sources*, 2014, **245**, 691–697.

[31] M. Thomassen, B. Børresen, G. Hagen and R. Tunold, *Journal of Applied Electrochemistry*, 2003, **33**, 9–13.

[32] M. Thomassen, E. Sandnes, B. Børresen and R. Tunold, *Journal of Applied Electrochemistry*, 2006, **36**, 813–819.

[33] M. C. Tucker, V. Srinivasan, P. N. Ross and A. Z. Weber, *Journal of Applied Electrochemistry*, 2013, **43**, 637–644.

[34] H. Hewa Dewage, B. Wu, A. Tsoi, V. Yufit, G. Offer and N. Brandon, *J. Mater. Chem. A*, 2015, **3**, 9446–9450.

[35] H. Prifti, A. Parasuraman, S. Winardi, T. M. Lim and M. Skyllas-Kazacos, *Membranes*, 2012, **2**, 275–306.

[36] X. Li, H. Zhang, Z. Mai, H. Zhang and I. Vankelecom, *Energy & Environmental Science*, 2011, **4**, 1147.

[37] M. Vijayakumar, M. Bhuvaneswari, P. Nachimuthu, B. Schwenzer, S. Kim, Z. Yang, J. Liu, G. L. Graff, S. Thevuthasan and J. Hu, *Journal of Membrane Science*, 2011, **366**, 325–334.

[38] T. Sukkar and M. Skyllas-Kazacos, *Journal of Applied Electrochemistry*, 2004, **34**, 137–145.

[39] W. Wang, Q. Luo, B. Li, X. Wei, L. Li and Z. Yang, *Advanced Functional Materials*, 2013, **23**, 970–986.

[40] M. Chakrabarti, N. Brandon, S. Hajimolana, F. Tariq, V. Yufit, M. Hashim, M. Hussain, C. Low and P. Aravind, *Journal of Power Sources*, 2014, **253**, 150–166.

[41] J. Millichamp, T. J. Mason, T. P. Neville, N. Rajalakshmi, R. Jervis, P. R. Shearing and D. J. Brett, *Journal of Power Sources*, 2015, **284**, 305–320.

[42] H. Liu, F. D. Coms, J. Zhang, H. A. Gasteiger and A. B. LaConti, *Polymer Electrolyte Fuel Cell Durability: 'Chemical Degradation: Correlations Between Electrolyzer and Fuel Cell Findings'*, Springer New York, New York, NY, 2009.

[43] P. Trogadas, O. O. Taiwo, B. Tjaden, T. P. Neville, S. Yun, J. Parrondo, V. Ramani, M.-O. Coppens, D. J. Brett and P. R. Shearing, *Electrochemistry Communications*, 2014, **48**, 155–159.

[44] J.-L. Burgot, *Ionic Equilibria in Analytical Chemistry*, Springer, Springer edn., 2012, p. 227.

[45] P. Trinidad, C. P. de León and F. C. Walsh, *Journal of environmental management*, 2008, **88**, 1417–25.

[46] P. Leung, C. Ponce de León, C. Low and F. Walsh, *Electrochimica Acta*, 2011, **56**, 2145–2153.

[47] G. Nikiforidis, L. Berlouis, D. Hall and D. Hodgson, *Electrochimica Acta*, 2014, **115**, 621–629.

[48] L. F. Arenas, F. C. Walsh and C. P. de Leon, *ECS Journal of Solid State Science and Technology*, 2015, **4**, P3080–P3085.

[49] G. E. Ryan, A. S. Pandit and D. P. Apatsidis, *Biomaterials*, 2008, **29**, 3625–35.

[50] T. Jyothi Latha and S. Jayanti, *Journal of Power Sources*, 2014, **248**, 140–146.

[51] R. Boddu, U. K. Marupakula, B. Summers and P. Majumdar, *Journal of Power Sources*, 2009, **189**, 1083–1092.

[52] Q. Xu, T. Zhao and P. Leung, *Applied Energy*, 2013, **105**, 47–56.

[53] D. Aaron, Q. Liu, Z. Tang, G. Grim, A. Papandrew, A. Turhan, T. Zawodzinski and M. Mench, *Journal of Power Sources*, 2012, **206**, 450–453.

[54] P. Alotto, M. Guarnieri and F. Moro, *Renewable and Sustainable Energy Reviews*, 2014, **29**, 325–335.

[55] *CellCube FB 200 storage system from GILDEMEISTER energy solutions*, http://energy.gildemeister.com/en/store/cellcube-fb-200#Technology.

[56] E. Technology, *Review of Electrical Energy Storage Technologies and Systems and of their Potential for the UK*, 2004.

[57] P. Leung, C. Ponce-de León, C. Low, A. Shah and F. Walsh, *Journal of Power Sources*, 2011, **196**, 5174–5185.

[58] S. J. Cooper, *Ph.D. thesis*, Imperial College London, 2015.

[59] F. S. A. J. Bard, G. Inzelt, *Electrochemical Dictionary*, Springer, 2008.

[60] V. F. Lvovich, *Impedance Spectroscopy: Applications to Electrochemical and Dielectric Phenomena*, Wiley, 2012.

[61] M. E. Orazem and B. Tribollet, *Electrochemical Impedance Spectroscopy*, 2008, vol. 48.

Chapter 3

General Experimental Methods

All equipments used in this work is listed in Table 3.1 that can be found at the end of this Chapter.

3.1 System construction

Several iterations to the test cell design were made early on in the project in order to obtain a leak free cell able to accommodate the reference electrode positioning method presented in Chapter 4. Fig. 3.1 displays the construction steps of the final design used for most of the experiments carried out unless specified otherwise in later Chapters. It is here displaying the Generation 2 (Gen2) RHVFC, the cell used for the RHCFC testing only presents minor changes from this which are discussed in Chapter 6.

First a polypropylene (PP) insulating plate was placed on top of an aluminium end plate (Fig. 3.1 a). A rigid aluminium end plate is necessary as PP is a soft material, and hence would otherwise deform. One layer of a full Viton gasket was placed on the PP, (Fig. 3.1 b). Next, a graphite plate with double serpentine flow channels was placed on top of the gasket (Fig 3.1 c) followed by a partial Viton gasket only covering the region outside the active surface area (Fig. 3.1 d). The electrode was then placed on top of the flow channel region (Fig. 3.1 e); for the RHVFC this was either an untreated carbon based electrode or a platinised carbon electrode (with the platinised side facing the membrane) for the cathode and anode side respectively. Finally the Nafion membrane was placed on top of the electrode as depicted in Fig 3.1 f; the

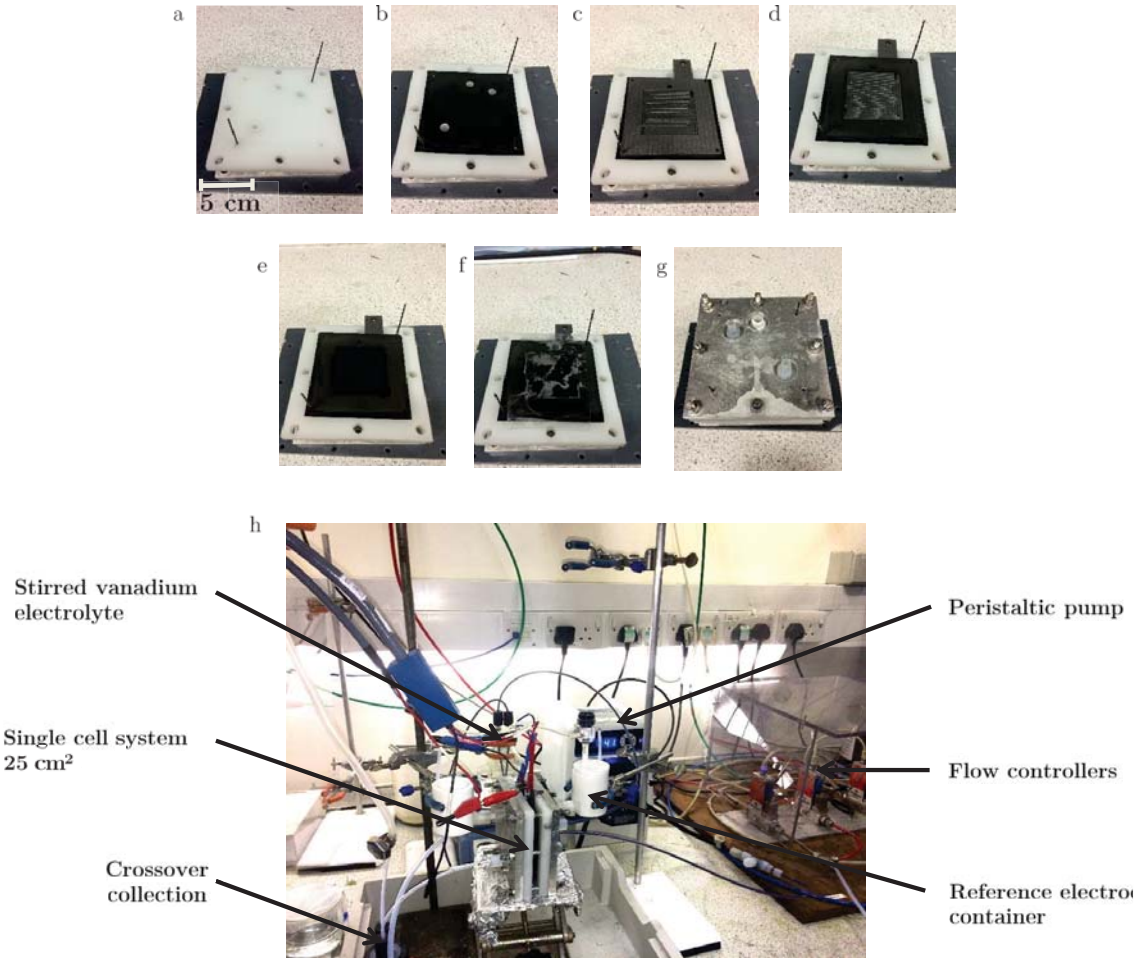

Figure 3.1: RHVFC (25 cm^2) construction steps with a) aluminium end plate and polypropylene plate b) one layer of a full size gasket c) graphite flow channel plate d) partial gasket only covering the region outside the active surface area e) carbon based electrode f) Nafion membrane g) fully layered cell with tie rods h) fully assembled RHVFC with a reference electrode set-up. These assembly steps must be repeated for the second half of the cell

membrane was pre-hydrated in deionised water before use. Once the membrane was in place, all steps from Fig 3.1 a-e were repeated for the other half of the flow cell. Once all the components were layered, as seen in Fig. 3.1 g, the cell was progressively tightened from 4 N.m up to 9 N.m after which the alignment rods were removed. Note that the cell was kept flat on the bench during the tightening process to avoid any displacement of the components. It was only placed upright once the full assembly was completed, as shown in Fig 3.1 h. A reference electrode set-up can be observed on both cathode and anode side in Fig. 3.1 h, its assembly protocol will be discussed in Chapter 4.

When disassembling the cell, the core part comprising the graphite plates, electrodes and membrane, can be stuck together making it impossible to separate the layers. In this case this

core part of the cell was soaked in deionised water for about half an hour in order to allow it to loosen. Once every layer was separated, the PP, Viton and graphite components were left to dry after being washed with soap and rinsed with deionised water. All electrodes were rinsed only with deionised water while bolts, washers and tie rods were periodically cleaned in ethanol. After weeks of usage, the Nafion membrane could appear either blueish if used in the RHVFC (due to V(IV) ions) or yellowish if used in the RHCFC (due to Ce(IV) ions). In order to remove these ions the membrane was soaked in 0.5M sulphuric acid, or methanesulphonic acid, for half an hour if used in the RHVFC or RHCFC respectively. After soaking the Nafion recovered its appearance, and was then kept in deionised water until future use.

3.2 Electrolyte preparation

3.2.1 Vanadium electrolyte preparation

A solution (60 mL) of 1 M vanadium was prepared by adding 14.1 g of vanadium (IV) oxide sulphate hydrate (Sigma-Aldrich) into 60 mL of 5 M sulphuric acid solution (Fluka Analytical). The mixture was left stirring until the solid was completely dissolved. A clear bright blue solution was obtained.

3.2.2 Cerium electrolyte preparation

A solution (50 mL) of 0.5M cerium was prepared by adding 5.75 g of Ce (III) carbonate (Sigma-Aldrich) to 38 mL of deionised water and then dissolving the stirred mixture by slowly adding 12 mL of concentrated methanesulphonic (MSA) acid (Sigma-Aldrich) until a clear Ce (III) solution was obtained. The final concentration of MSA was 4M.

3.3 System start-up and shut-down

The following procedures for start-up and shut-down were used for both the RHVFC and the RHCFC.

Start-up:

1. The pressure of the hydrogen valve was set to 1 bar.

2. The hydrogen supply was connected to the inlet on the anode side (upper-cell connection) and the outlet (lower-cell connection) was connected to the crossover collector which was connected to a vent line that terminated in the gas extraction hood.

3. Hydrogen was passed through the anode side at 5 mL/min and the connections checked for hydrogen leaks. After which hydrogen flow rate was adjusted to the chosen rate for the experiment.

4. The catholyte was supplied to the cathode side (lower-cell connection) through tubing that went from the electrolyte reservoir to the cell via the peristaltic pump. The solution exited the cell from the outlet (upper-cell connection) and returned to the reservoir. The electrolyte reservoir was stirred during experiments.

5. The electrolyte was pumped through the cathode side at a rate of 20 mL/min and the connections checked for leaks. After which the electrolyte flow rate was adjusted to the chosen rate for the experiment.

6. The electrode connections were made with the potentiostat.

7. A perspex screen was placed in front of the experimental set-up for safety reasons.

Shut-down:

1. The hydrogen valve was turned off and all the hydrogen was allowed to flow out of the system until the flow controller software detected no more hydrogen.

2. All the catholyte was allowed to flow back to the reservoir at high flow rate (150 mL/min) in order to minimise electrolyte loss.

3. The electrolyte inlet and outlet lines were removed from the reservoir which was kept tightly closed afterwards.

4. Deionised water was pumped through the cell in order to get rid of remaining electrolyte in the flow channels. This process was repeated twice or until the deionised water ran clear out of the cell.

5. The cathode side was checked for crossover and nitrogen was passed in order to push any remaining electrolyte to the crossover collector.

3.4 DC data acquisition

3.4.1 Charge/Discharge cycles

All charge and discharge cycles were performed using the following procedure:

1. The OCV of the cell was monitored for around 5 min prior to the charging process.

2. The system was charged using a chronopotentiometry function (galvanostatic mode) at constant current. The charge cycle stopped once the cell potential reached the upper cut-off voltage of 1.3 V for the RHVFC or 1.9 V for the RHCFC.

3. The OCV of the cell was monitored for around 30 min until it stabilised. On average, the OCV was 1.26 V and 1.71 V for the RHVFC and RHCFC respectively.

4. The cell was discharged using a chronopotentiometry function at constant current. The discharge cycle stopped once the cell potential reached the lower cut-off voltage of 0.4 V or 1.0V for the RHVFC and RHCFC respectively.

5. The OCV of the cell was monitored for around 30 min until it stabilised. On average, the OCV was 0.99 V and 1.52 V for the RHVFC and RHCFC respectively.

3.4.2 State of Charge (SOC) determination

1. Determination of 100 % SOC for either cell was established when the charging cut-off limit (1.3 V for the RHVFC or 1.9 V for the RHCFC) is reached when being charged at 5 $\mathrm{mA\,cm^{-2}}$.

2. Using this charge cycle the maximum experimental capacity could be obtained.

3. 0 % SOC was defined for either cell when the discharging cut-off limit (0.4 V for the RHVFC or 1.0 V for the RHCFC) was reached when being discharged at 5 mA cm^{-2}.

4. All intermediate SOC were reached by first calculating the desired fraction of the experimental maximum capacity. Followed by determining the charging time necessary at a given applied current using Equ. 3.1 where Q is the capacity.

$$Q = i \times t \tag{3.1}$$

3.4.3 Power data acquisition

At a given SOC, the following procedure was followed:

1. The OCV of the cell was monitored for 30 s and is here referred to as E_i.

2. At start -100 mA was applied for 5 s followed by 30 s rest.

3. The cell was held at E_i until the current dropped below 5 mA followed by a 30 s rest period.

4. Steps 2 and 3 were repeated by increasing the discharge current by 100 mA each time until the potential of the cell dropped to 0.3 V at step 2.

For each discharge step, the last measurement would be recorded for potential, current and power. The power data is presented in this work in the form of power density as a function of current density.

3.4.4 Cyclic Voltammetry (CV)

CV was used in the RHCFC at 50 % SOC as an equal ratio of reductants and oxidants should be present, the procedure was the following:

1. The cerium solution was pumped through the cathode then stopped once it was ensured that the flow channels were filled with electrolyte.

2. The potential scanning rate was selected to be between 10 and 50 mV s^{-1} and the scanning range from 1 to 1.9 V *vs.* SHE with one pass only.

3. Once the test was over, the electrolyte was pumped through again to ensure that fresh electrolyte filled the flow channels before starting the next CV test.

3.5 EIS data acquisition

3.5.1 EIS at OCV

All data was collected using potentio EIS procedures, such as the input AC voltage was controlled while the output AC current was measured. In order to get a single spectra two EIS procedures described in Table 3.2 were combined.

Table 3.2: Parameters used for the two EIS procedures used in order to get a single spectra between 200 kHz and 10 mHz.

Parameters	EIS procedure 1	EIS procedure 2
Voltage amplitude (mV)	20	20
Frequency range (Hz)	200 000 to 1	10 to 0.01
Number of points (logarithmically spaced)	30	20
Measures per frequency	15	3

The data from these two procedures was combined in order to get a high quality single spectra between 200 kHz and 10 mHz.

3.5.2 EIS under load

1. Prior to doing EIS under load, a polarisation curve for the cell must be obtained.

2. For a given current density, the corresponding potential value reading on the polarisation curve represents the potential used for the EIS under load test.

3. The cell was first charged to the desired SOC followed by an OCV period.

4. The EIS under load test was set-up according to the settings described in Table 3.3. As EIS under load tests discharge the cell, thus making the system non-linear, it is best to carry out quick EIS tests. Hence no measurements were collected for frequencies lower than 90 Hz.

Table 3.3: Parameters used for the EIS under load procedure in order to get a spectra between 200 kHz and 90 Hz.

Parameters	EIS under load
Voltage amplitude (mV)	20
Frequency range (Hz)	200 000 to 90
Number of points (logarithmically spaced)	3
Measures per frequency	5

5. An OCV period followed the EIS experiment.

6. Next a charging procedure was used to return to the same SOC as step 3 followed by an OCV period.

3.6 Conclusions

This Chapter has presented all general experimental procedures used in this work. If changes are made to these procedures, they will be discussed in the relevant Chapters.
The reference electrode positioning work, being research activity itself, will be discussed in greater detail in Chapter 4.

Table 3.1: List of all equipment used in the present work.

Item	Specifications	Manufacturer
Chemicals		
Vanadium (IV) oxide sulphate hydrate 97%		Sigma-Aldrich
Sulphuric acid 5 M solution		Fluka Analytical
Ce(III) carbonate		Sigma-Aldrich
Methanesulphonic acid 99.9%		Sigma-Aldrich
Cell Components		
End plate	Aluminium	
Insulating layer	Teflon, 16 mm (Gen1 RHVFC)	
	Polypropylene, 3 mm	RS
Current collector (Gen1 RHVFC)	Copper, 0.45 mm	
Flow channel plate	Graphite with polypropylene binder, 5 mm Product name: PPG85	SGL
	Titanium sheet, 5 mm (Gen2 RHCFC)	Dore Metals
H_2 electrode	Hydrogen electrode/Reformate Cathode 0.2 mm thick Pt loading: 0.5 mg/cm^2	VWR
Cathode electrode	Carbon paper, 0.4 mm (RHVFC) Product name: 10 AA	SGL
	Platinised titanium mesh, 0.7 mm (RHCFC) Product name: G	METAKEM
Gasket	Viton, 0.4 and 1 mm	
Reference electrode container	Teflon cylinder	RS
Connectors	PFA based	Cole-Parmer
Tubing	Chem-Durance, size 25 (Gen1 RHVFC)	Cole Parmer
	Masterflex PTFE ¼ inch (Hydrogen side)	Cole Parmer
	Masterflex PTFE 4mm (Cathode side)	Cole Parmer
Bulk electrolyte and crossover containers	Borosilicate bottles	VWR
	PFA multiple distributor lids	VWR
Ancillary Equipment		
Reference Electrode	Hydrogen reference electrode Hydroflex®	Gaskatel
Potentiostat	Autolab PGSTAT30	Bio-Logic
Booster	Autolab BSTR10A, 10 A	Bio-Logic
Peristaltic pump	77200-50	Cole Parmer
Flow controllers	E-Flow flow meters	Bronkhorst
Softwares		
EC-Lab	Data collection with the potentiostat	
Flow View/Flow DDE	To control the flow meters	
Z-View	EIS data processing	

Chapter 4

Alternative Reference Electrode Positioning Method

4.1 General principals of reference electrodes

For electrochemical devices, a reference electrode (RE) is necessary in order to measure the potential of the working and counter electrode separately, by measuring it with respect to that RE. There are several criteria that need to be considered when selecting a RE:

- The RE should be a non-polarisable electrode, offering a stable potential throughout the duration of the experiment.[1]
- The reaction taking place at the RE should be reversible and display Nernstian behaviour, such that the potential is only dependent on the species concentration.[2,3]
- The RE design and reactants should be compatible with the experimental cell it is going to be used in, i.e.: mercury containing REs should not be used with platinum based electrodes due to the risk of catalyst contamination.[1,4]

The standard hydrogen electrode (SHE), also referred to as the normal hydrogen electrode or the reversible hydrogen electrode, has by convention a potential of 0 V, therefore providing a reference potential for all other redox couples.[2] It is defined as the potential for the reaction described in Equation 4.1, where molecular hydrogen is oxidised to its hydrated ionic form.[2]

By definition the concentration of hydronium in an ideal solution should be 1 M, leading to an activity of unity and the hydrogen gas supplied should be at 1 bar.[2]

$$H_2 + 2\,H_2O \rightleftharpoons 2H_3O^+ + 2\,e^-,\ E^0 = 0\ V \tag{4.1}$$

As represented in Fig. 4.1 the SHE typically contains a platinum wire or sheet coated with a layer of highly dispersed large surface area platinum.[2,4] The platinum is in contact with both the electrolyte and the hydrogen gas so that it catalyses the reaction described in Equ. 4.1. The RE in Fig. 4.1 is used as a half-cell and is connected to a working electrode.

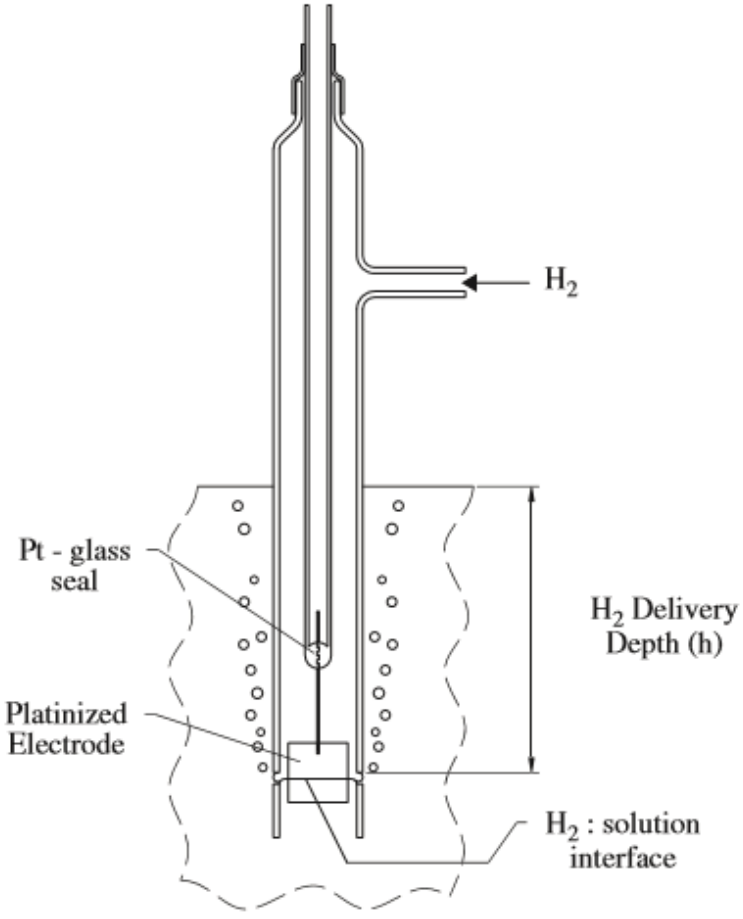

Figure 4.1: Schematic of a Standard Hydrogen Electrode. Reproduced from[1]

There are numerous types of hydrogen based RE available. An alternative to the SHE is the self-contained hydrogen electrode (SCHE) which does not require a constant gas supply but contains instead a hydrogen gas bubble that dissolves slowly and can be easily refilled.[1,2] Additionally there is also the dynamic hydrogen electrode (DHE) which contains two electrodes,

one evolving hydrogen and the other evolving oxygen. The main assets of the DHE are that it can be used in any pH environment (provided there is no contaminant in the electrolyte it is placed in), at any temperature and is self-contained therefore presenting the same advantages as the SCHE.[1,2] However both the SCHE and the DHE present a potential deviation from the SHE (up to 40 mV) which must be corrected.[1]

4.2 Current RE positioning methods

As presented in the literature, for PEMFCs and RFBs, it still remains challenging to insert a reference electrode into these systems given their planar cell design.[5] Currently there are two established reference electrode positioning methods that can be used with these devices: the sandwich and the edge methods. Both these configurations are discussed in the following Section. Additionally an alternative RE insertion method developed by Brightman *et al.* for PEMFCs, which served as a model for the new RE configuration developed in this thesis for RFB applications, is also introduced.

4.2.1 Sandwich method

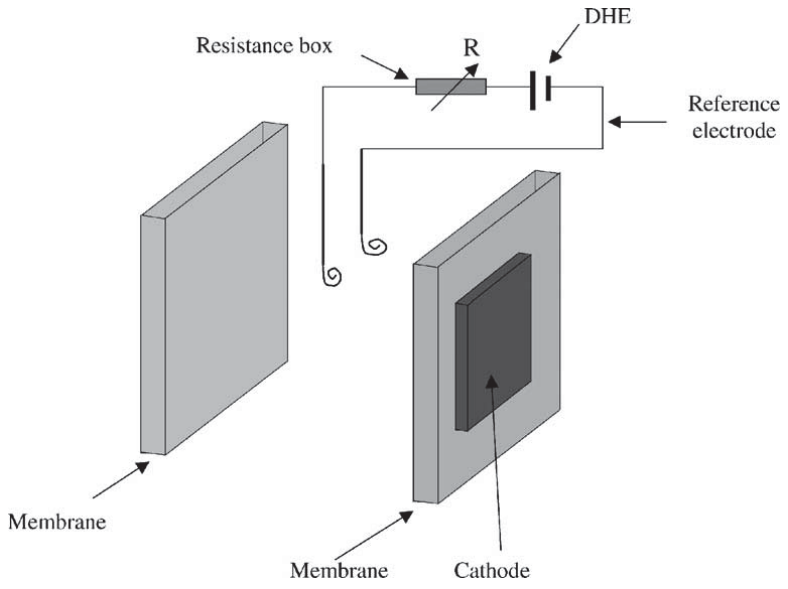

Figure 4.2: Schematic of a sandwich type reference electrode positioning method, placing a dynamic hydrogen electrode between two Nafion membranes. Reproduced from[6]

Figure 4.2 displays the sandwich method of positioning a DHE in a PEMFC also referred to as the internal method.[6] As shown in the diagram, it consists of placing the RE between two Nafion membranes. However this method presents drawbacks such as the increase of ohmic losses by the insertion of a secondary membrane into the cell.[6] Moreover the presence of the RE can lead to a non-uniform current distribution in the cell as well as affecting water transport in the membrane leading to large performance losses.[6–8]

4.2.2 Edge method

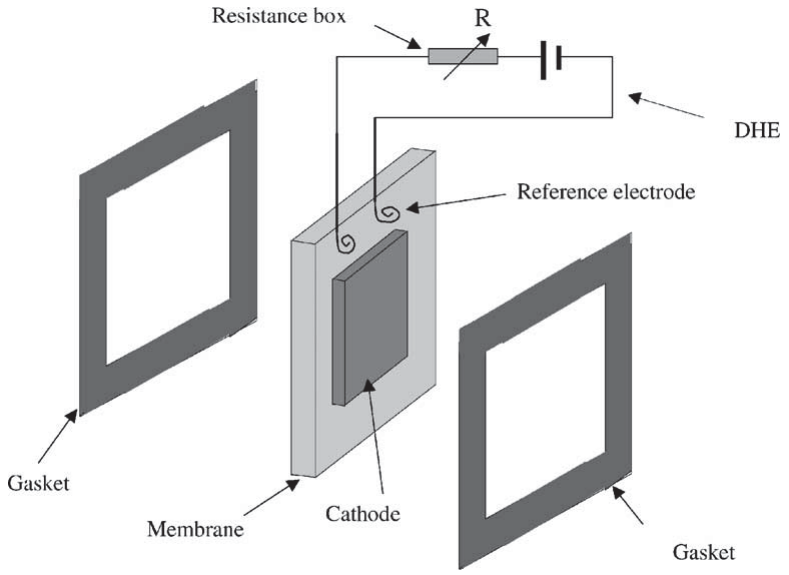

Figure 4.3: Schematic of an edge type reference electrode positioning method, placing a dynamic hydrogen electrode in contact with the Nafion membrane above the active surface area. Reproduced from[6]

Figure 4.3 displays the edge method of positioning a DHE in a PEMFC, also referred to as the external method.[6] In this configuration, the RE is placed in contact with the Nafion membrane, just above the active surface area and held in place by gaskets on each side of the membrane.[6] Dehydration of the membrane and thus poor ionic conductivity can be a challenge with this design, hence the outer region of the membrane in contact with the RE must be kept humidified.[6,9]

4.2.3 Alternative method

For the purpose of the work presented here, Brightman *et al.*'s.[8] alternative method of positioning a reference electrode in a PEMFC will be discussed. As shown in Fig. 4.4, one end of a salt bridge is inserted through the end plate, all the way to the membrane, while the other end is connected to a container filled with a 0.5 M sulphuric acid solution where the RE is immersed; allowing an ionically conductive path between the membrane and the RE. The salt bridge consists of a Nafion sheet encapsulated in a PTFE tube, filled with deionised water in order to ensure maximum conductivity of the membrane material.

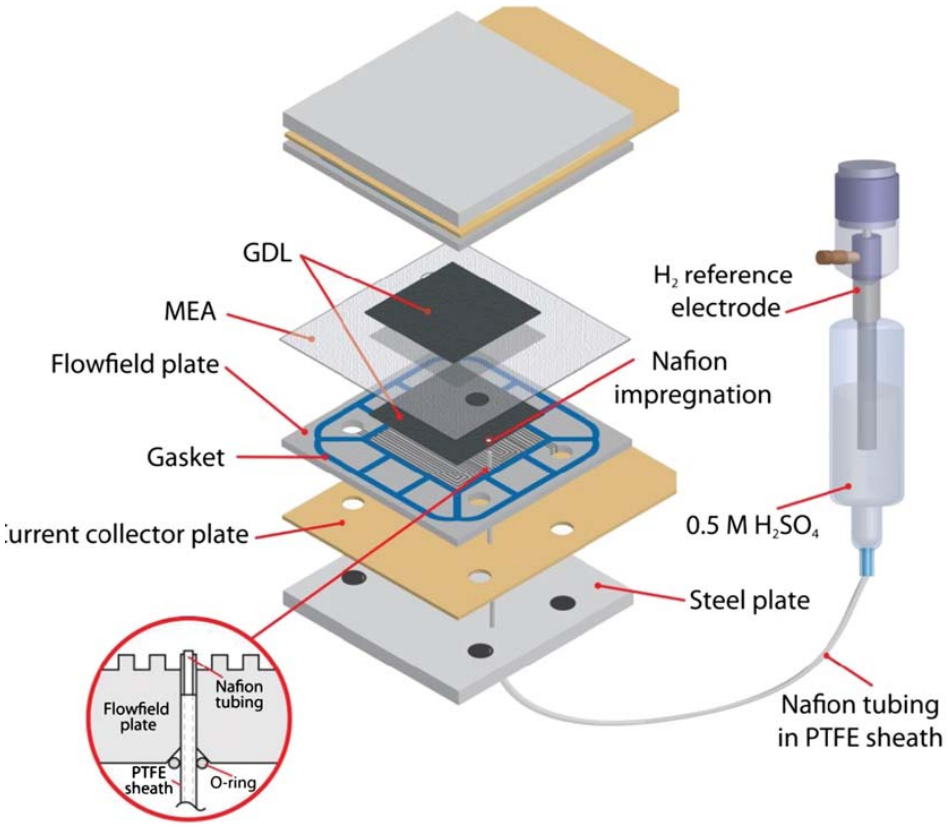

Figure 4.4: Schematic of the reference electrode positioning method developed by Brightman *et al.* Reproduced from[8] with permission from Elsevier.

It was demonstrated that, using this set-up, issues seen with the sandwich and edge type positioning methods such as inhomogeneous current and potential distribution, higher ohmic losses and membrane dehydration can be avoided.[8] Hence a similar RE positioning approach was adapted to RFBs and will be explained in the following Chapter.

4.3 Experimental set-up and methodology

The difficulty of inserting a reference electrode into planar electrochemical devices without disturbing its operation has already been introduced. In order to develop and test the alternative RE positioning method the Regenerative Hydrogen-Vanadium Fuel Cell (RHVFC) was used. However this Chapter will not be discussing the decoupled measurements obtained which will be presented in Chapter 5. The general cell assembly protocol without the RE set-up is presented in Chapter 3.

Figure 4.5 presents the RHVFC assembly with the RE set-up used in this work. A Hydroflex (Gaskatel) RE, which is a SCHE was used; unlike the SHE, this RE comes with its own supply of hydrogen in the form of cartridges that can be utilised for six months at a time. As it can be seen in the diagram, the RE is placed in a PTFE container containing a 0.5 M sulphuric acid solution, which is connected to the cell through an ionically conductive path. This salt bridge is established by inserting a 6.4 mm diameter PTFE tube (Cole-Parmer) through the end plate all the way to the membrane. First testing showed that air bubbles can arise at the membrane interface when the electrolyte is directly poured into the PTFE container. Thus, a smaller PTFE tube of 4 mm diameter (Cole-Parmer), represented in green in the diagram, was inserted into the first tubing, allowing the solution to be syringed into the smaller tubing. This secondary tubing allowed the elimination of any air bubbles, ensuring a stable ion conduction path. No diffusion of electrolyte was observed from the reference electrode container at either electrode.

Once the salt bridge is established, a stable potential was obtained for the Hydroflex RE. According to the literature, a potential deviation up to 40 mV can be observed from the expected 0 V *vs. SHE* due to small polarization losses.[1,2] A period of 24 and 48 hours for the RHVFC and the Regenerative Hydrogen-Cerium Fuel Cell (RHCFC) respectively was necessary to allow the RFB to settle due to the redistribution of pressure in the cell after assembly. Therefore all half-cell measurements were collected after this equilibration period.

The RE set-up was implemented on both the cathode and anode side of the cell. However half-cell measurements were collected at one electrode at a time i.e. when cathode measurements

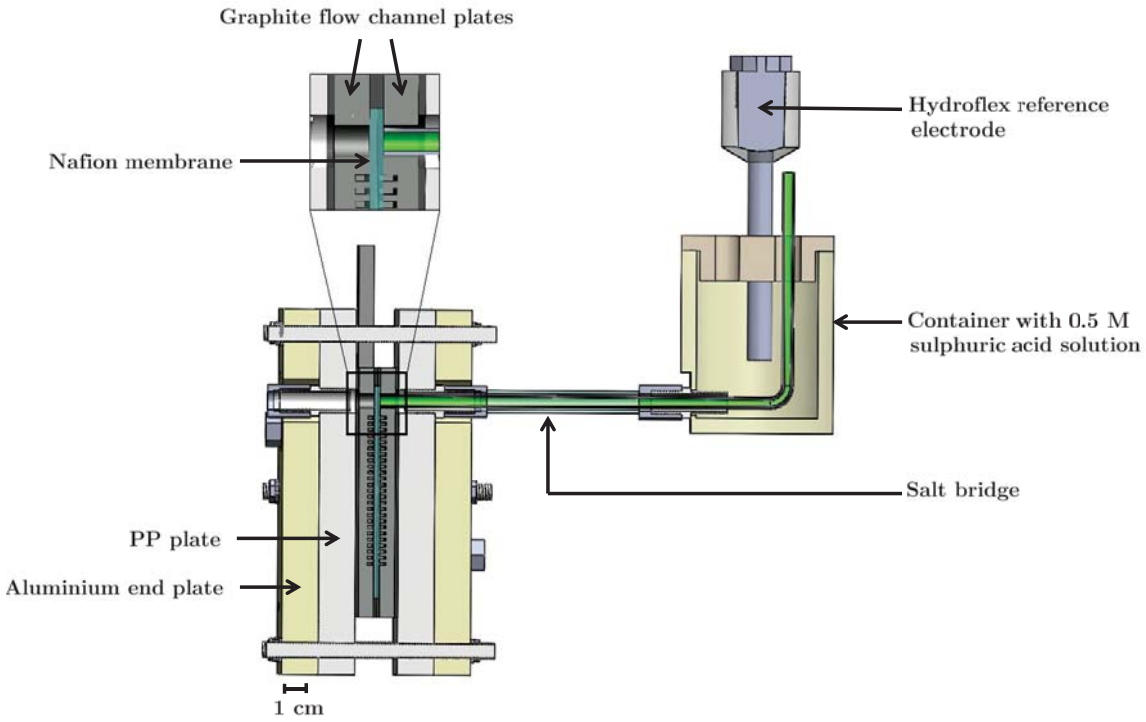

Figure 4.5: Schematic of the RHVFC with the integration of the reference electrode set-up.[10]

were obtained the RE was placed on the cathode side, and vice versa.

4.4 Results and Discussion

Monitoring the decoupled reference electrode potential at OCV for 24 hours, as presented in Fig. 4.6, shows that it is stable over that duration with a standard deviation as small as 300 µV. As mentioned in the experimental section above, the potential of the RE could deviate up to 40 mV from the 0 V *vs. SHE* due to small polarisation losses.

EIS data collected using the RE set-up demonstrated consistent results. Fig. 4.7 displays a whole cell EIS spectra collected with no RE present, comparing it to whole cell EIS spectra collected when the RE is on the vanadium side or the hydrogen side. The results show that all three spectra match as expected, with only the high frequency intercept differing slightly for the spectra collected with the RE on the vanadium side; the high frequency intercept is 4.63 $\Omega\,cm^{-2}$ for the spectra collected with no RE and when the RE is on the hydrogen side, whereas it is 4.65 $\Omega\,cm^{-2}$ when the spectra is collected with the RE on the vanadium side.

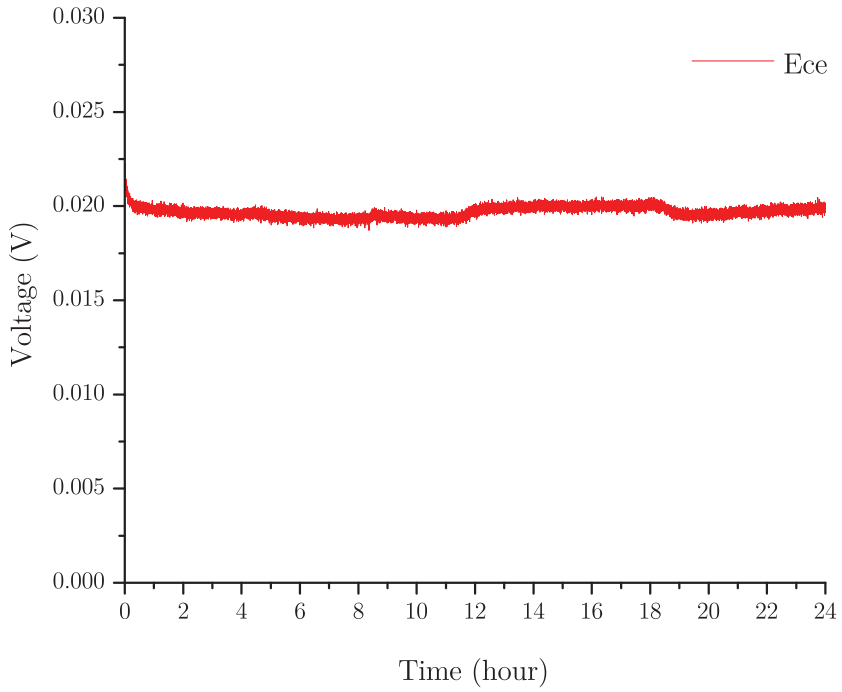

Figure 4.6: Reference electrode potential monitoring test at OCV for 24 hours.

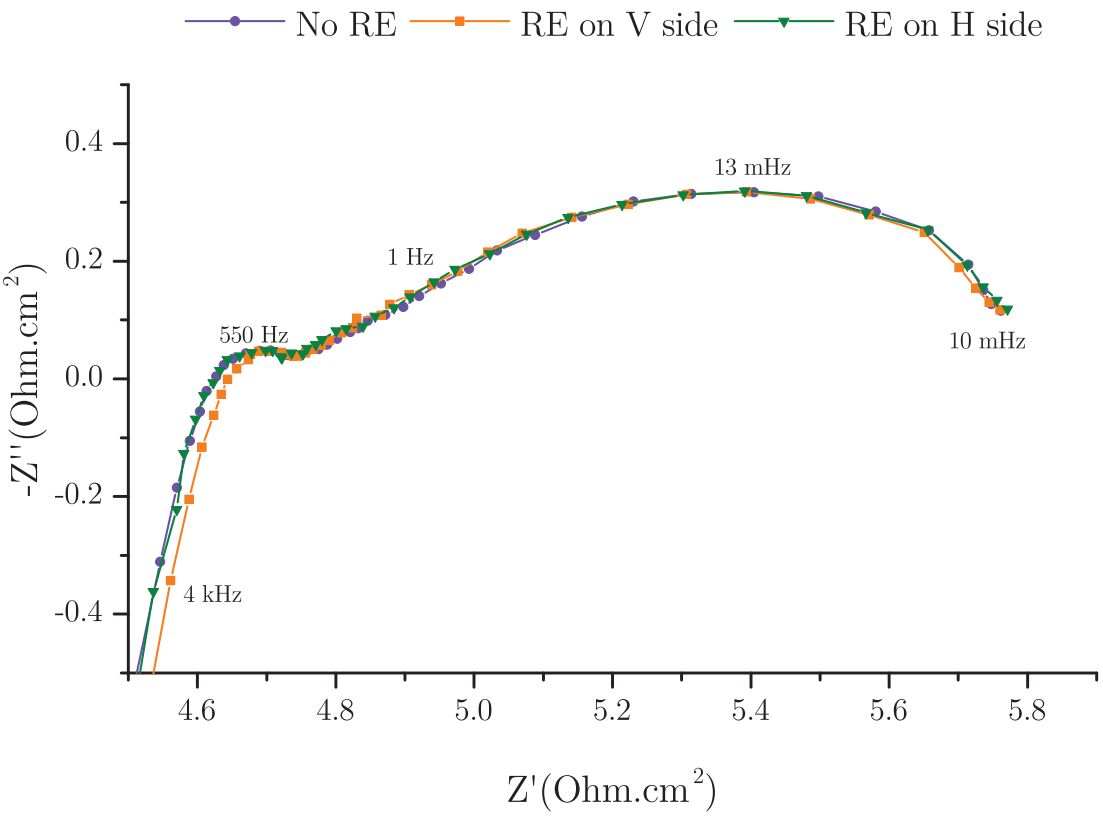

Figure 4.7: RHVFC whole cell EIS spectra at OCV obtained without a RE, with a RE on the Vanadium side and with a RE on the Hydrogen side (frequency range: 200 kHz to 10 mHz).

However, looking at Fig. 4.8, which displays the whole cell spectra along with the half-cell ones collected when the RE is on the vanadium side, it is clear that the hydrogen side spectra is inexact. Indeed it presents several looping effects that suggests it should be disregarded. A similar behaviour is displayed for the vanadium side spectra when collected using the RE on the hydrogen side.

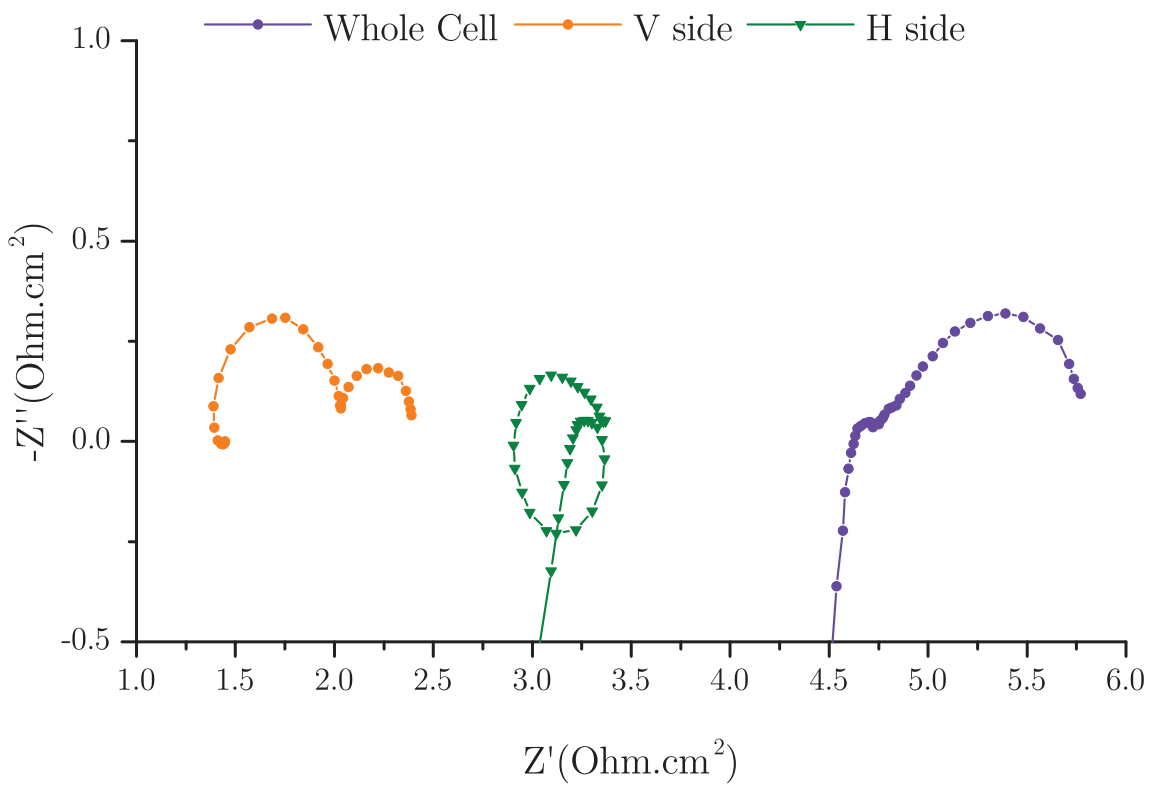

Figure 4.8: RHVFC half-cell and whole cell EIS spectra at OCV collected with a RE on the vanadium side (frequency range: 200 kHz to 10 mHz).

From Fig. 4.9 it is clear that the whole cell spectra, and the half-cell ones for the vanadium and hydrogen electrodes, obtained when the RE is on the same side as the electrode of interest present different behaviours. It is proposed that the looping effects observed in Fig. 4.8 arise from the uninsulated graphite exposed in the ionic bridge in Fig. 4.5. As the EIS data is collected, the conductive graphite causes electrical interference, making the data from the half-cell placed opposite to the one where the RE is placed, unusable.

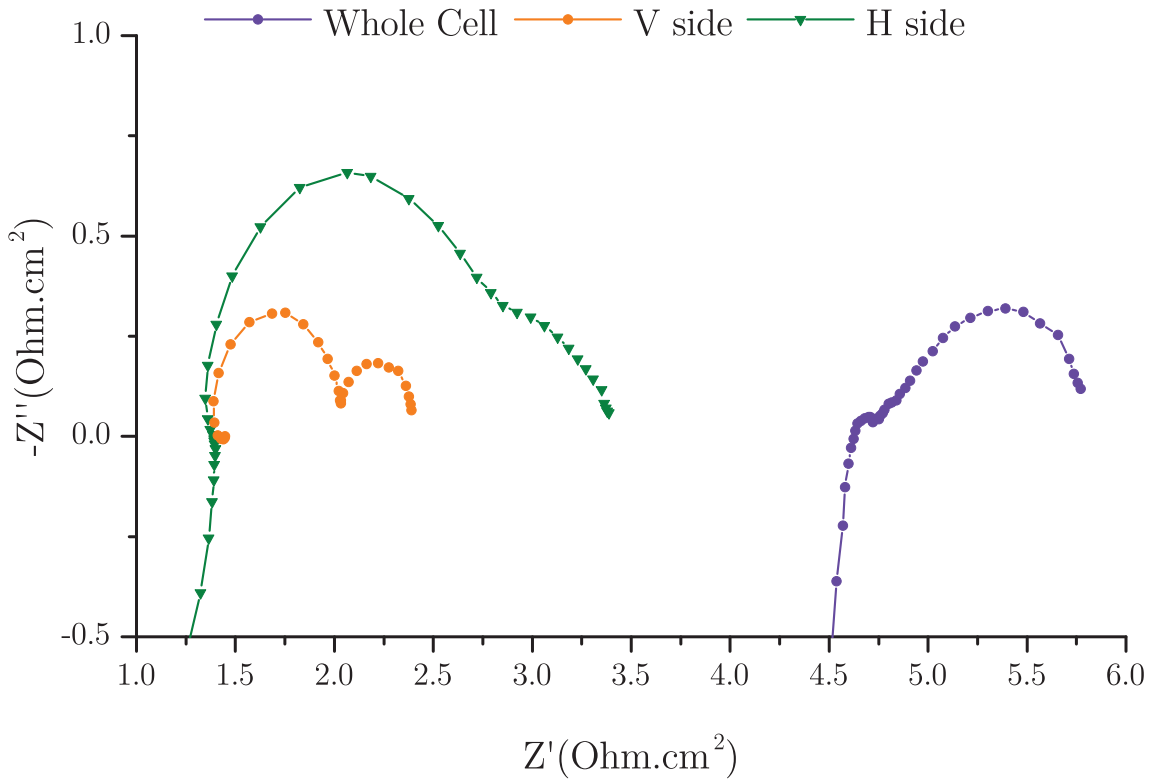

Figure 4.9: RHVFC half-cell and whole cell EIS spectra at OCV collected with a RE on the vanadium side and hydrogen side (frequency range: 200 kHz to 10 mHz).

For the Regenerative Hydrogen-Cerium Fuel Cell (RHCFC), the graphite plates were replaced by titanium. The reference electrode hole in the titanium plate was coated with PVDF to insulate the metal. Hence the data collected for the RHCFC with the RE on the cerium side as displayed in Fig. 4.10 does not show this interference effect on the hydrogen side. Unfortunately, the graphite material used for the RHVFC contains a PVDF binder which prohibits the use of PVDF to insulate the reference electrode hole. Once the PVDF coating is done, the plate needs to be heated above 177 °C. This step would also melt the PVDF binder in the graphite plate.

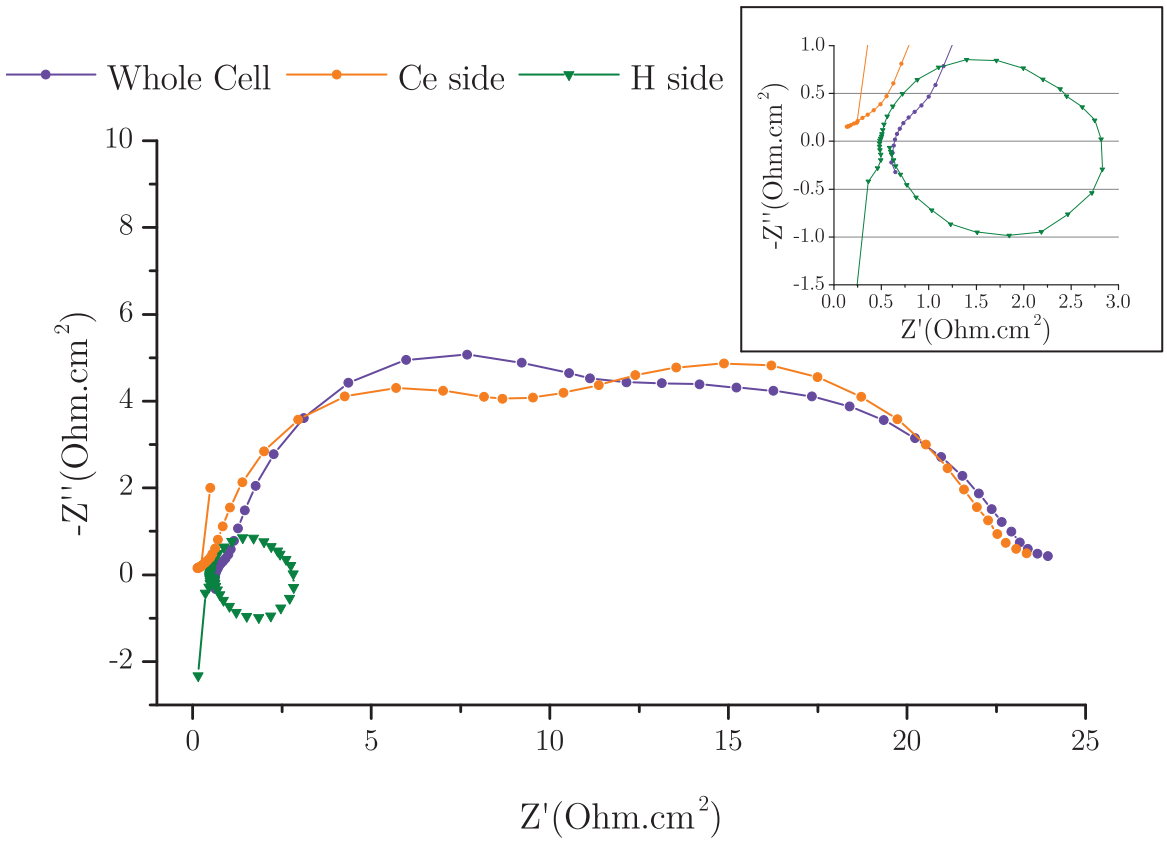

Figure 4.10: RHCFC half-cell and whole cell EIS spectra at OCV collected with a RE on the vanadium side and hydrogen side (frequency range: 200 kHz to 10 mHz).

Figure 4.11 A and B present the residual of the real and imaginary part respectively for the cerium and hydrogen half-cells in the RHCFC. The residual is obtained by subtracting the real/imaginary value of the half-cell spectra obtained when the RE is on the opposite side of the electrode of interest from the real/imaginary value of the half-cell spectra when the RE is on the same side. It can be observed that, for both half-cells, the residual of each half-cell is similar to the other. For the real part residuals, they are similar for both half-cells for higher frequencies up to 30 Hz, beyond which they diverge. The imaginary residuals are almost identical from higher frequencies to 155 Hz, after which they differ in magnitude but display a similar trend. Figure 4.11 also highlights that the difference in value between the spectra collected when the RE is on the same side as the electrode of interest and on the opposite side can be up to 2.0 $\Omega\,cm^{-2}$ for the real part and 0.75 $\Omega\,cm^{-2}$ for the imaginary part. Although a clear data set can be obtained when the reference electrode hole is insulated, it is best to use the spectra collected when the RE is placed on the same side as the electrode of interest, to minimise the

impact of additional membrane impedance.

The ability to obtain these decoupled results is further validation of the RE design and assembly. The nature of these losses will be further discussed in Chapter 5 for the RHVFC and in Chapter 6 for the RHCFC.

A

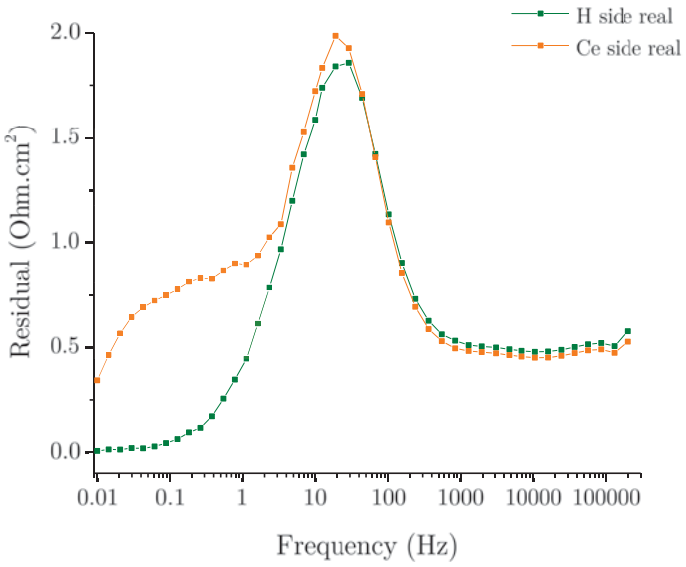

B

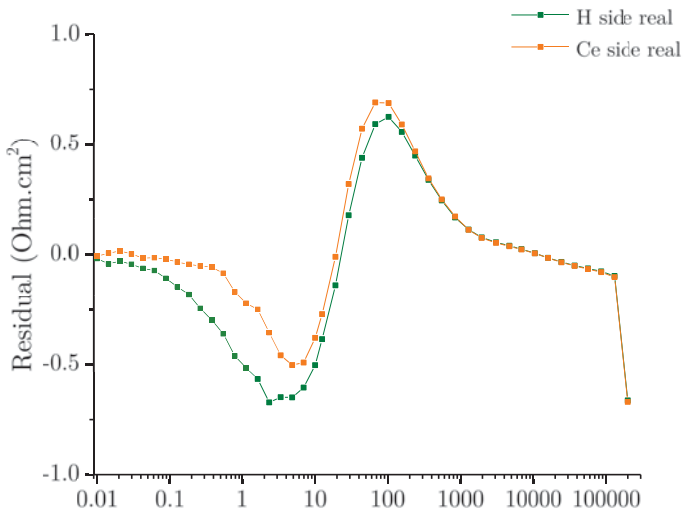

Figure 4.11: Plots of the residual against the frequency of A) the real part of the cerium and hydrogen half-cell B) the imaginary part of the cerium and hydrogen half-cell.

In order to fully confirm the validity of the current RE positioning method, it is important to compare EIS results with direct current (DC) data. From Chapter 2, it is known that the

gradient of the linear region of the I-V curve should give predominantly the ohmic resistance with some activation and mass transport contribution. However this resistance value can also be extracted from EIS.

An I-V curve was obtained for the vanadium, hydrogen and whole cell potential, shown in Fig. 4.12. From the plot, it can be seen that the region between 0 mA cm^{-2} (at OCV) and 80 mA cm^{-2} appears to be linear; this also implies that the initial activation polarisation expected at small current densities cannot be observed here, possibly due to very large ohmic losses. The gradients of the linear fit to these potential curves in that region are 5.7 Ω cm^{-2}, 2.1 Ω cm^{-2} and 3.6 Ω cm^{-2} for the whole cell, vanadium electrode and hydrogen electrode respectively.

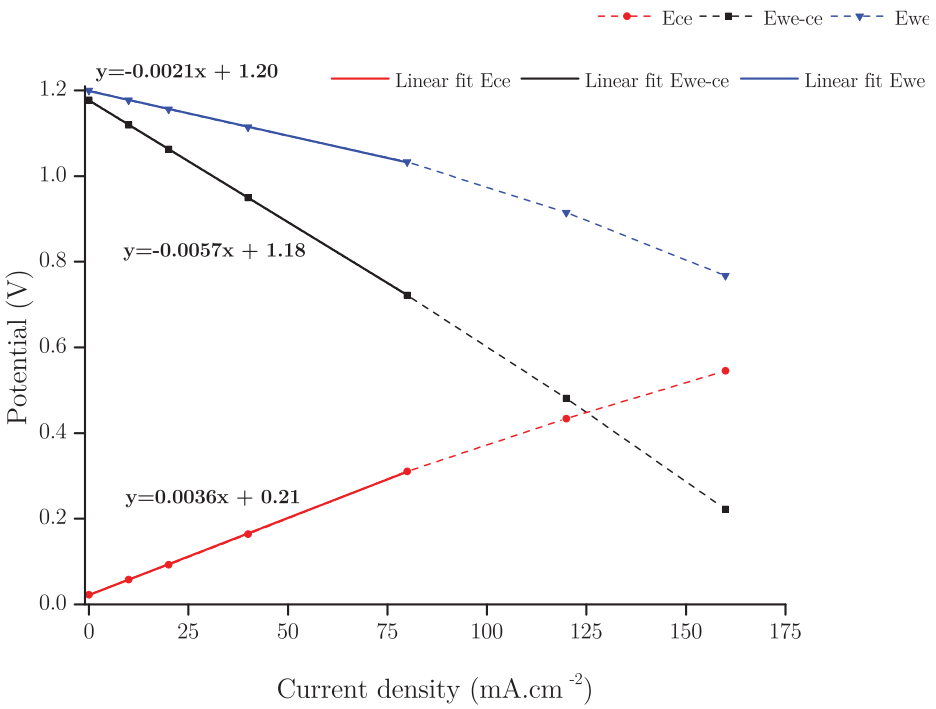

Figure 4.12: Hydrogen, vanadium and whole cell potentials as a function of current density, and the linear fit to each curve in the region of 10 to 80 mA cm^{-2}.

EIS under load was carried out using the protocol described in Chapter 3. This reveals how the different losses change as a function of current density for the RHVFC. Fig. 4.13 displays EIS under load data for the whole cell spectra for current densities between 10 and 60 mA cm^{-2}. The spectra were fitted with an equivalent circuit model in order to estimate the total resistance of the whole cell. Unfortunately it was not possible to fit the EIS spectra collected at 60 mA cm^{-2}

as the data is too noisy. The total whole cell resistance varied between 5.0-5.3 $\Omega\,cm^{-2}$ which is close to the 5.7 $\Omega\,cm^{-2}$ value found with the DC data. The nature of the whole cell, vanadium and hydrogen half-cells losses will be discussed in Chapter 5.

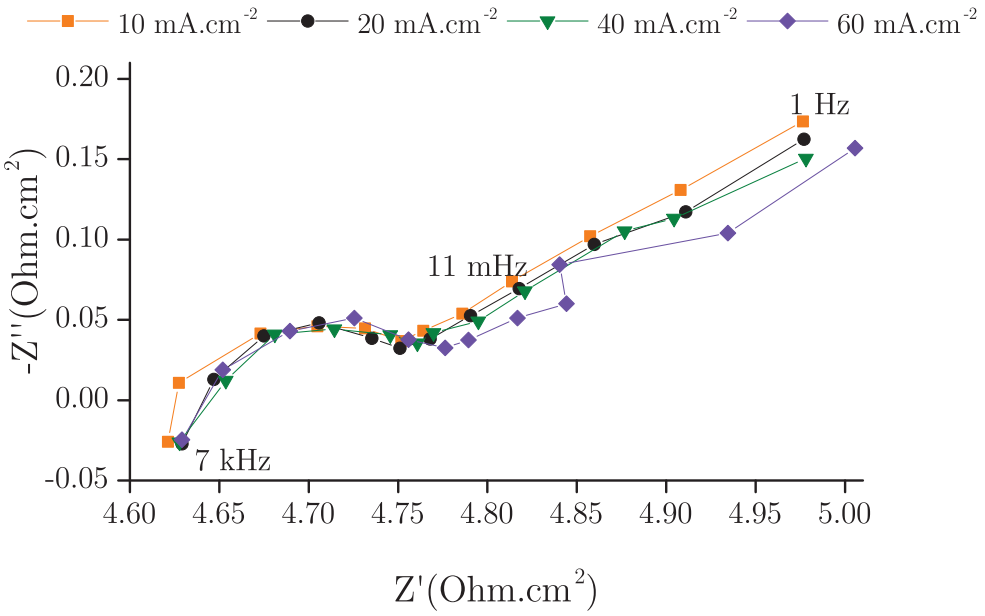

Figure 4.13: Whole cell EIS under load for the RHVFC at 100 mL/min vanadium flow rate and 100 mL/min hydrogen flow rate at an undefined SOC (frequency range: 7 kHz to 1 Hz).

Figure 4.14 displays the EIS under load results for the vanadium half-cell for the same current density range as the whole cell. Once again the fitted data gave a total resistance value for the vanadium cathode of 2.0-2.1 $\Omega\,cm^{-2}$ which again matches with the 2.1 $\Omega\,cm^{-2}$ value extracted from the half-cell polarisation curve.

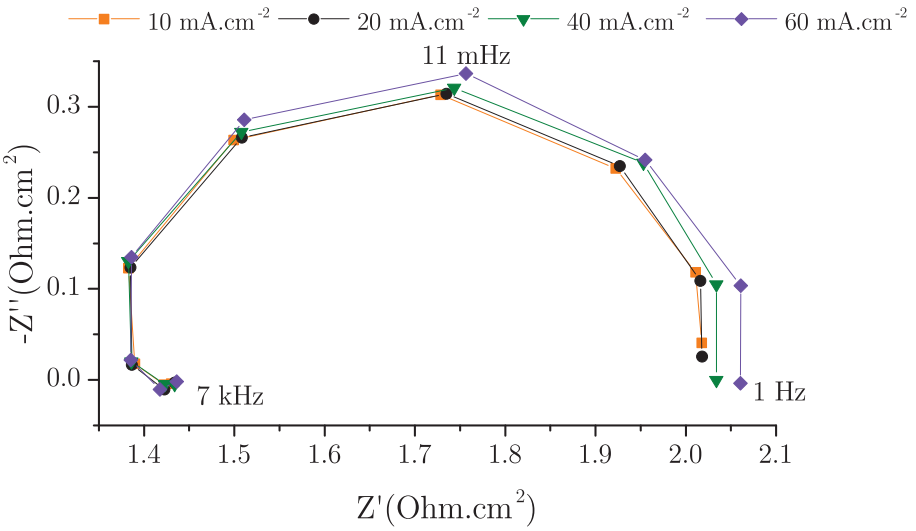

Figure 4.14: Vanadium side EIS under load at 100 mL/min vanadium flow rate and 100 mL/min hydrogen flow rate at an undefined SOC (frequency range: 7 kHz to 1 Hz).

Finally Fig. 4.15 displays the EIS under load results for the hydrogen half-cell for the same current density range as the whole cell. The total resistance value obtained from the EIS data varied between 3.1-3.3 $\Omega\,cm^{-2}$ compared to 3.6 $\Omega\,cm^{-2}$ from the DC data.

Overall, it can be seen that there is a sufficiently good match between the DC data and the EIS results demonstrating the successful operation of the RE set-up.

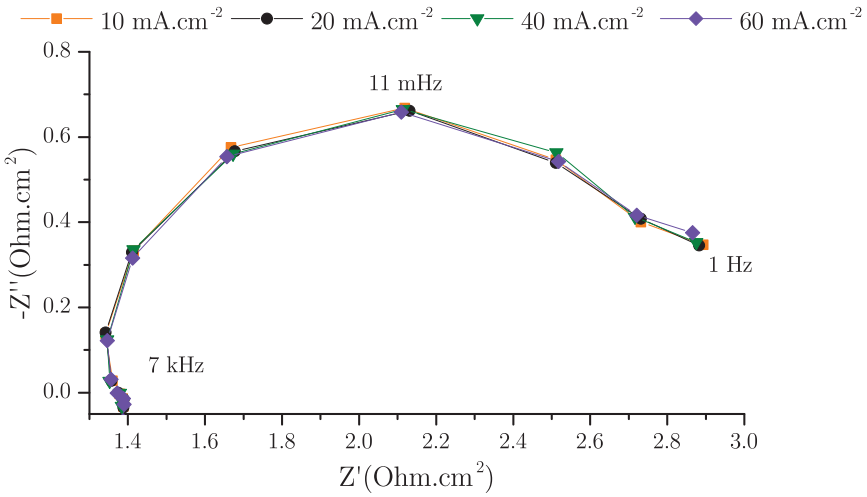

Figure 4.15: Hydrogen side EIS under load at 100 mL/min vanadium flow rate and 100 mL/min hydrogen flow rate at a random SOC (frequency range: 7 kHz to 1 Hz).

4.5 Conclusions

The validity of an alternative RE positioning method, inspired by the one developed by Brightman *et al.*, was established in this Chapter. Unlike the mainstream sandwich and edge type RE positioning methods, the method presented in this work affects neither the operation of the cell nor the measurements collected.

The RE potential stability using the salt bridge set-up was demonstrated. Moreover by collecting distinctive half-cell EIS spectra for cathode, anode and whole cell as well as correlating the EIS data with DC data, the successful operation of the RE set-up was established.

The presented set-up should be used in the RHVFC and RHCFC to decouple the cathode and anode processes; these results will be discussed in Chapter 5 and 6 respectively.

References

[1] C. Zoski, *Handbook of Electrochemistry*, 2007, pp. 73–110.

[2] F. S. A. J. Bard, G. Inzelt, *Electrochemical Dictionary*, Springer, 2008.

[3] R. G. Kelly, J. R. Scully, D. Shoesmith and R. G. Buchheit, *Electrochemical Techniques in Corrosion Science and Engineering*, CRC Press, 2002.

[4] V. S. Bagotsky, *Fundamentals of Electrochemistry*, John Wiley & Sons, 2005.

[5] D. S. Aaron, Z. Tang, J. S. Lawton, A. P. Papandrew and T. A. Zawodzinski Jr., *ECS Transactions*, 2012, **41**, 43–51.

[6] G. Li and P. G. Pickup, *Electrochimica Acta*, 2004, **49**, 4119–4126.

[7] B. Andreaus, A. McEvoy and G. Scherer, *Electrochimica Acta*, 2002, **47**, 2223–2229.

[8] G. Hinds and E. Brightman, *Electrochemistry Communications*, 2012, **17**, 26–29.

[9] J. H. Ohs, U. Sauter, S. Maass and D. Stolten, *Journal of the Electrochemical Society*, 2012, **159**, F181–F186.

[10] H. Hewa Dewage, V. Yufit and N. P. Brandon, *Journal of The Electrochemical Society*, 2015, **163**, A5236–A5243.

Chapter 5

Understanding losses in the Regenerative Hydrogen-Vanadium Fuel Cell

The Regenerative Hydrogen-Vanadium Fuel Cell (RHVFC) developed by Yufit *et al.* is presented in Fig. 5.1.[1,2] A solution of V(IV)/V(V) electrolyte is pumped through the cathode in a similar fashion to the all-vanadium redox battery (VRB), while hydrogen is supplied to the anode. For the purpose of the work presented here, hydrogen is not recycled. However in a commercial system, hydrogen would be stored at pressures of a few bar, probably maintained by electrochemical compression either directly inside the flow cell, or external to it.

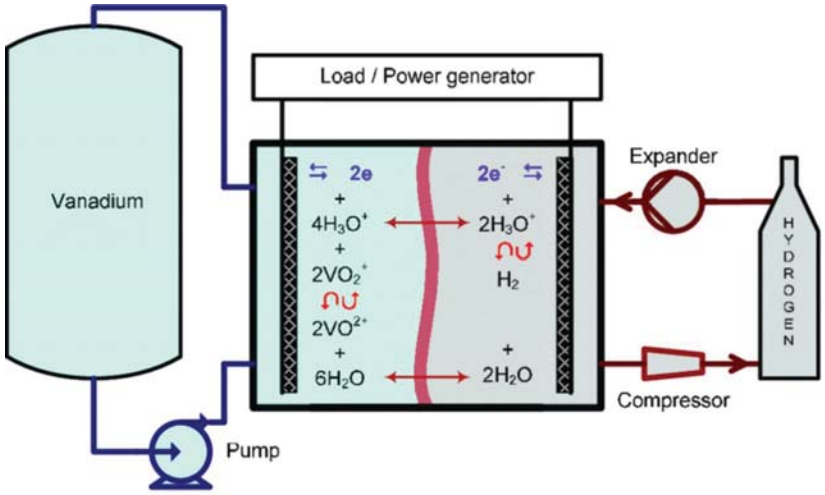

Figure 5.1: Schematic illustration of the RHVFC concept. Reproduced from[2] with the permission of the Electrochemical Society.

Given that the cost of the vanadium represents over 40 % of the total cost of a VRB as shown in Fig. 5.2, the RHVFC offers the benefit of only using half of the vanadium, hence potentially decreasing the overall cost of the system. The benefits of having a hydrogen electrode were already discussed in Chapter 2. The second largest source of cost is the membrane electrode assembly (MEA) which includes the separator and the electrodes. In order to increase the performance and lifetime, and hence reduce the cost of the MEA, understanding of the behaviour and degradation mechanisms in the porous electrodes and ion exchange membrane is crucial. This Chapter focuses on half-cell studies of the RHVFC and the effect of several parameters on its different losses. It will first present preliminary findings and issues faced with cell design and testing. Then it will discuss findings obtained using the reference electrode set-up developed in this research, and presented in Chapter 4.

As described by Equ. 5.1-5.3, during discharge (energy delivery mode) V(V) is reduced to V(IV) and hydrogen is oxidised, whereas during charge (energy storage mode), V(IV) is further oxidised to V(V) while hydrogen is produced and stored.

$$2\,VO_2^+ + 4\,H_3O^+ + 2\,e^- \rightleftharpoons 2VO^{2+} + 6\,H_2O,\ E^0_{cathode} = 0.99\ V \tag{5.1}$$

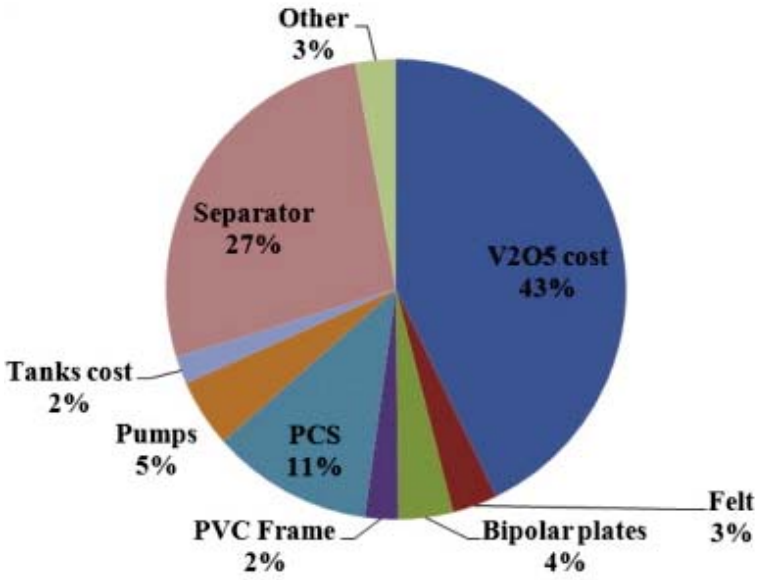

Figure 5.2: Breakdown of total costs of a VRB for a 1 MW/4 MWh system. Reproduced from[3] with the permission of Elsevier.

$$H_2 + 2\,H_2O \;\rightleftharpoons\; 2\,H_3O^+ + 2\,e^-,\; E^0_{anode} = 0\ V \tag{5.2}$$

$$2\,VO_2{}^+ + 2\,H_3O^+ + H_2 \;\rightleftharpoons\; 2\,VO^{2+} + 4\,H_2O,\; E^0_{cell} = 0.99\ V \tag{5.3}$$

5.1 Experimental methods

This Section will describe the different RHVFC versions used for testing in this chapter.

5.1.1 Generation 1

Fig. 5.3 displays the construction steps of the Generation 1 (Gen1) RHVFC. Although not represented in the figure, alignment rods were used during the construction in order to position the different layers correctly in the cell.

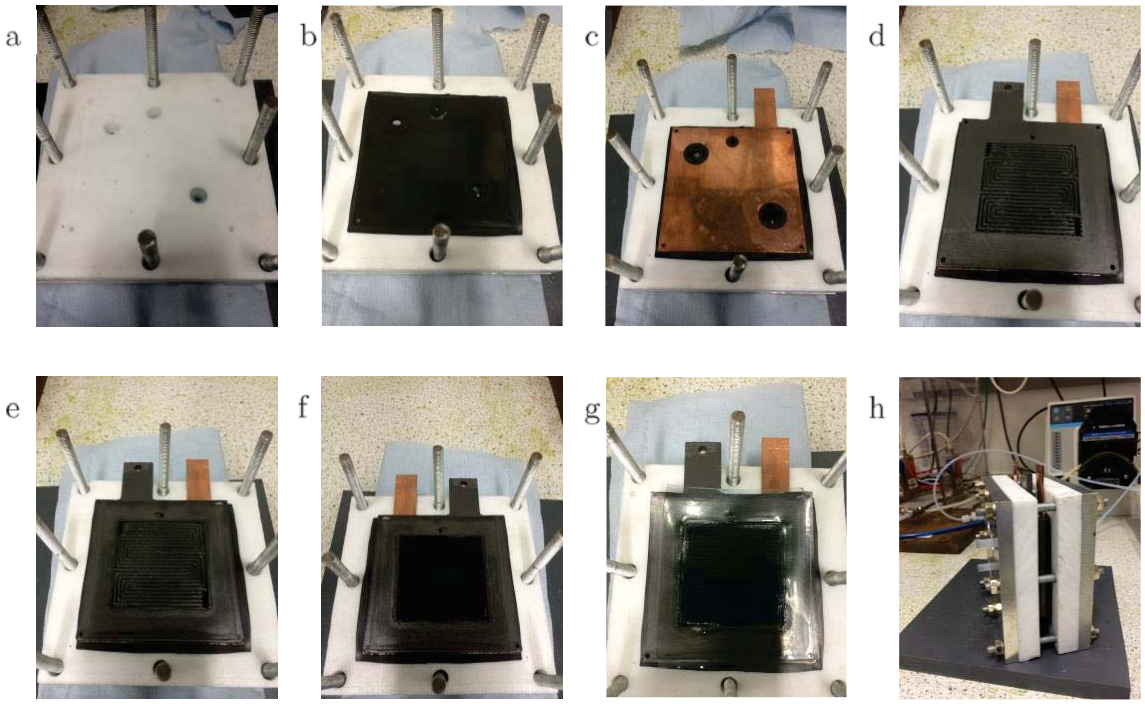

Figure 5.3: RHVFC (25 cm^2) construction steps with a) aluminium end plate and Teflon plate b) one layer of a full size gasket with one layer of o- ring gaskets c) copper current collector d) graphite flow channel plate e) partial gasket only covering the region outside the active surface area f) carbon based electrode g) Nafion membrane h) fully assembled RHVFC.

First a Teflon insulating plate was placed on top of an aluminium end plate (Fig. 5.3 a). A rigid aluminium end plate is necessary as Teflon is a soft material, and hence would otherwise deform. One layer of a full Viton gasket was placed on the Teflon, with additional o-ring gaskets at the inlet, outlet and RE hole positions (Fig. 5.3 b). These additional gaskets were intended to prevent the electrolyte coming into contact with the copper current collector shown in Fig. 5.3 c. However this method did not work consistently, leading to copper corrosion in the cell on some occasions. A graphite plate with double serpentine flow channels was placed on top of the copper current collector (Fig 5.3 d) followed by a partial Viton gasket only covering the region outside the active surface area (Fig. 5.3 e) leaving the active surface area uncovered. The electrode was then placed on top of the flow channel region; either an untreated carbon based electrode or a platinised carbon electrode (with the platinised side facing the membrane) for the cathode and anode side respectively. Finally the Nafion membrane was placed on top of the electrode as depicted in Fig 5.3 g; the membrane was pre-hydrated in deionised water before

use. Once the membrane was in place, all steps from Fig 5.3 a-f were repeated for the other half of the flow cell. Once all the components were layered, the cell was progressively tightened from 4 N.m up to 9 N.m after which the alignment rods were removed. Note that the cell was kept flat on the bench during the tightening process to avoid any displacement of the components. It was only after full assembly was completed that the cell could be placed up-right, as shown in Fig 5.3 h.

5.1.2 Generation 2

The Generation 2 (Gen2) RHVFC was mainly needed due to address the problem of copper corrosion in the Gen1 cell. The design was simplified to exclude the copper current collectors and the Viton o-ring gaskets. The Gen2 cell construction steps can be found in the General Experimental Methods chapter (Chapter 3) and its design was also used for the Regenerative Hydrogen-Cerium Fuel Cell (RHCFC). The reference electrode set-up for this cell was introduced in Chapter 4.

In order to understand the behaviour of the cell, both DC and EIS measurements were carried out. As the Gen2 RHVFC was assembled and disassembled between different sets of experiments (i.e. between testing the cell at various catholyte flow rate and anolyte flow rates), the values obtained for the different losses could vary, reflecting component and assembly variability. Therefore is was judged appropriate to look at the individual resistance values as well as the relative contribution of each process with respect to the total resistance of the cell. All values are displayed in Table 5.2 and will be discussed in this Chapter.

5.2 Results and Discusion

5.2.1 Preliminary results

EIS data collected at 100 % SOC for the system published by Yufit *et al.*,[2] and the Gen1 cell tested in this work, are displayed in the Nyquist plots in Fig. 5.4. Firstly a clear difference in the series resistance (obtained from the high frequency intercept) is observed. The lower

value of 0.02 $\Omega\,cm^{-2}$ found by Yufit *et al.* compared to the 0.65 $\Omega\,cm^{-2}$ found here can be explained as the previous cell had its MEA hot-pressed which would minimize contact resistance between the membrane and the electrodes.[2] Additionally it also used gold plated copper current collectors which would further minimize ohmic losses.[2]

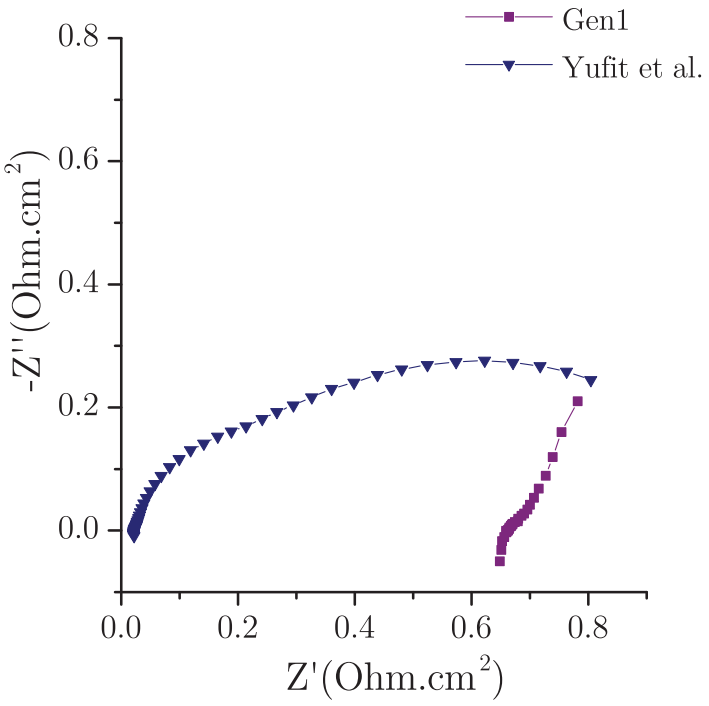

Figure 5.4: Nyquist plot for the RHVFC investigated by Yufit *et al.*[2] and Gen1 at 100 % SOC at 100 mL/min vanadium and hydrogen flow rate (frequency range: 200 kHz to 100 mHz for Gen1 and 6.3 kHz to 100 mHz for Yufit *et al.* cell).

The Nyquist plots also reveal that at least two different processes are seen in both cases. It was established by Yufit *et al.* that the high frequency depressed semi-circle indicated losses that are typically associated with the porosity and roughness of the carbon electrodes.[2] Whereas the lower frequency depressed semi-circle describes diffusion processes in the porous media.[2]

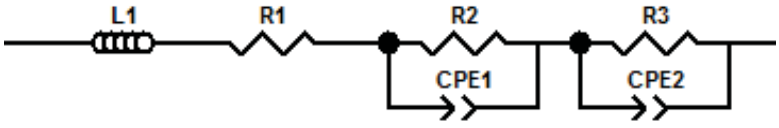

Figure 5.5: Equivalent circuit used by Yufit et al. to model the EIS response at 100 % SOC where L1 represents a high frequency inductor, R the series resistance, R2 and CPE1 the charge transfer process, R3 and CPE2 the diffusion of species in the porous media.[2]

In order to quantify the losses, the equivalent circuit model used by Yufit *et al.* as presented in Fig. 5.5 was used. However this led to very large fitting errors suggesting that it was not appropriate for modelling the data collected from Gen1. Hence the circuit presented in Fig. 5.6 was used instead, which includes a semi-infinite Warburg diffusion element in addition to the model used by Yufit *et al.*; and in which the constant phase elements are replaced by capacitors as they gave smaller fitting errors. L_{wires} is attributed to the inductance of the wires in the cell at high frequency, R_S the series resistance, the double-layer capacitor C_{DL1} and its parallel resistor R_{CT1} the charge transfer reaction of hydrogen, the double-layer capacitor C_{DL2} and its parallel resistor R_{CT2} the charge transfer of vanadium, and finally the semi-infinite Warburg element W_{Diff} describes the vanadium diffusion related losses.

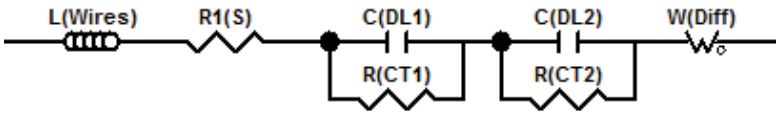

Figure 5.6: Equivalent circuit used to model Gen1 EIS response at 100 % SOC.

The values of the different resistance contributions are given by Fig. 5.7. Both R_{CT1} and R_{CT2} are smaller than the value found by Yufit et al. which was 0.123 $\Omega\,cm^{-2}$ (which is believed to be the charge transfer resistance of the vanadium reaction). Moreover it is clear from Fig. 5.7 that the cell suffers from significant ohmic losses, followed in importance by relatively large vanadium mass transport losses.

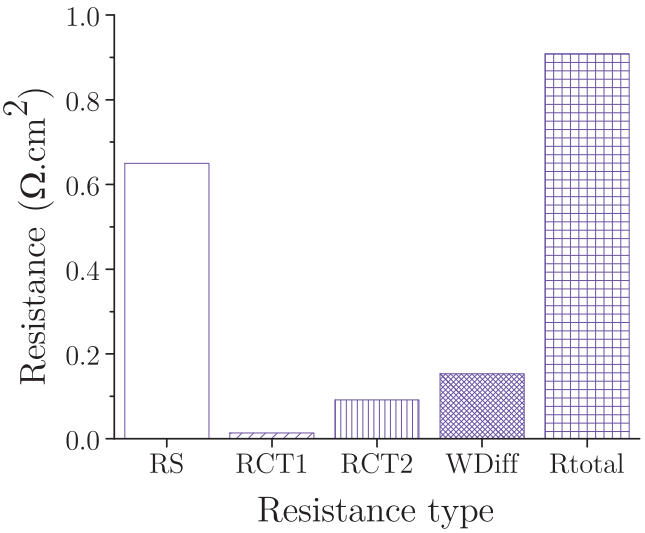

Figure 5.7: Different resistance contribution of the whole Gen 1 cell at 100 % SOC at 100 mL/min vanadium and hydrogen flow rates.

However looking at the time constant values of the different processes presented in Table 5.1, it is not expected to find the time constant of the vanadium charge transfer reaction to be as high as 1.7 s, especially as it is in the same order as the diffusion process (1.5 s). Besides the values found by Yufit et al. for the same process was 23 ms. Nonetheless the small time constant values for $C_{DL1/RCT1}$ of 0.067 ms suggests that this is likely to be associated with charge transfer losses of the hydrogen reaction.

Table 5.1: Fitted parameters, time constant and diffusion values of the different processes for the whole cell at 100 % SOC at 100 mL/min vanadium and hydrogen flow rate.

SOC	R_S	R_{CT1}	C_{DL1}	τ_1	R_{CT2}	C_{DL2}	τ_2	W_{Diff}	τ_{Diff}	D
%	$\Omega\,cm^2$	$\Omega\,cm^2$	mF	ms	$\Omega\,cm^2$	mF	s	$\Omega\,cm^2$	s	$cm^2\,s^{-1}$
100	0.65	0.014	124	0.067	0.092	452	1.7	0.15	1.5	1.09×10^{-7}

These initial results highlight the difficulty of decoupling the different losses when only considering whole cell data. It is likely that the equivalent circuit model used here, although optimised for the data, is still not good enough. Moreover the Gen1 cell suffered from occasional catholyte leaks onto the copper current collectors leading to corrosion, thus affecting the stability of the results. In order to actually decouple anode and cathode losses the reference electrode set-up presented in Chapter 4 was therefore used. The next section will discuss this.

5.2.2 Testing with the reference electrode set-up

First, the copper current collector had to be removed from the cell in order to use the reference electrode as it was not compatible with the presence of the salt bridge. Thus higher ohmic losses are to be expected due to poorer current collection.

As mentioned in Chapter 3, the RHVFC takes up to 24 hours to settle due to the redistribution of pressure in the cell after assembly. In order to monitor these changes and to assess whether the cell was stable before testing, an EIS spectra was collected every half an hour as displayed in Fig. 5.8. It can be observed that right after assembly the RHVFC has a very large total resistance, approximatively 11.3 $\Omega\,cm^{-2}$, compared to 4.2 $\Omega\,cm^{-2}$ after 24 hours. The cell was then re-tightened to 9 N.m as some loosening had occurred after the 24 hours period, the EIS spectra collected subsequently shows a small improvement in series resistance, with the high frequency intercept going from 5.4 $\Omega\,cm^{-2}$ prior to re-tightening, to 5.3 $\Omega\,cm^{-2}$ afterwards.

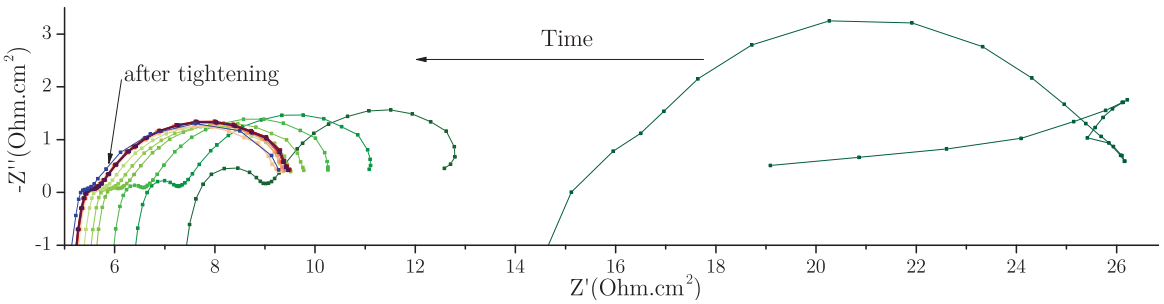

Figure 5.8: 24 hours cell monitoring test after assembling where an EIS spectra was collected at OCV every half-hour (frequency range: 200 kHz to 10 mHz) .

Following the stabilisation of the cell, it was tested under various conditions using the reference electrode set-up in order to observe any change in the overpotentials at either electrode.

Effect of vanadium flow rate

Figure 5.9 A displays the Nyquist plots collected for the vanadium electrode only, for various vanadium flow rates, where two depressed semi-circles can be observed. The higher frequency feature is attributed to kinetic controlled losses in the cathode whereas the lower frequency one is related to diffusion limitations, as will be explained below. From the plot and its inset, it can be seen that both processes decrease as the vanadium flow rate increases. However the

change in electrolyte flow rate has the most effect on the diffusion losses. In order to quantify the resistance changes in the cathode, the data was fitted with the equivalent circuit presented in Fig. 5.9 B where R_S represents the series resistance which corresponds to the high frequency intercept. Then the combined elements R_{CT} and C_{DL} describe the charge transfer resistance of the cathode. Finally the CPE and R_{Diff} model the diffusion behaviour of the electrolyte in the porous electrode.

A

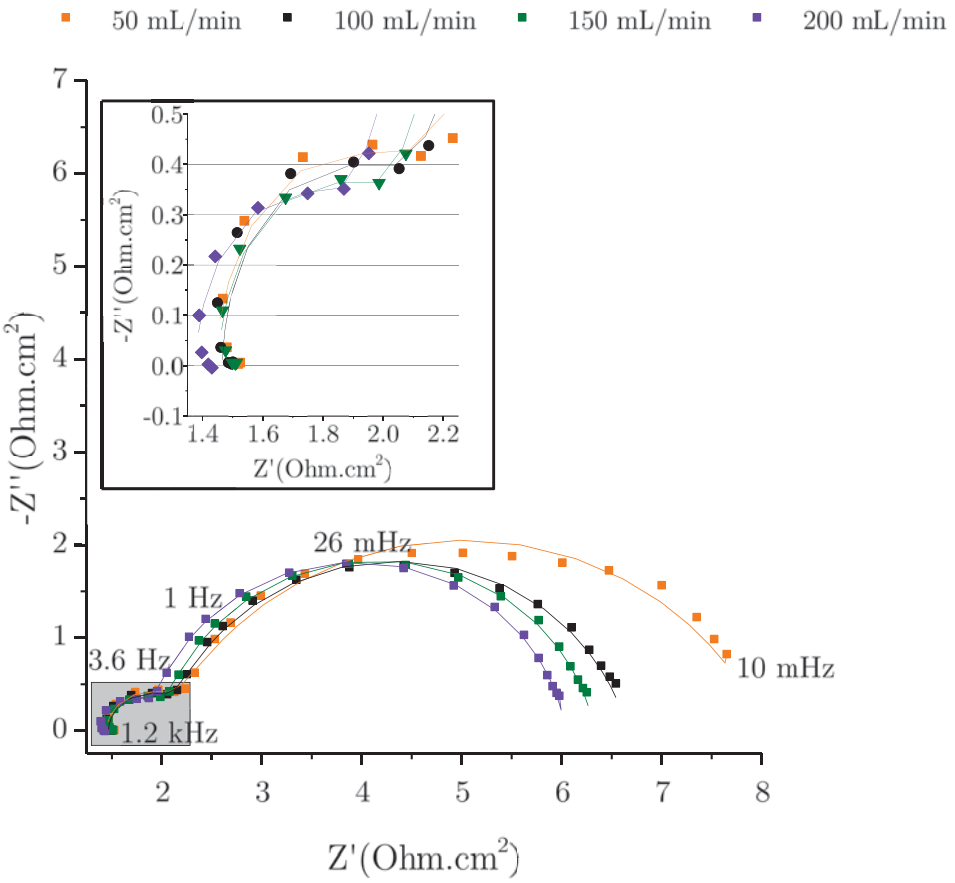

B

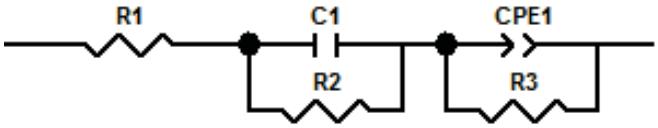

Figure 5.9: A) Nyquist representation of the EIS response at OCV of the vanadium half-cell with the fitted spectra at different vanadium flow rates with a hydrogen flow rate of 100 mL/min (frequency range: 1.2 kHz to 10 mHz). B) Equivalent circuit used to fit the EIS data where R1=R_S, C1=C_{DL}, CPE1=CPE, R2=R_{CT} and R3=R_{Diff}.

Table 5.2: All resistance values for processes in the cathode, anode and whole cell under various conditions.

	1 M Vanadium and 5 M H_2SO_4												0.5 M Vanadium and 5 M H_2SO_4				1 M Vanadium and 3 M H_2SO_4			
	V Flow Rate (mL/min)				H_2 Flow Rate (mL/min)				H_2-N_2 Mix (% of H2)				V Flow Rate (mL/min)				V Flow Rate (mL/min)			
	50	100	150	200	25	50	75	100	25	50	75	100	50	100	150	200	50	100	150	200
Vanadium Half-Cell																				
Series Resistance Rs ($\Omega.cm^2$)	1.5	1.5	1.5	1.4	1.4	1.4	1.4	1.4	1.4	1.4	1.4	1.4	1.4	1.4	1.4	1.4	1.4	1.4	1.4	1.4
Contribution of Rs (%)	18.5	22.0	23.4	23.3	21.7	22.0	22.4	22.7	22.5	22.0	21.9	22.2	19.3	22.6	24.2	25.0	18.4	21.2	27.2	27.9
Charge Transfer Resistance RCT ($\Omega.cm^2$)	0.6	0.6	0.5	0.5	0.6	0.6	0.6	0.6	0.7	0.7	0.7	0.6	1.2	0.5	0.9	0.9	1.1	0.9	0.8	0.7
Contribution of RCT (%)	7.1	8.8	8.4	8.1	9.8	9.4	9.8	9.9	10.2	10.1	10.0	10.0	16.9	8.7	14.9	15.7	15.3	13.6	16.2	14.7
Double-Layer Capacitance (F)	0.4	0.4	0.4	0.5	0.3	0.3	0.3	0.3	0.3	0.3	0.3	0.3	0.1	0.4	0.1	0.1	0.1	0.2	0.2	0.2
Diffusion Resistance Rdiff ($\Omega.cm^2$)	6.0	4.6	4.3	4.1	4.5	4.4	4.3	4.2	4.3	4.4	4.4	4.3	4.6	4.3	3.5	3.3	4.9	4.3	2.9	2.9
Contribution of Rdiff (%)	74.5	69.2	68.2	68.6	68.5	68.6	67.9	67.4	67.3	67.9	68.2	67.8	63.8	68.8	60.9	59.3	66.3	65.2	56.6	57.4
Constant Phase Element ($\Omega^{-1}.s^{\alpha}$)	6.7	6.2	0.6	0.6	5.0	5.2	5.3	5.7	5.4	5.3	5.3	5.4	7.3	5.0	5.7	5.7	7.5	5.0	7.3	5.6
α	0.4	0.4	0.9	0.9	0.8	0.8	0.8	0.8	0.8	0.8	0.8	0.8	0.7	0.7	0.8	0.8	0.7	0.8	0.8	0.8
Total Resistance ($\Omega.cm^2$)	8.0	6.7	6.3	6.0	6.6	6.5	6.4	6.3	6.3	6.5	6.5	6.4	7.2	6.2	5.8	5.6	7.5	6.5	5.1	5.0
τCT (ms)	8.3	8.8	9.0	9.0	7.6	7.5	7.6	7.5	7.4	7.5	7.5	7.4	4.1	7.8	4.3	4.3	6.1	6.4	6.2	6.2
τDiff (s)	1.3	0.9	0.7	0.7	1.2	1.2	1.2	1.2	0.9	0.9	0.9	0.9	1.5	0.8	0.8	0.7	1.8	0.8	0.8	0.6
Hydrogen Half-Cell																				
Series Resistance Rs ($\Omega.cm^2$)	1.2	1.2	1.2	1.2	1.3	1.3	1.3	1.3	1.3	1.3	1.3	1.3	-	1.3	1.3	1.3	1.3	1.3	1.3	1.3
Contribution of Rs (%)	29.9	32.7	34.6	35.5	35.9	36.0	36.0	35.6	36.8	37.3	36.7	37.2	-	45.1	46.7	44.8	43.2	48.2	49.9	52.8
H2 ads./des. Resistance Rads/des ($\Omega.cm^2$)	2.1	1.2	0.8	0.6	1.8	1.9	2.0	2.0	1.6	1.5	1.6	1.6	-	1.4	1.2	1.3	1.4	0.8	0.8	0.5
Contribution of Rads/des (%)	51.0	33.0	23.3	19.2	50.1	53.8	55.0	55.9	46.7	43.7	45.2	46.3	-	48.6	40.3	42.0	45.0	27.2	31.7	21.2
Constant Phase Element ($\Omega^{-1}.s^{\alpha}$)	0.2	0.2	0.2	0.3	0.1	0.1	0.1	0.1	0.1	0.1	0.1	0.1		0.3	0.3	0.4	0.1	0.2	0.3	0.3
α	0.8	0.8	0.8	0.8	0.9	0.9	0.9	0.9	0.9	0.9	0.9	0.9		0.9	0.9	0.8	0.9	0.9	0.9	0.9
Adsorption on Pt Resistance RPtads	0.8	1.3	1.4	1.5	0.5	0.4	0.3	0.3	0.6	0.7	0.6	0.6	-	0.2	0.4	0.4	0.4	0.7	0.5	0.7
Contribution of RPtads (%)	19.1	34.3	42.1	45.3	14.0	10.2	9.1	8.5	16.6	19.0	18.1	16.5	-	6.3	13.0	13.2	11.8	24.6	18.4	26.0
Total Resistance ($\Omega.cm^2$)	4.1	3.7	3.4	3.3	3.6	3.6	3.6	3.6	3.5	3.5	3.5	3.5	-	3.0	2.9	3.0	3.1	2.8	2.6	2.5
Whole Cell																				
Series Resistance Rs ($\Omega.cm^2$)	5.4	5.2	4.9	4.7	5.4	5.4	5.4	5.4	5.4	5.4	5.4	5.4	5.5	4.9	4.6	4.7	5.0	4.4	4.3	4.1
Contribution of Rs (%)	47.5	55.7	57.8	58.7	55.0	55.1	55.7	55.3	57.1	56.8	56.6	57.4	49.1	53.5	54.7	55.5	44.1	49.5	54.7	58.8
Charge Transfer Resistance RCT ($\Omega.cm^2$)	0.2	0.2	0.2	0.2	0.2	0.2	0.2	0.2	0.3	0.2	0.2	0.2	0.2	0.1	0.1	0.2	0.4	0.4	0.4	0.3
Contribution of RCT (%)	1.6	2.0	2.1	2.2	2.0	2.0	2.0	2.1	2.8	2.4	2.2	2.2	1.3	1.3	1.6	1.8	3.6	4.6	4.6	4.6
Double-Layer Capacitance (mF)	17	22	32	36	22	21	22	20	27	24	23	23	13	22	29	24	7.2	9.3	8.2	7.4
Diffusion Resistance Rdiff ($\Omega.cm^2$)	5.8	4.0	3.4	3.1	4.2	4.2	4.1	4.2	3.8	3.9	3.9	3.8	5.6	4.1	3.7	3.6	6.0	4.1	3.2	2.6
Constant Phase Element ($\Omega^{-1}.s^{\alpha}$)	4.7	4.4	4.2	4.0	6.0	6.0	6.0	6.0	6.5	6.5	6.4	6.8	5.8	5.4	4.8	4.2	7.6	5.9	6.3	6.5
α	0.6	0.7	0.7	0.7	0.7	0.7	0.7	0.7	0.7	0.7	0.7	0.7	0.6	0.6	0.7	0.7	0.5	0.6	0.6	0.6
Contribution of Rdiff (%)	51.0	42.2	40.1	39.1	43.0	43.0	42.3	42.6	40.2	40.8	41.2	40.5	49.6	45.2	43.7	42.7	52.2	45.9	40.7	36.7
Total Resistance ($\Omega.cm^2$)	11.4	9.4	8.5	8.0	9.9	9.8	9.6	9.8	9.4	9.5	9.6	9.4	11.2	9.1	8.5	8.4	11.4	9.0	7.8	7.0
τCT (ms)	0.1	0.2	0.2	0.2	0.2	0.2	0.2	0.2	0.3	0.2	0.2	0.2	0.1	0.1	0.2	0.2	0.1	0.2	0.1	0.1
τDiff (s)	1.2	0.6	0.5	0.4	1.0	1.0	1.0	1.0	1.0	1.0	1.0	1.1	1.6	0.8	0.6	0.5	3.2	1.0	0.7	0.5

The mathematical expression describing this circuit is given by Equation 5.4. The charge transfer and diffusion processes have both time constants associated with them which can be calculated from $\tau_{CT} = C_{dl}R_{CT}$ and $\tau_{Diff} = \sqrt[\alpha]{QR_{Diff}}$. Where the parameter α is between 0 and 1 when describing the capacitive behaviour of porous and non-uniform interfaces.

$$Z_{cathode} = R_S + \frac{R_{CT}}{1 + j\omega C_{DL}R_{CT}} + \frac{R_{Diff}}{1 + (j\omega)^{\alpha}QR_{Diff}} \tag{5.4}$$

Using this expression, the values obtained for the resistances are presented in Fig. 5.10 and in Table 5.2. The results show that the series resistance of the cathode (Fig. 5.10 A) is mostly unaffected by the change of vanadium flow rate, except at 200 mL/min where it displays a minor decrease.

The charge transfer resistance (Fig. 5.10 B) decreases progressively with increasing flow rate, with a drop from 0.6 $\Omega\,\mathrm{cm}^{-2}$ at 50 mL/min to 0.5 $\Omega\,\mathrm{cm}^{-2}$ at 200 mL/min. However this decrease is insignificant compared to the diffusion losses. In RFBs the reaction does not occur at a distinct electrode-membrane interface, it takes place throughout the porous electrode. As the design of this RHVFC is based around a flow-by electrode, the electrolyte still has to diffuse through the porous media which would only be slightly affected by the electrolyte flow rate. Hence this explains why the charge transfer losses are only weakly affected by the change of vanadium flow rate.

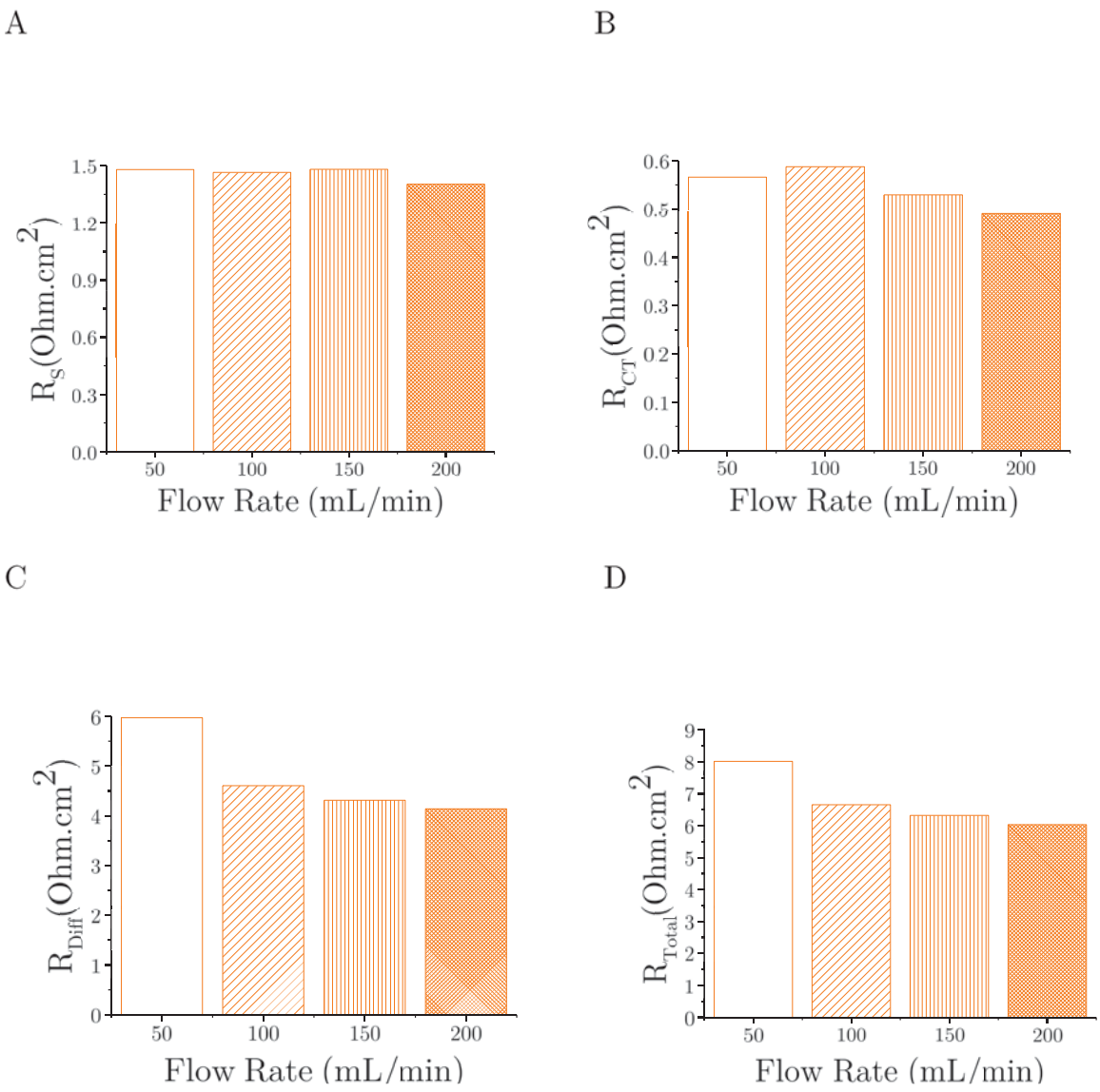

Figure 5.10: A) Series B) Charge transfer C) Diffusion D) Total, resistance of the cathode at different vanadium flow rates, and at 100 mL/min hydrogen flow rate.

As expected, electrolyte flow rate variations mostly affect diffusion losses (Fig. 5.10 C) which drop from 6.0 $\Omega\,cm^{-2}$ at 50 mL/min to 4.6 $\Omega\,cm^{-2}$ at100 mL/min, and there on to 4.3 $\Omega\,cm^{-2}$ and 4.2 $\Omega\,cm^{-2}$, at 150 and 200 mL/min respectively. Thus the catholyte flow rate have a larger effect on the diffusion losses than those associated with charge transfer.

Finally, looking at the total resistance value (Fig. 5.10 D), it is the biggest at the lowest flow rate (50 mL/min) largely dominated by mass transport losses contributing 74 % (6.0 $\Omega\,cm^{-2}$)

of the total losses (8.0 $\Omega\,cm^{-2}$).

Regarding the calculated time constants for these processes, Table 5.2 shows that τ_{CT} is a few milliseconds which is comparable to previous work done by Yufit *et al.* who found similar values from whole cell measurements of the RHVFC.[2] Moreover τ_{Diff} values are about one second which is again consistent with previous work.

The experiments were repeated with the RE on the hydrogen side, and the resulting Nyquist plots of the anode at different vanadium flow rates are displayed in Fig. 5.11 A. As can be observed, the anode spectra were different to those obtained for the cathode. Inductive behaviour was observed at high frequencies followed by a depressed semi-circle, which PEMFC half-cell studies attribute to hydrogen adsorption and desorption on the platinum catalyst;[4] it appears that the charge transfer reaction cannot be resolved, being masked by the hydrogen adsorption/desorption process. From the literature it is understood that molecular hydrogen diffusion in the electrode is too fast to be detected, thus making mass transport limitations negligible.[4] Finally at lower frequencies, an inductive loop is observed (or two in the spectra for 50 mL/min vanadium flow rate). From adsorption effects studies on PEMFC cathodes, it is concluded that that this lower frequency inductive loop arises due to adsorption of crossing vanadium ions onto the platinum catalyst of the hydrogen electrode.[4–6] Indeed during the experiment a bright blue liquid can be observed in the crossover collector suggesting the presence of V(IV) ions. Moreover upon disassembly, it could be seen that the platinum side of the hydrogen electrode was wet with vanadium crossover while the back of the electrode is totally dry. This implies that the crossover is stagnating/flooding the hydrogen electrode, at least temporarily, while it slowly diffuses through the catalyst layer into the carbon/binder media. The presence of PTFE and polyfluorosulphonic acid (PFSA) increase the hydrophobicity of the carbon electrode thus wicking the crossover liquid out of the porous media.

A

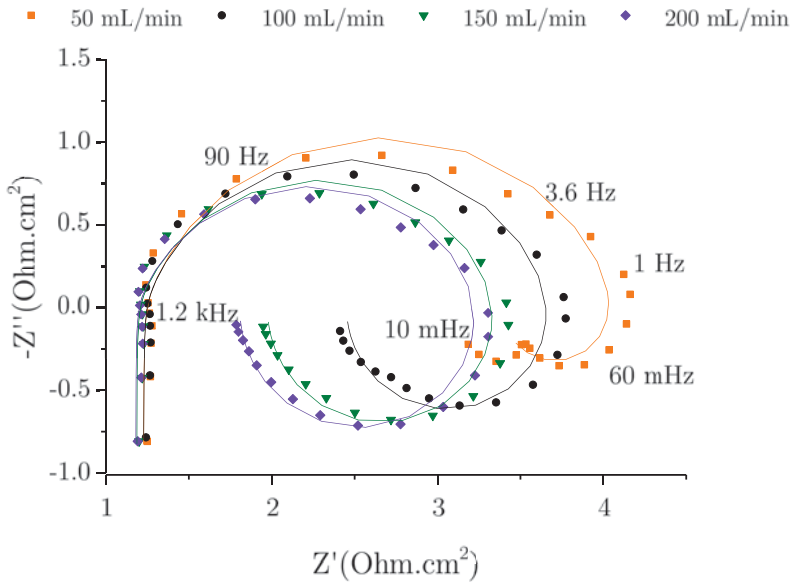

B

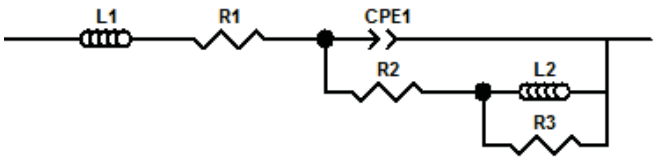

C

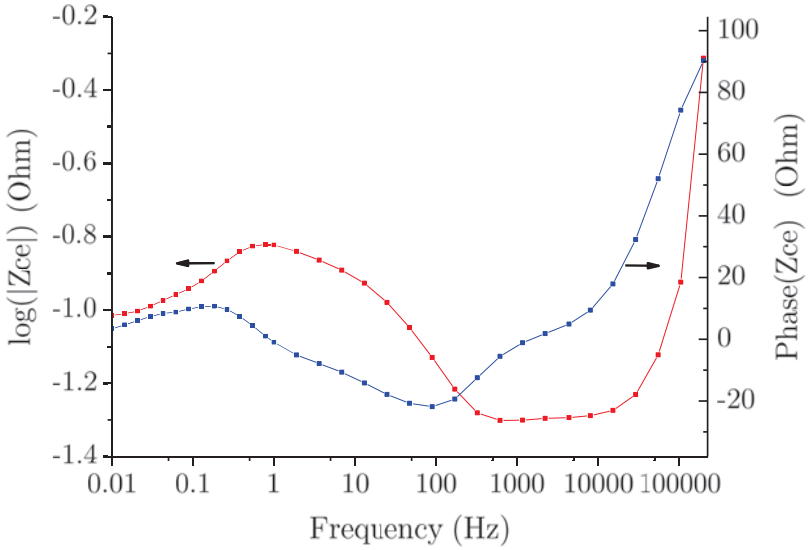

Figure 5.11: A) Nyquist representation of the EIS response at OCV of the hydrogen half-cell with the fitted spectra at different vanadium flow rates with a hydrogen flow rate of 100 mL/min (frequency range: 200 kHz to 10 mHz). B) Equivalent circuit used to fit the EIS data where L1=L_{wires}, R1=R_S, CPE1=CPE, R2=R_{AD}, L2=L_{APt}, R3=R_{APt}. C) Bode plots of the EIS response of the hydrogen half-cell at different vanadium flow rates with a hydrogen flow rate of 100 mL/min.

The equivalent circuit used to model these processes at the anode is given by Fig. 5.11 B. L_{wires} describes the high frequency inductive effects caused by the wires and R_S represents the series resistance of the anode. Next the CPE with R_{AD} in parallel is used to describe the adsorption/desorption of hydrogen on platinum. L_{APt} with R_{APt} in parallel models the low frequency vanadium adsorption behaviour onto the catalyst. The modelling of low frequency inductive behaviour has led to a lot of controversy in the literature. An inductor (expression given by Equ. 2.21 in Chapter 2) has a negligible resistance at low frequencies whereas a capacitor (expression given by Equ. 2.20 in Chapter 2) has a negligible contribution at high frequency. It is argued by some that although an inductive behaviour is observed at lower frequencies it is possible to model this process using a negative differential capacitor and a negative differential resistor, as an adsorption process can usually be modelled by a capacitor and resistor combination.[7] However in this work, an inductor and resistor combination is selected to model the adsorption behaviour. Looking at the Bode plot of the anode presented in Fig. 5.11 C, it is clear that a positive phase shift occurs at lower frequencies which is characteristic of inductive behaviour.[8,9] Moreover from the literature, it has been suggested that if a delay occurs between the time a voltage perturbation is applied and the time for the current to stabilise then this delay will lead to a positive phase shift.[8,9] Thus it is suggested that the coverage, and the change of coverage, of the vanadium adsorbed intermediate is slow.

$$Z_{anode} = jL_{Wires} + R_S + Z* \tag{5.5}$$

$$Z* = \frac{j\omega L_{APt}(R_{AD} + R_{APt}) + R_{AD}R_{APt}}{(j\omega)^{\alpha+1}QL_{APt}(R_{AD} + R_{APt}) + (j\omega)^{\alpha}QR_{AD}R_{APt} + j\omega L_{APt} + R_{APt}} \tag{5.6}$$

The mathematical expression for the equivalent circuit used to model anode behaviour is given by Equ. 5.5 and 5.6. The values of the individual resistances are displayed in Fig. 5.12 and in Table 5.2. Note that the time constants associated with the hydrogen and vanadium adsorption processes cannot be calculated due to their interdependency.

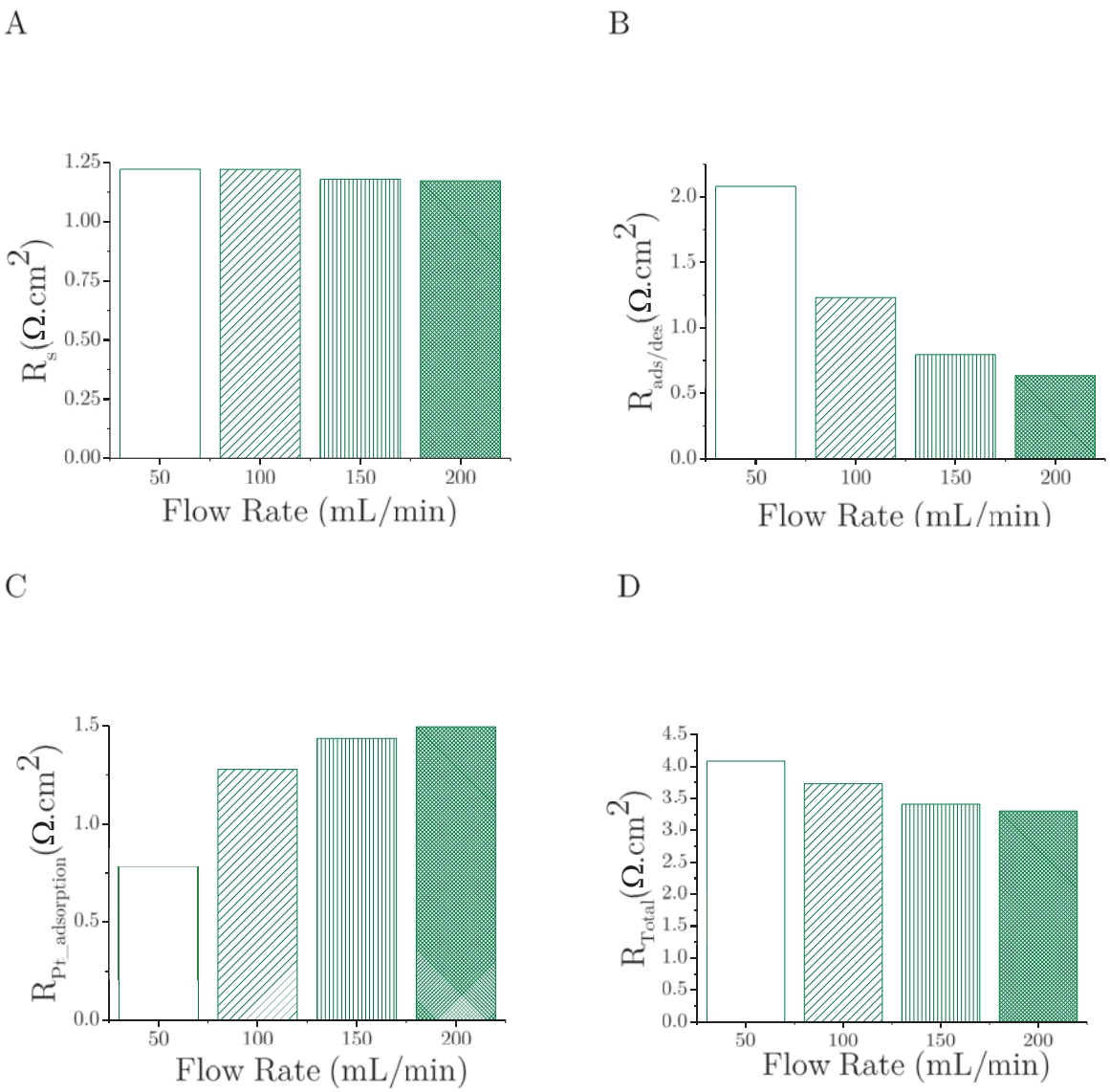

Figure 5.12: A) Series B) Hydrogen adsorption/desorption C) Vanadium adsorption on the platinum D) Total, resistance of the anode at different vanadium flow rates and at 100 mL/min hydrogen flow rate.

From Fig. 5.12 A, it can been that the series resistance of the anode is only very slightly affected by the catholyte flow rate change, with only a 4 % (0.05 $\Omega\,cm^{-2}$) decrease between 50 and 200 mL/min. However the resistance of the hydrogen adsorption/desorption (Fig. 5.12 B) is greatly affected and decreases with increasing flow rate ; it drops from 2.1 $\Omega\,cm^{-2}$ at 50 mL/min to 1.2 $\Omega\,cm^{-2}$ at 100 mL/min and there on to 0.8 $\Omega\,cm^{-2}$ and 0.6 $\Omega\,cm^{-2}$ at 150 and 200 mL/min respectively. Looking at Table 5.2, the contribution of the hydrogen adsorption/desorption

resistance to the total anode resistance is 51 % at 50 mL/min and goes down to 19 % at 200 mL/min. It is observed that the vanadium adsorption resistance shows the opposite trend (which would be expected as they are competing processes), increasing with increasing catholyte flow rate, such that its contribution to the total resistance goes from 19 % to 45 % at 50 and 200 mL/min respectively. The contribution of these two processes are of the same order of magnitude. However looking at Fig. 5.12 D, the total resistance of the anode decreases with increasing vanadium flow rate. Nonetheless, it is important to point out that the 20 % resistance reduction going from 50 (4.1 $\Omega\,\mathrm{cm}^{-2}$) to 200 mL/min (3.3 $\Omega\,\mathrm{cm}^{-2}$) might not benefit the cell in the long run. It can be suggested that at higher catholyte flow rates the amount of vanadium crossover decreases, which explains the increasing vanadium adsorption on platinum resistance. Vanadium ions are surrounded by a hydration shell, implying that more water is also brought over to the anode at lower flow rates perhaps flooding the anode. The long term effects of vanadium adsorption on the catalyst is still unknown, hence it might be best to favour lower vanadium adsorption resistance to lower hydrogen adsorption/desorption loss.

Figure 5.13 A displays the whole cell Nyquist data collected when the RE is placed on either the anode or cathode side. Regardless of which side the RE is placed, or even when no RE is used, the whole cell spectra remain unchanged, as explained in Chapter 4. The EIS plots present two depressed semi-circles indicating the presence of at least two processes. It can be assumed that the whole cell spectra consist of contributions from both the anode and cathode. Looking at the first depressed semi-circle it is concluded that it corresponds to the charge transfer resistance of the hydrogen reaction, whereas the second process corresponds to vanadium diffusion losses. These losses were quantified using the equivalent circuit model presented in Fig. 5.13 B where L represents the inductance response of the cell, R_S the sum of all component resistances, the double-layer capacitance C_{DL} and its parallel resistor R_{CT} emulate the charge transfer resistance of the hydrogen reaction, and finally the constant phase element CPE and its parallel resistor R_{Diff} describe vanadium diffusion. Equ. 5.7 gives the mathematical expression that describes the equivalent circuit used for the whole cell, the individual resistance values and time constants are given by Fig. 5.14 and Table 5.2.

A

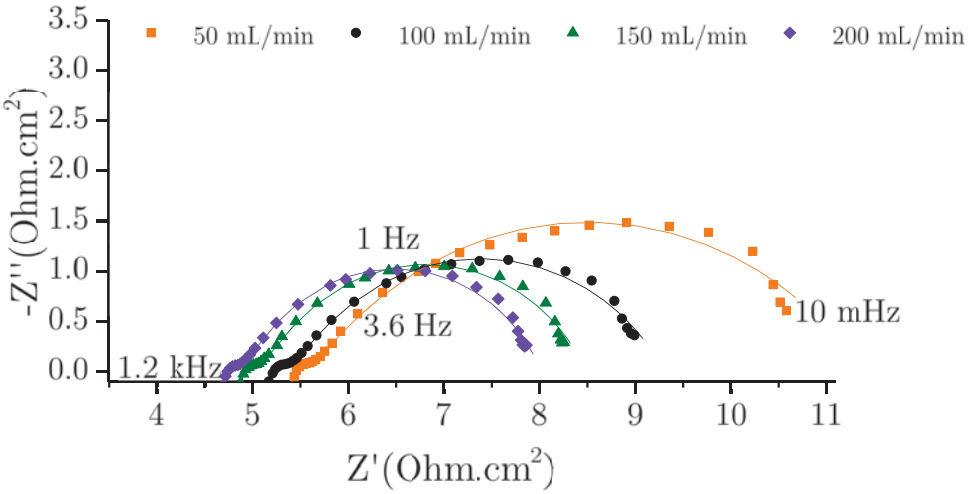

B

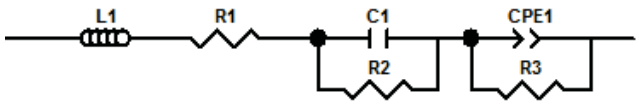

Figure 5.13: A) Nyquist representation of the EIS response at OCV of the whole cell with the fitted spectra at different vanadium flow rates with a hydrogen flow rate of 100 mL/min (frequency range: 200 kHz to 10 mHz). B) Equivalent circuit used to fit the EIS data where L1=L, R1=R_S, C1=C_{DL}, R2=R_{CT}, CPE1=CPE and R3=R_{Diff} .

$$Z_{wholecell} = j\omega L + R_S + \frac{R_{CT}}{1 + j\omega C_{DL} R_{CT}} + \frac{R_{Diff}}{1 + (j\omega)^{\alpha} Q R_{Diff}} \tag{5.7}$$

Figure 5.14 A shows that the series resistance of the system decreases slightly (about 5 % which is $\sim 0.2\ \Omega\,\mathrm{cm}^{-2}$ every time the flow rate drops by another 50 mL/min) with increasing vanadium flow rate.

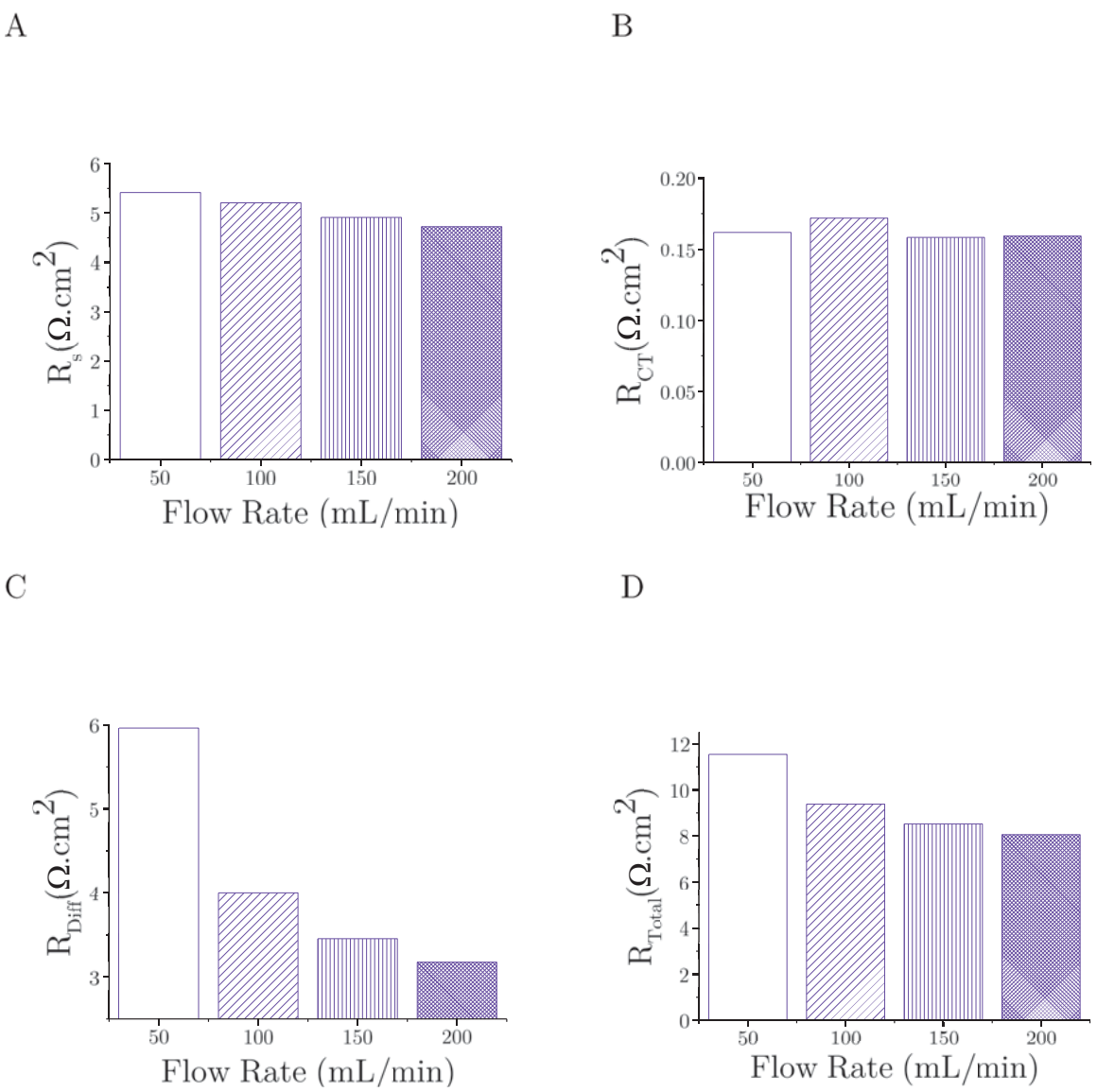

Figure 5.14: A) Series B) Hydrogen charge transfer C) Vanadium diffusion D) Total resistance of the whole cell at different vanadium flow rates and at 100 mL/min hydrogen flow rate.

It is not yet understood why the charge transfer resistance of hydrogen cannot be resolved in the Nyquist plot for the anode, yet contributes significantly to the whole cell spectra, or why the vanadium charge transfer resistance does not appear to contribute. However the time constant values τ_{CT}, which are of the order of tenths of milliseconds, match values found for the hydrogen charge transfer process in PEMFCs[10] confirming further the nature of this process. Figure 5.14 reveals that this hydrogen charge transfer resistance is not affected by catholyte

flow rate. Hence under the conditions tested the biggest contributor to losses in the cell is the vanadium diffusion process (Fig. 5.14 C). As for the cathode, the diffusion related losses drop rapidly with increasing catholyte flow rate. First from 5.8 $\Omega\,cm^{-2}$ at 50 mL/min to 4.0 $\Omega\,cm^{-2}$ at 100 mL/min and there on to 3.4 $\Omega\,cm^{-2}$ and 3.2 $\Omega\,cm^{-2}$ at 150 and 200 mL/min respectively. Regarding the time constant τ_{Diff}, it is in same order as the values found for vanadium diffusion losses in the cathode. Finally it is understood from Fig. 5.14 D that the overall resistance of the whole cell decreases with increasing vanadium flow rate.

Effect of hydrogen flow rates

The RHVFC was investigated under various hydrogen flow rates, and at constant vanadium flow rate (100 mL/min). EIS data collected at OCV (Table 5.2) shows that the cathode and the whole cell do not appear to be affected by varying the anolyte flow rate, or the effects are too small to resolve. Varying this parameter only seems to affect the anode, which presents some small changes as shown in Fig. 5.15.

From Fig. 5.15 A, the hydrogen flow rate has no effect on the series resistance of the anode. However the hydrogen adsorption/desorption resistance shows a small increase going from 1.8 $\Omega\,cm^{-2}$ at 25 mL/min to 2.0 $\Omega\,cm^{-2}$ at 50 mL/min, and thereafter remainimg at 2.0 $\Omega\,cm^{-2}$ at 75 and 100 mL/min. Whereas the vanadium adsorption process displays the opposite trend as it decreases with increasing hydrogen flow rate. Nonetheless, as the hydrogen adsorption/desorption resistance was 4 to 7 times bigger that the vanadium adsorption resistance, this small decrease has no major significance. Overall, looking at the total anode resistance a small gain could be achieved by operating the RHVFC between 50 and 75 mL/min, though the effect of hydrogen flow rate was small compared to the effect of vanadium flow rate.

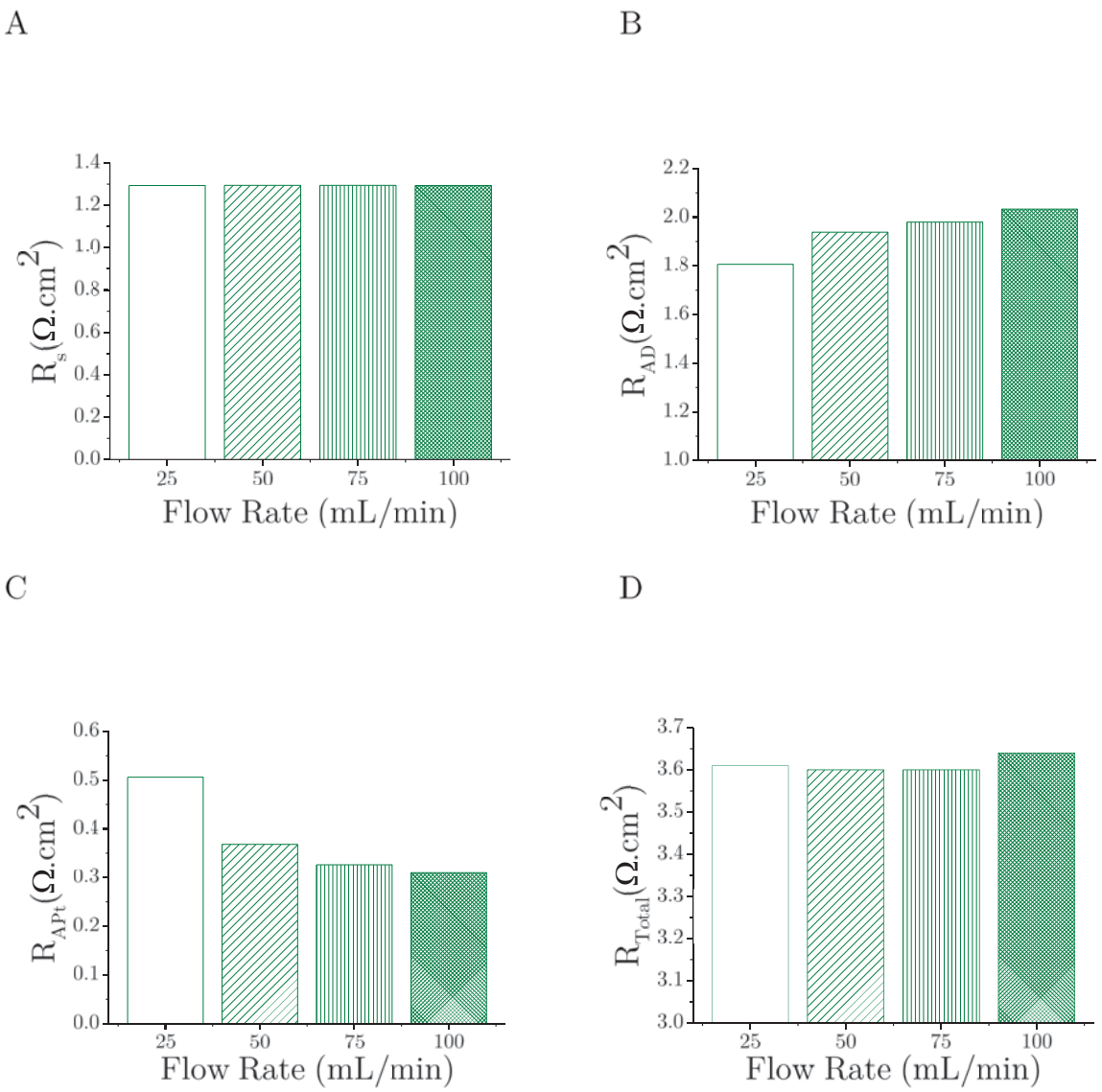

Figure 5.15: A) Series B) Hydrogen adsorption/desorption C) Vanadium adsorption on the platinum D) Total, resistance of the anode at different vanadium flow rates and at 100 mL/min hydrogen flow rate.

Effect of hydrogen and nitrogen mixtures

As depicted in Table 5.2 utilising different hydrogen and nitrogen mixtures (while keeping the anolyte and catholyte flow rate at 100 mL/min) only results in small fluctuations of the resistances for the cathode, anode and whole cell. The only noticeable change is that the hydrogen charge transfer resistance in the whole cell spectra slightly decreases as the concentration of

hydrogen increases, as expected.

Effect of using 0.5 M vanadium/5 M sulphuric acid and 1 M vanadium/3 M sulphuric acid

EIS tests at OCV were carried out at 0.5 M vanadium/5.0 M sulphuric acid concentration at different vanadium flow rates and constant hydrogen flow rate (100 mL/min). The results displayed in Table 5.2 show that the charge transfer resistance of the cathode only fluctuates without showing a clear trend. Nonetheless for a given flow rate the charge transfer resistance value is generally higher than that obtained at 1.0 M vanadium, and its contribution to the total cathode resistance is higher too. As expected, it is clear the vanadium diffusion related losses decrease with increasing flow rate as observed at 1.0 M vanadium concentration. However the diffusion related resistance values were lower by approximatiely 20 % for a given flow rate, except at 100 mL/min where it is only lower by 7 %. Equally, the total cathode resistance was lower by roughly 8 %. The whole cell diffusion losses do not follow that trend where, except for 50 mL/min, they are higher than at 1.0 M vanadium testing. In addition to the vanadium diffusion losses which are observed on the cathode, the whole cell diffusion losses also incorporate diffusion through the membrane, suggesting increased resistance to ion transport across the separator when going from a 1 M vanadium solution to a 0.5 M one. Regarding the anode data, the vanadium adsorption resistance displays lower values with smaller contributions to the total spectra than previously.

When the solution was exchanged for the 1.0 M vanadium/3.0 M sulphuric acid solution, the cathode charge transfer results display similar trends to the 0.5 M vanadium tests. However the diffusion losses are now even lower, with the cathode total resistance found to be the lowest so far. The whole cell results show a smaller series resistance value overall, one possible explanation, as suggested by literature, is the lower acid concentration leads to better membrane hydration.[11] Moreover the hydrogen charge transfer resistance, which was not affected by previous parameter variations, now decreased with increasing flow rates, with values about twice as large as those obtained at 5.0 M sulphuric acid. A hypothesis is that at lower acid concentrations more water is allowed to crossover to the hydrogen electrode, flooding the electrode. The total cell resistance

values are 0.2, 4, 9 and 13 % smaller at 50, 100, 150 and 200 mL/min respectively compared to 5.0 M sulphuric acid tests.

It has also been seen in literature that the vanadium and sulphuric acid concentrations affect the viscosity of the catholyte and thus the permeability of the membrane to vanadium ions. The permeability of the membrane to vanadium ions decreases with increasing vanadium and sulphuric acid concentrations.[11] However as the sulphuric acid concentration becomes larger the effects of the vanadium concentration on the permeability are overshadowed; this is partially due to a bigger influence of the acid concentration on the viscosity of the electrolyte than the vanadium concentration.[11] Decreased viscosity leads to faster transport of ions through the porous media hence the smaller diffusion related losses for the cathode at lower vanadium and sulphuric acid concentrations as seen here. This also explains why the effects on the cell at 1 M vanadium/3 M sulphuric acid are more significant than at 0.5 M vanadium/5 M sulphuric acid. Besides it can be assumed that at lower acid concentrations more water is available thus more vanadium ions could cross over with its hydration shell. However in practice, having more free water molecules means that the membrane is better hydrated, thus there are fewer sites available in the membrane for the vanadium ions to hop to as this is one of the suggested mechanism of vanadium ion diffusion along with free diffusion of dissolved vanadium un-associated with other ion groups.[11] While there is still discussion in the literature on the exact mechanisms of vanadium transport through the ion exchange membrane, there is a consensus that a balance must be found between acid and vanadium concentration in order to avoid membrane dehydration, large diffusion losses due to high viscosity of the electrolyte or excess cross over.[11,12]

5.3 Conclusions

Preliminary results established that whole cell data is insufficient to fully understand the individual cathode and anode losses. Hence the reference electrode set-up presented in Chapter 4 was used to decouple the processes occurring within the cell, and the obtained data fitted using equivalent circuit models to establish the meaning of the different processes.

From the experiments it is concluded that the cathode diffusion and ohmic losses represent

the largest contribution to irreversible losses in the RHVFC. Vanadium crossover to the anode could be detected through vanadium adsorption onto the platinum catalyst. Finally, it has been demonstrated that both the anolyte flow rate and the anolyte composition (*i.e.* hydrogen and nitrogen mixtures) have only minor effects on the cell in comparison with the catholyte flow rate and/or catholyte composition (*i.e.* different vanadium and sulphuric acid concentration) effects. There is potential to minimize these losses by optimizing the catholyte composition, as a balance must be found between acid and vanadium concentration in order to avoid membrane dehydration, large diffusion losses due to high viscosity of the electrolyte, or excess vanadium cross over. This work also suggests that minimising vanadium crossover through improved ion selectivity of the membrane is crucial as the long term effect of vanadium on the hydrogen electrode is not yet understood. Future work can also look into optimising the cathode electrode structure to enhance mass transport to and within the electrode. Improving the cell design for the next RHVFC generation in order to minimise high ohmic losses due to poor current collection is crucial. Such a cell would deliver better performance overall and EIS under load tests would inform about the losses under such conditions.

References

[1] N. Brandon and V. Yufit, *Imperial College London*, 2013, **WO2013104664 A1**, .

[2] V. Yufit, B. Hale, M. Matian, P. Mazur and N. P. Brandon, *Journal of the Electrochemical Society*, 2013, **160**, A856–A861.

[3] V. Viswanathan, A. Crawford, D. Stephenson, S. Kim, W. Wang, B. Li, G. Coffey, E. Thomsen, G. Graff, P. Balducci, M. Kintner-Meyer and V. Sprenkle, *Journal of Power Sources*, 2014, **247**, 1040–1051.

[4] H. Kuhn, B. Andreaus, A. Wokaun and G. Scherer, *Electrochimica Acta*, 2006, **51**, 1622–1628.

[5] I. A. Schneider, H. Kuhn, A. Wokaun and G. G. Scherer, *Journal of The Electrochemical Society*, 2005, **152**, A2092.

[6] V. F. Lvovich, *Impedance Spectroscopy: Applications to Electrochemical and Dielectric Phenomena*, Wiley, 2012.

[7] E. Barsoukov and J. R. Macdonald, *Impedance Spectroscopy Theory, Experment, and Applications*, Second Edi edn., 2005, pp. p 91–93.

[8] P. Piela, R. Fields and P. Zelenay, *Journal of The Electrochemical Society*, 2006, **153**, A1902.

[9] J. T. Müller, P. M. Urban and W. F. Hölderich, *Journal of Power Sources*, 1999, **84**, 157–160.

[10] O. Himanen, T. Hottinen, M. Mikkola and V. Saarinen, *Electrochimica Acta*, 2006, **52**, 206–214.

[11] J. S. Lawton, A. Jones and T. Zawodzinski, *Journal of the Electrochemical Society*, 2013, **160**, A697–A702.

[12] J. Tong and J. L. Anderson, *Biophysical journal*, 1996, **70**, 1505–13.

Chapter 6

A Novel Regenerative Hydrogen-Cerium Fuel Cell

The concept of the Regenerative Hydrogen-Cerium Fuel Cell (RHCFC) was first proposed in this study, combining the high voltage cerium redox couple with the hydrogen generation reaction similarly to the RHVFC.

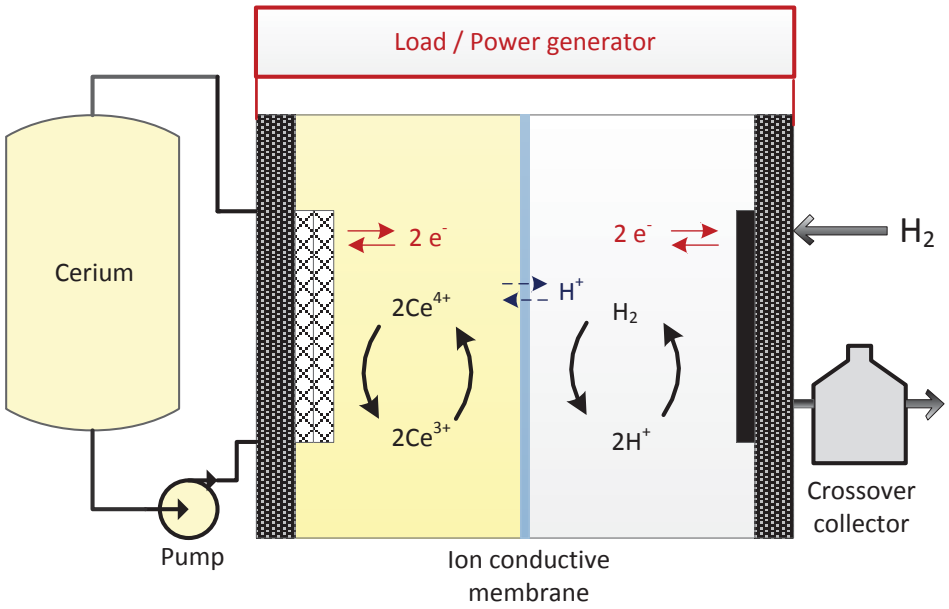

Figure 6.1: Schematic illustration of the RHCFC concept. Reproduced from[1] with the permission of the Royal Society of Chemistry.

As represented in Fig. 6.1, a solution of Ce (III)/Ce (IV) is pumped through the cathode while hydrogen is supplied to the anode. Similarly to the RHVFC in Chapter 5, the hydrogen is not recycled in this work. However in a commercial system, hydrogen pressurised to a few bar would be used in a closed system, with pressure probably being maintained by electrochemical compression, either directly in the flow cell, or by an external device.

As described by Equ. 6.1-6.3, during discharge (energy delivery mode) cerium (IV) is reduced to cerium (III) while hydrogen is oxidised to protons, whereas during charge (energy storage mode), cerium (III) is oxidised to cerium (IV) while hydrogen is produced and stored. Note that the standard cell potential for the cerium couple reaction ($E^0_{cathode}$) can vary between 1.28 and 1.72 V due to changes in activity depending on the solvent used and the solvation of the cerium ions.[2,3] Also note that the H^+ ions concentration changes from 4 M to 3 M when charging the cell.

$$Ce^{4+} + e^- \rightleftharpoons Ce^{3+},\ E^0_{cathode} = 1.28 \text{ to } 1.72 \text{ V} \tag{6.1}$$

$$\frac{1}{2}H_2 \rightleftharpoons H^+ + e^-,\ E^0_{anode} = 0 \text{ V} \tag{6.2}$$

$$Ce^{4+} + \frac{1}{2}H_2 \rightleftharpoons Ce^{3+} + H^+,\ E^0_{cell} = 1.28 \text{ to } 1.72 \text{ V} \tag{6.3}$$

6.1 Experimental methods

This Section will describe the different RHCFC versions used for testing in this chapter.

6.1.1 Generation 1 RHCFC

The Generation 1 (Gen1) RHCFC construction steps are similar to the ones for the Generation 2 RHVFC cell presented in Chapter 3, but with a few differences. The changes are the following:

- The Gen1 RHCFC is a single cell assembly with a 5 cm^2 active surface area as oppose to 25 cm^2. Thus the serpentine flow channels were adapted to the new geometry.

- The cathode material is no longer an untreated carbon paper but two superimposed platinised titanium meshes (METAKEM G, 700 µm individual thickness, 50 mg m^{-2} platinum loading). Due to the high operating voltage of the RHCFC, the use of a carbon based cathode is not suitable as it would degrade rapidly, as discussed in Chapter 2.

6.1.2 Generation 2 RHCFC

The Gen1 RHCFC, utilised graphite based flow channel plates for simplicity, given it was the first proof of concept test. The flow channel plate design was improved for Generation 2 (Gen2), where titanium flow channel plates were designed and built, which are more robust under the operating conditions in the cell. All other components were kept the same.

6.1.3 X-ray photoelectron spectroscopy (XPS) analysis

XPS experimental data collection was done by I. Villar Garcia and the analysis and interpretation of the results were done jointly.

XPS Data Collection

All XPS spectra were recorded using a K-α + XPS spectrometer equipped with a MXR3 Al K monochromated X-ray source (hν= 1486.6 eV). X-ray gun power was set to 72 W (6 mA and 12 kV). With this X-ray settings, the intensity of the Ag $3d_{5/2}$ photoemission peak for an atomically clean Ag sample, recorded at 20 eV pass energy, was 5×10^6 counts s^{-1} and the full width at half maximum was 0.58 eV. Binding energy calibration was made using Au $4f_{7/2}$ (84.01 eV), Ag $3d_{5/2}$ (368.20 eV) and Cu $2p_{3/2}$ (932.55 eV). Charge compensation was achieved using the FG03 flood gun using a combination of low energy electrons and the ion flood source. Survey scans were acquired using 200 eV pass energy, 0.5 eV step size and 500 milliseconds (50 ms $\times$ 10 scans) dwell times. All high resolution spectra were acquired using 20 eV pass energy, 0.1 eV step size and 1 second (50 ms $\times$ 20 scans = 1000 ms) dwell times. Samples were prepared by pressing the sample onto the sample holder with metal clips and analysed at an electron take-off angle normal to the surface with respect to the analyser.

XPS Data Analysis

Thermo Avantage was used for data interpretation. Shirley or two point linear background subtractions were employed depending on background shape. Thermo scientific sensitivity factors were used for quantification analysis.

6.1.4 Secondary Electron Microscopy (SEM)

All SEM and energy dispersive x-ray spectroscopy (EDX) data was collected with the help and supervision of E. Ware. Secondary electrons imaging and an acceleration voltage rage of 5-20 kV were used. All magnification and scale bar values are specified individually for each image.

6.2 Results and Discussion

6.2.1 Proof of concept demonstration

Firstly, in order to prove the feasibility of the RHCFC concept, the Gen1 cell was charged and discharged at different current densities, as presented in Fig. 6.2. As mentioned in Chapter 3, the upper and lower cut-off potential limits were set to be 1.8 V and 1.5 V respectively. These values are calculated using the Nernst equation for this cell assuming a standard cell potential of 1.72 V . Moreover, between the charge and discharge experiments at a given current density (potentiometry experiments), the cell is held at the potential limit (1.8 V after charge and 1.5 V after discharge) until the current drops below 2 $\mathrm{mA\,cm^{-2}}$ such that each charge/discharge experiment is started from the same datum. This chronoamperometry experiment was not carried out after charge/discharge at 5 $\mathrm{mA\,cm^{-2}}$, as the overpotential is so low, the current would drop below the current cut-off limit instantly.

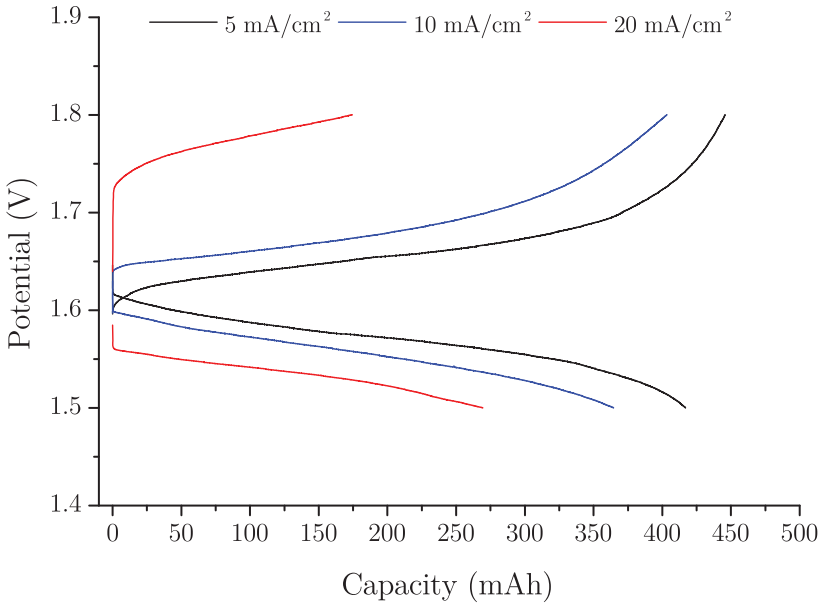

Figure 6.2: Galvanostatic charge/discharge curves of the RHCFC Gen 1 cell with a hydrogen flow rate of 50 ml/min and cerium flow rate of 97 ml/min at different current densities. Reproduced from[1] with the permission of the Royal Society of Chemistry.

The data in Fig. 6.2 reveals asymmetry between the charge and discharge processes. Although the RHCFC can be successfully charged and discharged, the capacity decreases rapidly with increasing current density. The discharge capacity drops from 417 mAh to 365 and 270 mAh on going from 5 to 10 to 20 mA cm^{-2} and from 446 mAh to 404 and 175 mAh on charging. This suggests that when charging, mass transport losses are more significant and the oxygen evolution reaction is also contributing.[4] Furthermore, Fig. 6.2 shows that at 20 mA cm^{-2} there is more capacity at discharge than charge, one possible cause is the parasitic oxygen evolution reaction contributing during the charging step, leading to the cut-off voltage being reached sooner.

Power data was collected at 100 and 50 % SOC as displayed in Fig. 6.3 A and B respectively. Analysis shows a peak power density of 148 mW cm^{-2} at 100 % SOC at a 146 mL/min cerium flow rate. As the cerium flow rate drops to 97 then 48 mL/min, the peak power density drops to 130 and 100 mW cm^{-2} respectively. Similarly at 50 % SOC, as displayed in Fig. 6.3 B, a peak power density of 102 mW cm^{-2} is found at 146 mL/min which subsequently drops to 86 and 67 mW cm^{-2} at 97 and 48 mL/min respectively.

A

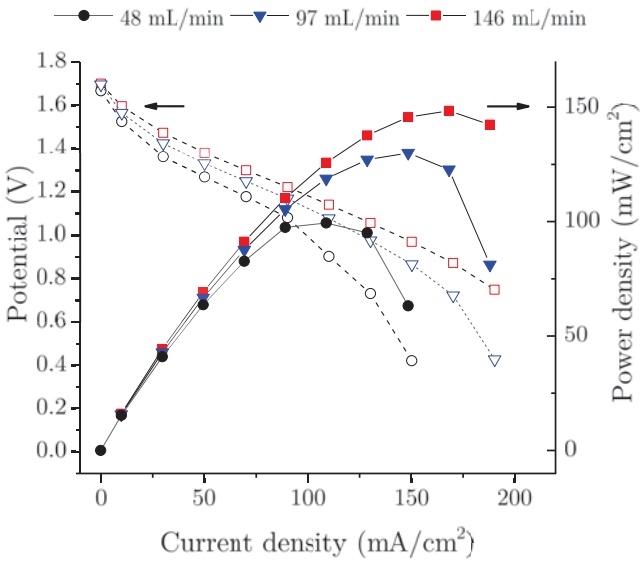

B

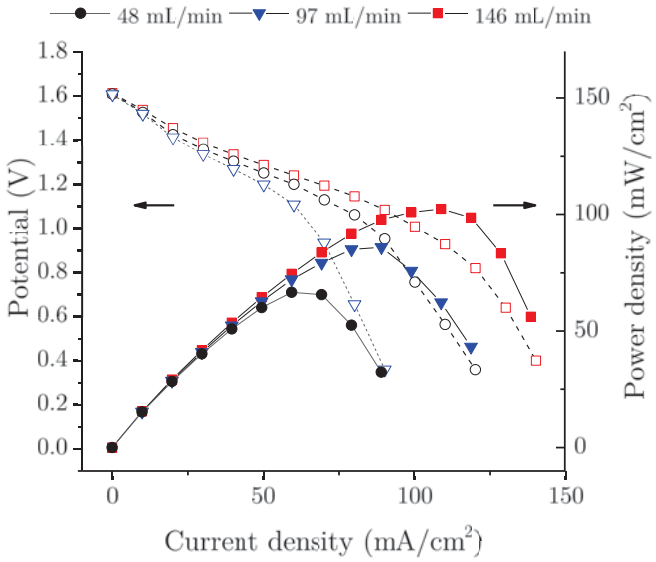

Figure 6.3: Power curve data taken at A) 100 % and B) 50 % SOC, for different cerium flow rates, with a 50 mL/min flow rate for hydrogen. Reproduced from[1] with the permission of the Royal Society of Chemistry.

A

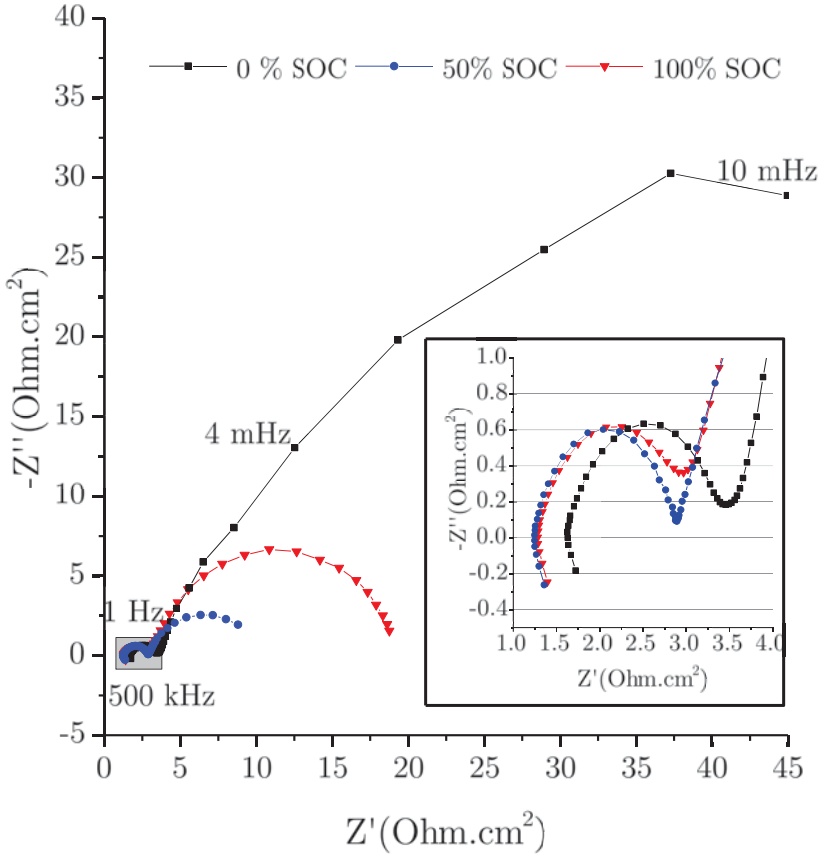

B

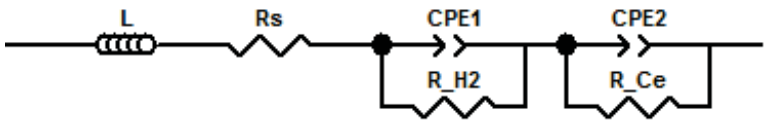

Figure 6.4: A) Nyquist representation of EIS measurements at different SOCs with a hydrogen flow rate of 50 mL/min and cerium flow rate of 146 mL/min B) Equivalent circuit used in order to fit the EIS data where L=L_{Wires}, Rs=R_S, R_H2=R_{H2} and R_Ce=R_{Ce}. Reproduced from[1] with the permission of the Royal Society of Chemistry.

These results demonstrate that the peak power density is clearly affected by the cerium flow rate, indicating mass transport limitations in the cell. Moreover given that the peak power density at

50 % SOC is 102 mW cm^{-2} at 146 mL/min cerium flow rate compared to 100 mW cm^{-2} at 100 % SOC at 48 mL/min flow rate, it can be concluded that a reduction in the catholyte flow rate can have more detrimental effect on the performance of the cell than a decrease in SOC.

EIS measurements are collected at OCV at 0, 50 and 100 % SOC as depicted in Fig. 6.4 A. The Nyquist plot displays two depressed semi-circles at all SOC indicating the presence of at least two processes. Looking at the inset displaying a closer look on the high frequency behaviour, it can be observed that while the high frequency intercept is similar at 50 and 100 % SOC it clearly shows an increase at 0 % SOC. The first depressed semi-circle does not seem to vary strongly between the different SOC, however the second one is clearly the largest at 0 % SOC followed by 100 then 50 % SOC.

Table 6.1: Time constants of the hydrogen and cerium charge transfer processes.

SOC %	CPE1/R_H2 τ (ms)	CPE2/R_Ce τ (s)
0	0.17	11.5
50	0.16	5.9
100	0.12	0.7

$$Z_{wholecell} = j\omega L_{Wires} + R_S + \frac{R_{H2}}{1 + (j\omega)^{\alpha} Q R_{H2}} + \frac{R_{Ce}}{1 + (j\omega)^{\alpha} Q R_{Ce}} \tag{6.4}$$

In order to quantify the different resistance contributions, the equivalent circuit presented in Fig. 6.4 B was used to model the EIS response of the cell. The mathematical model describing this circuit is given by Equ. 6.4. In this circuit, L_{Wires} describes the high frequency inductive effects caused by the wires and the cell, and R_S represents the series resistance of the cell. Next, CPE1 and R_{H2} are attributed to the charge transfer resistance of the hydrogen reaction while CPE2 and R_{Ce} are attributed to the charge transfer resistance of the cerium reaction. This is confirmed by varying the catholyte flow rate and not seeing any variation in the first semi-depressed circle, while the second is affected. Moreover, as given in Table 6.1, the time constant values found for the hydrogen charge transfer reaction are consistent with those obtained in Chapter 5 with the RHVFC cell.

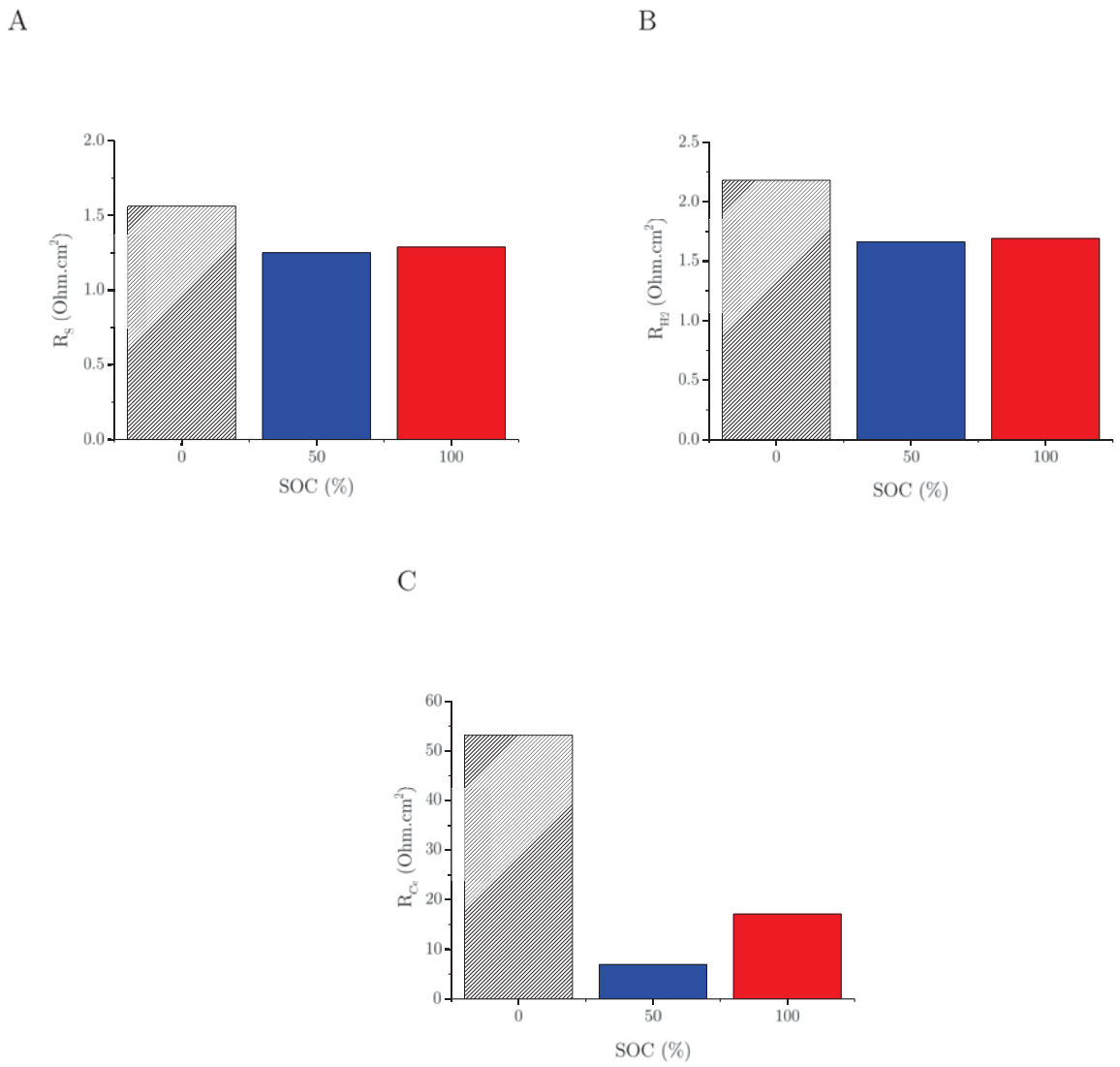

Figure 6.5: A) Series, B) Hydrogen charge transfer, C) Cerium charge transfer, resistance at different SOCs for a hydrogen flow rate of 50 mL/min and a cerium flow rate of 146 mL/min. Reproduced from[1] with the permission of the Royal Society of Chemistry.

The values of the different resistance contributions obtained using this equivalent circuit are presented in Fig. 6.5 A-C. As mentioned above, the series resistance RS is similar at 50 and 100 % SOC (1.3 $\Omega\,cm^2$). The hydrogen charge transfer resistance R_{H2} displays analogous behaviour with similar values at 50 and 100 % SOC (1.7$\Omega\,cm^2$). However at 0 % SOC, both R_S and R_{H2} are higher at 1.6 and 2.2 $\Omega\,cm^2$ respectively. One possible explanation according to the Nernst equation for this cellis: given that the bulk electrolyte proton concentration increase from 3 to 4 M going from 100 to 0 % SOC, the Nafion membrane uptakes MSA thus suffering a decrease in proton mobility; similar behaviour has been observed in a sulphuric acid environment.[2] This

would explain why the proton concentration would affect both the series resistance of the cell and the charge transfer resistance of the hydrogen electrode. Finally, regarding the charge transfer resistance of the cerium reaction R_{Ce}, a minimum is observed in Fig. 6.5 C at 50 % SOC; this is expected as no depletion of one reactant occurs. From 7 $\Omega\,cm^2$ at 50 % SOC, RCe rises to 17 and then to 53 $\Omega\,cm^2$ at 100 and 0 % SOC respectively. There is clearly a large asymmetry between the different SOCs presenting a threefold increase going from fully charged to fully discharged state. This asymmetric behaviour of the cerium redox couple has been demonstrated through cyclic voltammetry experiments.[4] It is also believed that the reduced proton mobility in the membrane at 0 % SOC contributes to the increase of R_{Ce}. It is evident from these preliminary results that the overall resistance of the cell is largely dominated by the charge transfer losses on the cathode as they are a factor of 10-35 times larger than other losses in the RHCFC.

These initial results demonstrate the feasibility of the RHCFC and touch on some of the challenges such as the high dependence of the cell performance on catholyte flow rate and large kinetic losses on the cerium side. However in order to validate these initial findings, decoupled anode and cathode results are necessary, and this will be discussed in the next Section.

6.2.2 Further investigation: half-cell measurements

Firstly the Gen2 RHCFC is cycled at various current densities as shown in Fig. 6.6. The OCV recorded after fully charging and discharging at 5 $mA\,cm^{-2}$ is on average 1.71 V and 1.52 V respectively. However in order to compensate for the higher overpotentials when charging/discharging at higher current densities, the cut-off limits are set to 1.9 V and 1.0 V for the experiments displayed in Fig. 6.6. Unlike the experiments presented for the Gen1 cell (Fig. 6.2), an additional chronoamperometry step is not used between the charge and discharge steps at a given current density; thus efficiencies could be calculated.

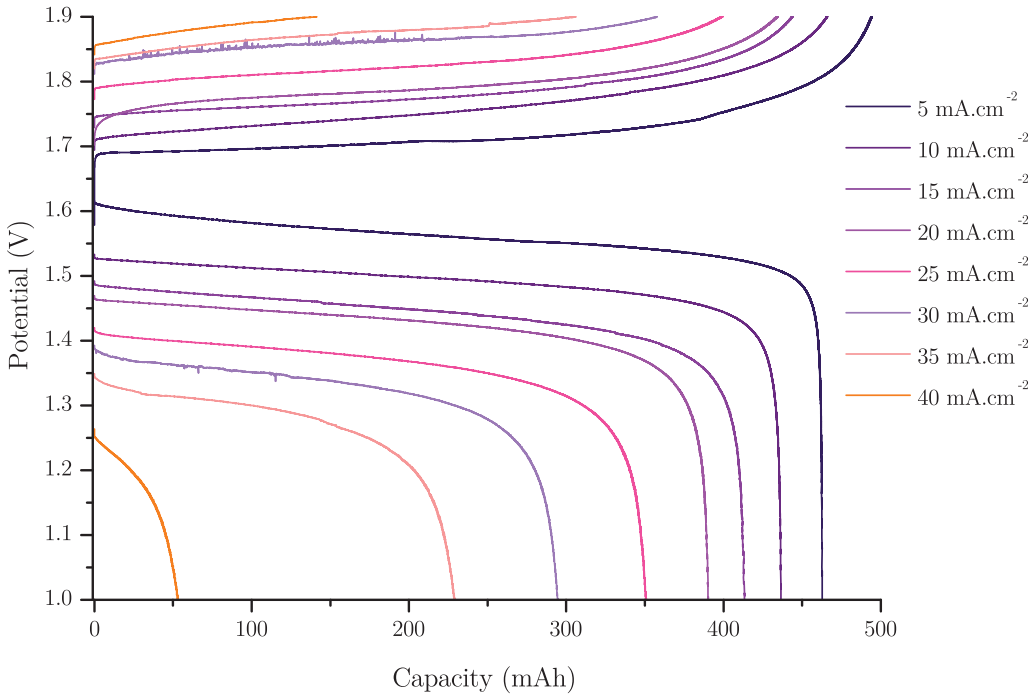

Figure 6.6: Charge and discharge of the Gen 2 RHCFC at various current densities at 150 mL/min cerium flow rate and 50 mL/min hydrogen flow rate. (*Experiment executed by G. Owen-Jones under the supervision of H. Hewa Dewage*)

It is clear from Fig. 6.6 that the Gen2 cell can be successfully charged and discharged at different current densities up to 40 mA cm^{-2}. However looking at the charging step, beyond 25 mA cm^{-2}, the potential curve appears linear when reaching the 1.9 V cut-off voltage, not displaying the mass transport region tail observed for lower current densities. There are two possible causes: first at higher current densities the activation overpotential is higher, secondly it is also believed that the parasitic oxygen evolution reaction taking place during charging is contributing to the potential hence reaching the cut-off sooner. As the cell is not let to charge fully, the matching discharge step also reaches the cut-off voltage rapidly.

Looking at the charge and discharge capacities presented in Fig. 6.7, even at 5 mA cm^{-2} the charge and discharge capacities of 494 and 463 mAh only represent 73 and 69 % of the theoretical maximum capacity of the electrolyte (670 mAh). At 40 mA cm^{-2} these drop to 142 and 53 mAh for the charging and discharging steps respectively which are only 21 and 8 % of the theoretical maximum capacity. The underutilisation of the available electrolyte would represent

a significant barrier to the commercialisation of the RHCFC as it stands.

Looking at the different efficiencies of the Gen2 cell (Fig. 6.8), it is observed that the coulombic efficiency is equal to or above 90 % up to 20 mA cm^{-2} with voltage and energy efficiencies of 79-90 % and 70-85 %. Above 20 mA cm^{-2}, the coulombic efficiency drops rapidly while the voltage efficiency keeps decreasing linearly leading to a decrease of the energy efficiency to values as low as 24 % at 40 mA cm^{-2}.

Power data is collected at 50, 90 and 100 % SOC, the peak power density values as a function of SOC and cerium flow rate are displayed in Table 6.2. Fig. 6.9 presents the power and potential data collected at 50 % SOC at different flow rates. Unlike for the Gen1 cell tests it is now possible to decouple the cathode and anode potentials. From A-C graphs in Fig. 6.9 it is clear that the whole cell losses as the current density increases are mostly driven by the cathode. The anode overpotential increases linearly suggesting mostly ohmic loss, whereas the cathode suffers from severe mass transport losses.

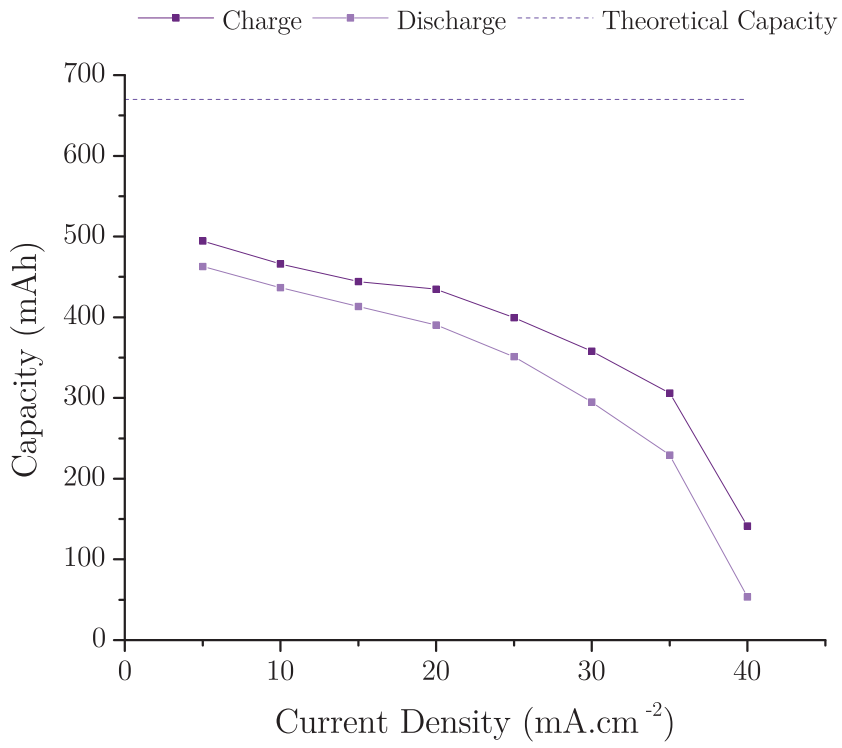

Figure 6.7: Capacity at charge and discharge of the RHCFC at various current densities at 150 mL/min cerium flow rate and 50 mL/min hydrogen flow rate.

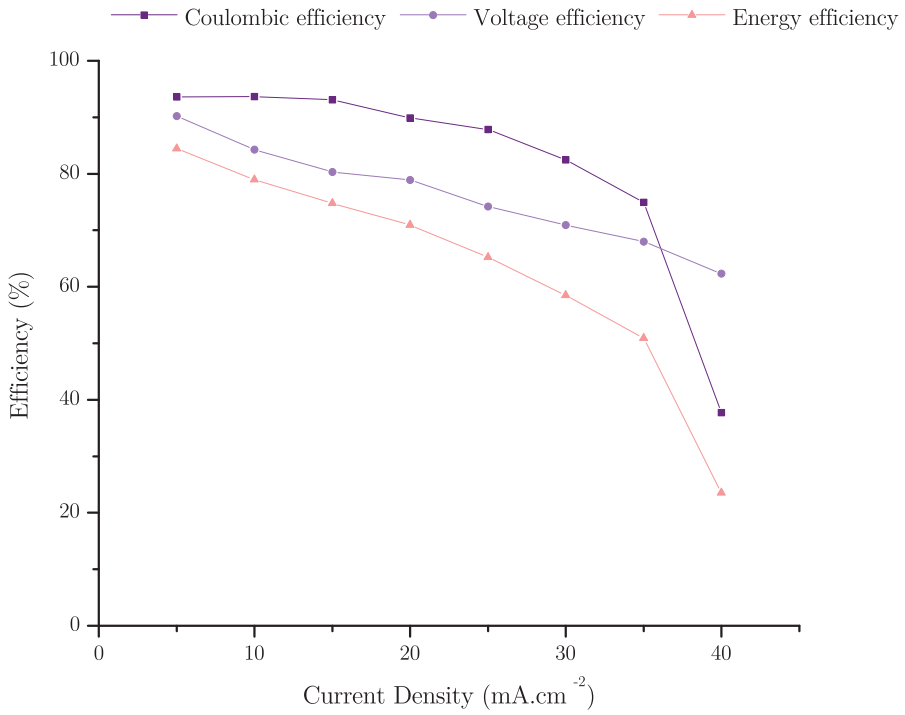

Figure 6.8: Efficiencies at charge and discharge of the RHCFC at various current densities at 150 mL/min cerium flow rate and 50 mL/min hydrogen flow rate.

A

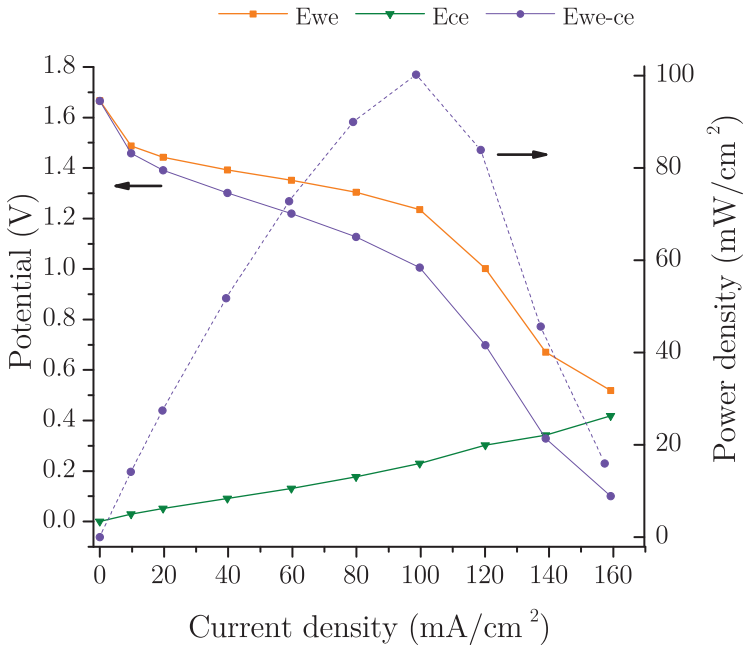

B

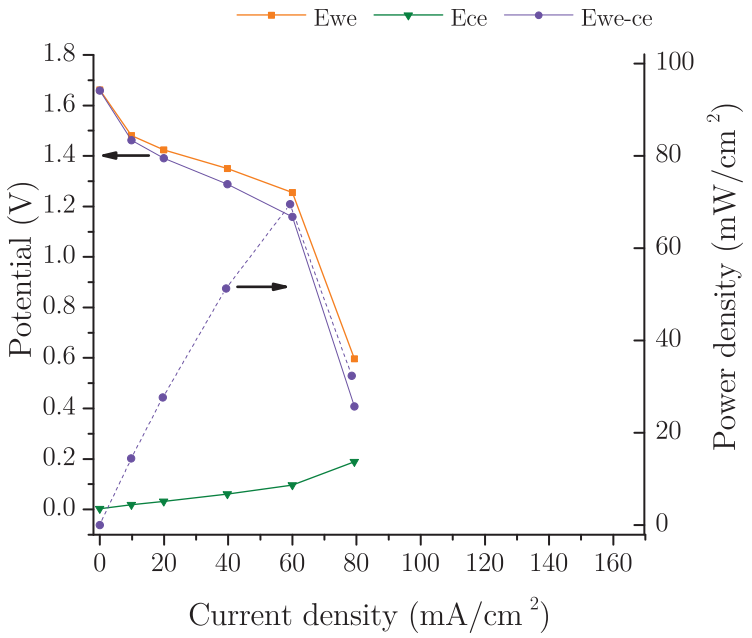

C

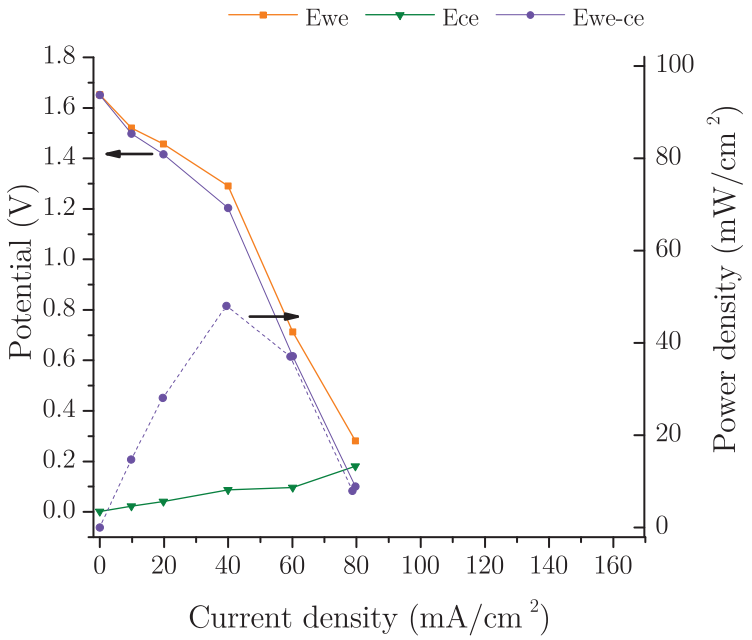

Figure 6.9: Cell potential and power density as a function of current density where Ewe is the cathode potential, Ece the anode potential and Ewe-ce the whole cell potential at 50 % SOC at 50 mL/min hydrogen flow rate and at A) 150 mL/min cerium flow rate B) 50 mL/min cerium flow rate C) 15 mL/min cerium flow rate.

Looking at Table 6.2, the maximum peak power density obtained at 100 % SOC at 150 mL/min cerium flow rate is now 198 mW cm^{-2} which shows an increase of 25 % compared to the Gen1

cell. This gain could be attributed to smaller ohmic losses by the substitution of the graphite plates with the titanium ones in Gen2. However, similarly to the previous cell, the Gen2 cell demonstrates that the power performance is highly affected by the catholyte flow rate. At 100 % SOC, the cell suffers a decrease of 59 % in peak power density going from 150 mL/min (198 $mW\,cm^{-2}$) to 15 mL/min (82 $mW\,cm^{-2}$). As seen previously a decrease in catholyte flow rate has more detrimental effect on the power performance than a decrease in SOC.

Table 6.2: Peak power density values at different cerium flow rates and SOCs and a constant hydrogen flow rate of 50 mL/min.

SOC (%)	Ce flow rate (mL/min)	Peak power ($mW\,cm^{-2}$)
100	15	82
100	50	140
100	100	180
100	150	198
90	15	78
90	50	97
90	150	118
50	15	48
50	50	70
50	150	100

Cyclic voltammetry (CV) was also carried at 50 % SOC following the procedure presented in Chapter 3, the results for the cathode half-cell are presented in Fig. 6.10. The anodic peak corresponds to the oxidation of the Ce(III) to Ce(IV) ions whereas the cathodic peak corresponds to the reduction of the Ce(IV) to Ce(III). As can be seen there is no anodic peak present. However the current does increase with potential. In order to resolve an anodic peak CV was carried out at lower scan rate and the upper voltage limit was expanded from 1.9 to 2.5 V. Nonetheless no anodic peak was resolved.

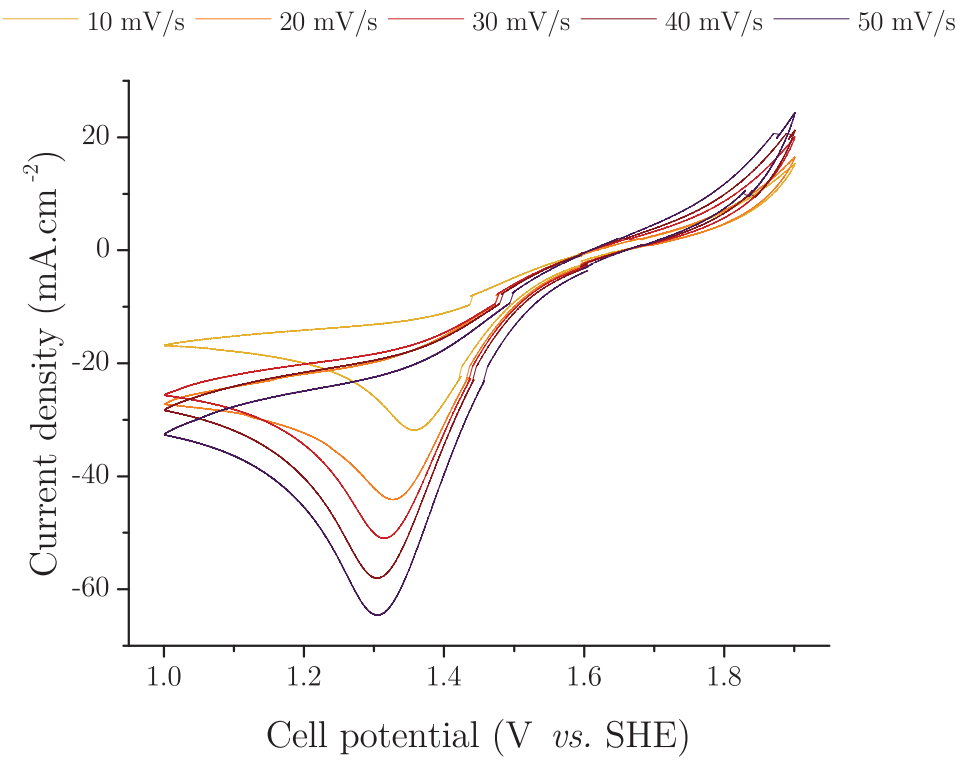

Figure 6.10: Cyclic voltammogram for the cathode half-cell collected at 50 % SOC at different scan rates.

Looking at the cathodic peak, the peak potential slightly shifts to smaller values as the scan rate goes up, varying from 1.36 to 1.30 V on going from 10 to 50 mV/s. Given that no anodic peak is observable it is not possible to look at the peak separation. It is also suggested that the oxidation evolution reaction makes a contribution to the anodic current. Figure 6.11 presents the CV data collected by A. Tsoi in a RHCFC cell utilising either one platinised carbon electrode or four layers of ruthenium coated stainless steel (SS) meshes instead of the platinised titanium meshes used in the present Gen2 cell. Both anodic and cathodic peaks can be observed when the carbon based electrode is used. However, similarly to the present cell, the anodic peak disappears when using the SS meshes. Both SS and titanium meshes are limited in available surface area for the cerium reaction to occur compared to the porous carbon electrode.

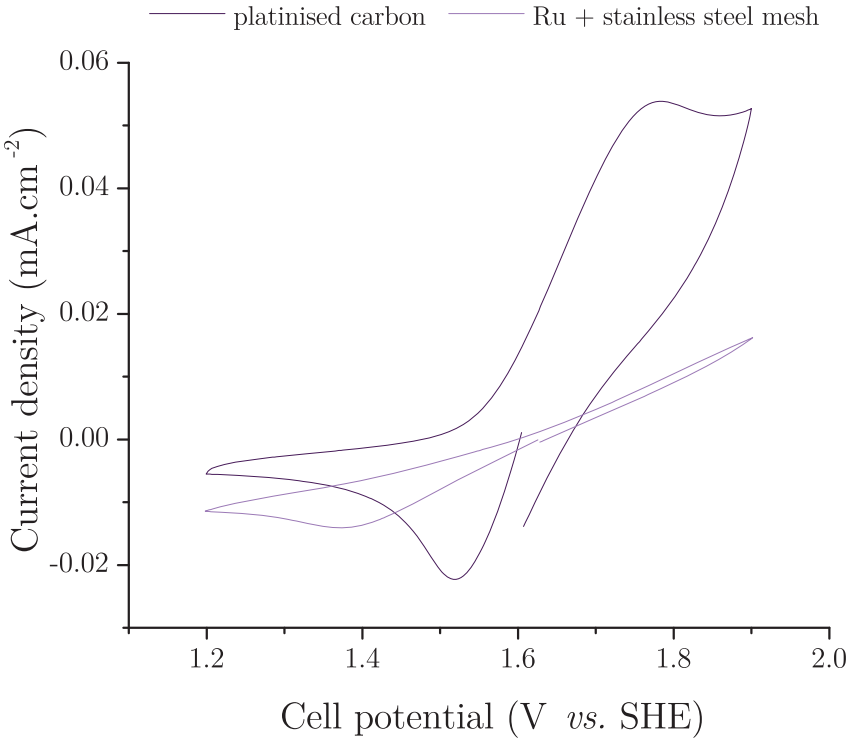

Figure 6.11: Cyclic voltammogram collected for the whole cell where either a platinised carbon electrode or four layers of ruthenium coated stainless steel meshes were used instead of the platinised titanium meshes used in the present Gen2 cell. (*Experiment executed by A. Tsoi*)

The literature reports that the cerium reaction can be considered quasi-reversible.[5] The diffusion coefficient of the Ce(IV) ions was calculated using the Randles-Sevcik equation presented in Equ. 6.5 where ip is the current value at the peak potential, n the number of electrons transferred, F the Faraday constant, A the electrode surface area, C the concentration, v the scan rate, R the gas constant, T the temperature and D the diffusion coefficient.

$$i_p = 0.4463nFAC\left(\frac{nFvD}{RT}\right)^{\frac{1}{2}} \tag{6.5}$$

The values for D was extracted using Fig. 6.12 where the slope of the fitted function is equal to Equ. 6.6. The diffusion coefficient was found to be 4.12×10^{-7} $\mathrm{cm^2\,s^{-1}}$. This value is slightly smaller than the values found in Zhipeng *et al.*s work which range between 2.56–2.68 $\times10^{-6}$ $\mathrm{cm^2\,s^{-1}}$ which were obtained using chronoamperometry and rotating disk electrode experiments. However it is in the same order as the values presented by Nikiforidis *et al.* of 4.63 $\times10^{-7}$ $\mathrm{cm^2\,s^{-1}}$ obtained using cyclic voltammetry which are in agreement with

Leung *et al.* and Devadoss *et al.* (2.7–7.2 $\times 10^{-7}$ $cm^2\,s^{-1}$).[4–7]

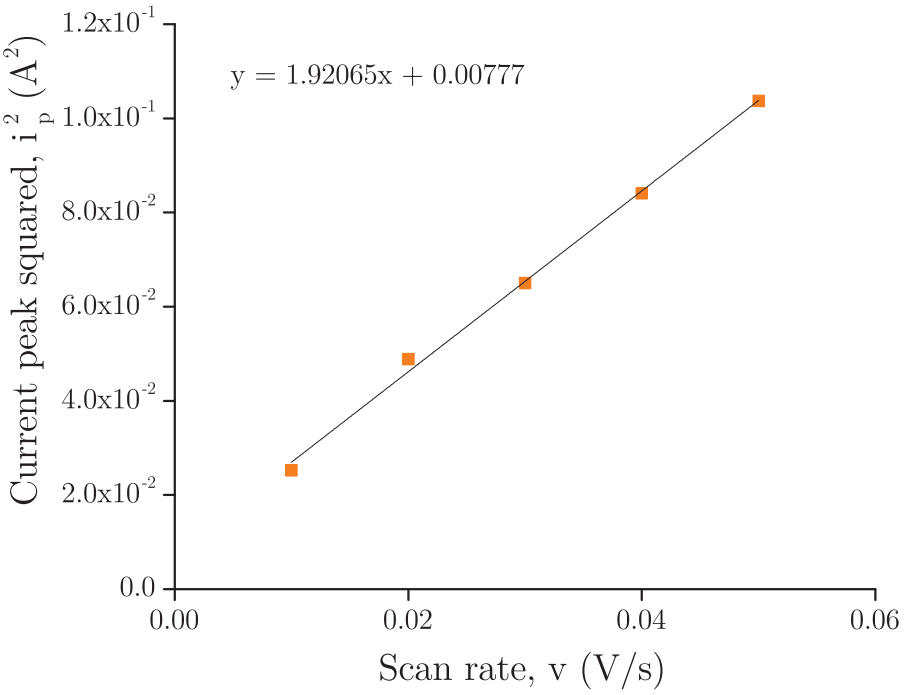

Figure 6.12: Current peak squared as a function of the scan rate where the slope of the fitted function is a function of the Ce(IV) ions diffusion coefficient.

$$slope = \frac{(0.4463nFAC)^2}{RT}D \tag{6.6}$$

It was also found that these diffusion coefficient values decrease with increasing MSA concentration leading to lower peak current values.[4] However a balance must be found for the cerium and MSA concentrations as according to literature higher MSA concentration tend to favour Ce(IV) solubility but would decrease Ce(III) solubility; Leung *et al.* have found that the optimal concentration of cerium is 0.8 M while the MSA concentration is 4 M.[4]

In order to decouple the losses, the DC data needs to be compared with EIS measurements. EIS under load was carried out following the protocol presented in Chapter 3. Figure 6.13 A depicts the cerium half-cell spectra collected at OCV and at different current densities up to 60 mA.cm-2 at 90 % SOC. As the cell is under load, it will discharge over time thus making the system non-linear and consequently not giving meaningful EIS spectra, unless short measurement times are used. In order to reduce the acquisition time for each EIS spectra under load, the frequency

range, which ranges from 200 kHz to 10 mHz at OCV, had to be reduced to 100 kHz to 2 Hz for under load experiments. hence low frequency information was lost but the rest of the data acquired is of good enough quality that it can be fitted with an equivalent circuit model.

Power data is collected at 50, 90 and 100 % SOC, the peak power density values as a function of SOC and cerium flow rate are displayed in Table 6.2. Fig. 6.9 presents the power and potential data collected at 50 % SOC at different flow rates. Unlike for the Gen1 cell tests it is now possible to decouple the cathode and anode potentials. From A-C graphs in Fig. 6.9 it is clear that the whole cell losses as the current density increases are mostly driven by the cathode. The anode overpotential increases linearly suggesting mostly ohmic loss, whereas the cathode suffers from severe mass transport losses.

A

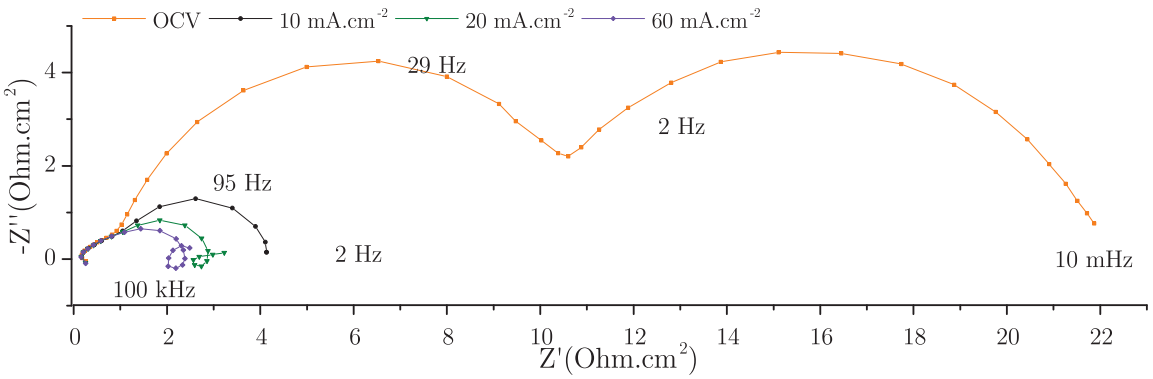

B

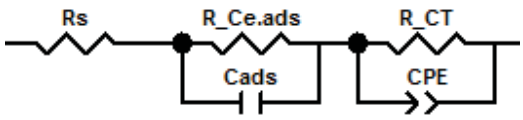

Figure 6.13: A) Nyquist representation of the EIS response of the cerium half-cell at different at different current densities at 50 mL/min cerium and hydrogen flow rates. B) Equivalent circuit used to fit the EIS data from 100 kHz to 2 Hz. (Frequency range at OCV: 200 kHz to 10 mHz, frequency range under load: 100 kHz to 2 Hz).

At OCV, in Fig. 6.13 A, three depressed semi-circles can be distinguished. However when the EIS experiments are carried out under load only the two at higher frequencies can be observed. Thus the equivalent circuit presented in Fig. 6.13 B was used to fit the data between 100 kHz and 2 Hz. The values of the different resistances are displayed in Fig. 6.14. First it can be seen that the series resistance value R_S does not vary with current density. The higher frequency

process observable in Fig. 6.13 A and described by R_{ads} and C_{ads} in Fig. 6.13 B seems to display a slightly larger value at OCV but otherwise remains constant under load. Although the nature of that process is not fully determined, it is understood from the literature that Ce (III) ions can be adsorbed on the platinum surface.[4,8] Thus this highest frequency process could be attributed to this adsorption phenomena with a time constant varying between 11–16 µs. However further work is necessary in order to confirm this. Next, the following process in Fig. 6.13 A described by R_{CT} and CPE is attributed to the charge transfer resistance of the cerium reaction. As observed in Fig. 6.14 this is the largest resistance contribution within the frequency range studied. Moreover, its value is the largest at OCV then decreases with increasing current density, as expected.

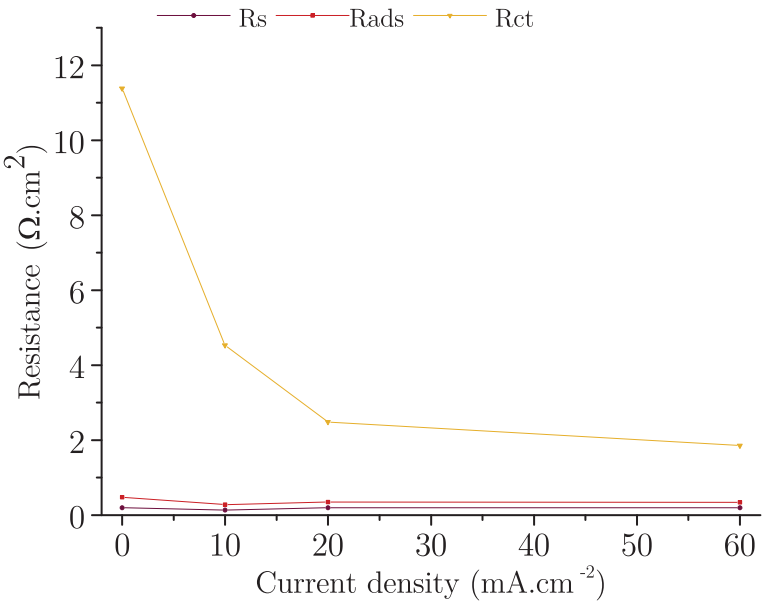

Figure 6.14: Different resistances values obtained for the cerium half-cell at 90 % SOC at 50 mL/min cerium and hydrogen flow rate.

Next, Fig. 6.15 A, depicts the hydrogen half-cell spectra collected at OCV and at different current densities up to 60 mA cm^{-2} at 90 % SOC. At OCV one depressed semi-circle can be observed at higher frequencies while an inductive loop is present at lower frequencies. However, in the EIS under load experiments two processes can be observed at higher frequencies while the inductive loop cannot be included due to the frequency range. Due to the relatively small number of points in the EIS spectra, it was challenging fitting the second process. Thus the

equivalent circuit presented in Fig. 6.15 B was used to fit the series resistance value R_S and the depressed semi-circle present at higher frequencies R_{CT}. The values of the different resistances are displayed in Fig. 6.16.

A

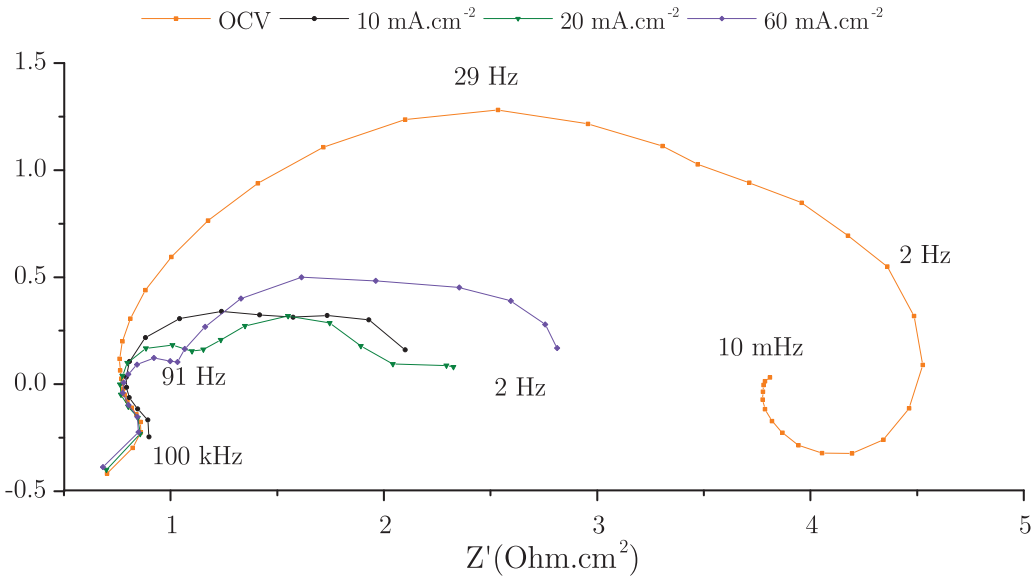

B

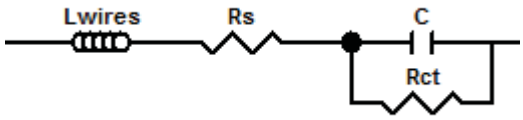

Figure 6.15: A) Nyquist representation of the EIS response of the hydrogen half-cell at different at different current densities at 50 mL/min cerium and hydrogen flow rates. B) Equivalent circuit used to fit the EIS data from 100 kHz to 2 Hz. (Frequency range at OCV: 200 kHz to 10 mHz, frequency range under load: 100 kHz to 2 Hz).

As for the cathode spectra, it can be seen that the series resistance value R_S does not vary with current density. The higher frequency process observable in Fig. 6.15 A and described by R_{CT} and C in Fig. 6.15 is attributed to the charge transfer resistance of the hydrogen reaction. As observed in Fig. 6.16, its value is the largest at OCV then decreases with increasing current density as expected. Its time constant varies between 0.3–1.8 ms which matches values found from PEMFC studies and the RHVFC work presented in Chapter 5.[9]

Finally, Fig. 6.20 A depicts the whole cell spectra collected at OCV and at different current densities up to 60 mA cm^{-2} at 90 % SOC. Similarly to the cathode half-cell, at OCV three

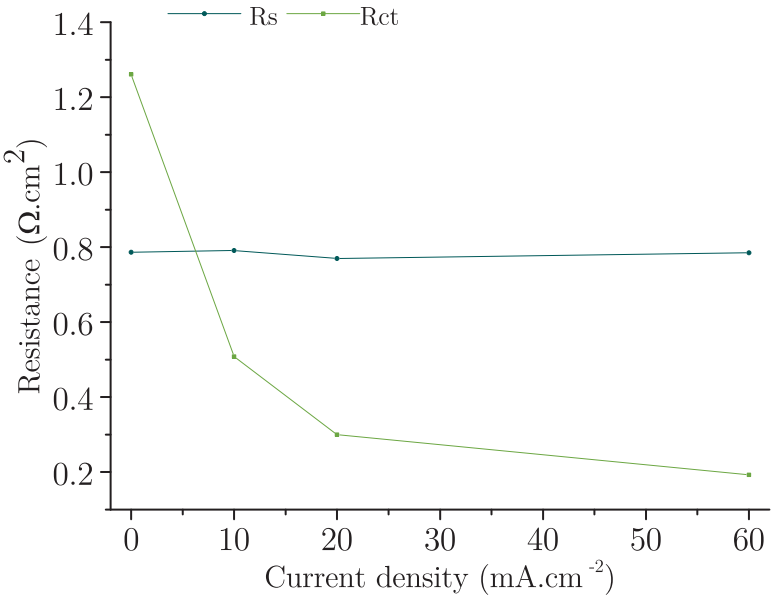

Figure 6.16: Different resistances values obtained for the hydrogen half-cell at 90 % SOC at 50 mL/min cerium and hydrogen flow rate.

depressed semi-circles can be distinguished. However when the EIS experiments are carried out under load only the two arcs at higher frequencies can be observed. Thus the equivalent circuit presented in Fig. 6.17 B was used to fit the data between 100 kHz and 2 Hz. The values of the different resistances are displayed in Fig. 6.18.

As for both half-cells, the series resistance R_S seems invariant with current density. The higher frequency process observable in Fig. 6.13 A and described by R_{HCT} and C_{HCT} in Fig. 6.17 B displays the largest resistance value at OCV, subsequently decreasing with increasing current density. Although the time constant for the process varies between 0.6–4 ms, which suggests it could be related to the hydrogen charge transfer process, the resistance values obtained are 2.5-6 times bigger than the ones found for the hydrogen half-cell. Similarly, the following process in Fig. 6.17 A described by R_{CeCT} and CPE presents the largest resistance value at OCV and then decreases with increasing current density. Again the time constant for the process varies between 1.0–1.6 s suggesting that it is related to the charge transfer process of the cerium reaction. However, once again the resistance values founds for the whole cell are higher than the ones found for the cerium cathode, on average by 1.2 times. It is not fully understood why the values of both hydrogen and charge transfer resistances are larger for the whole cell spectra

A

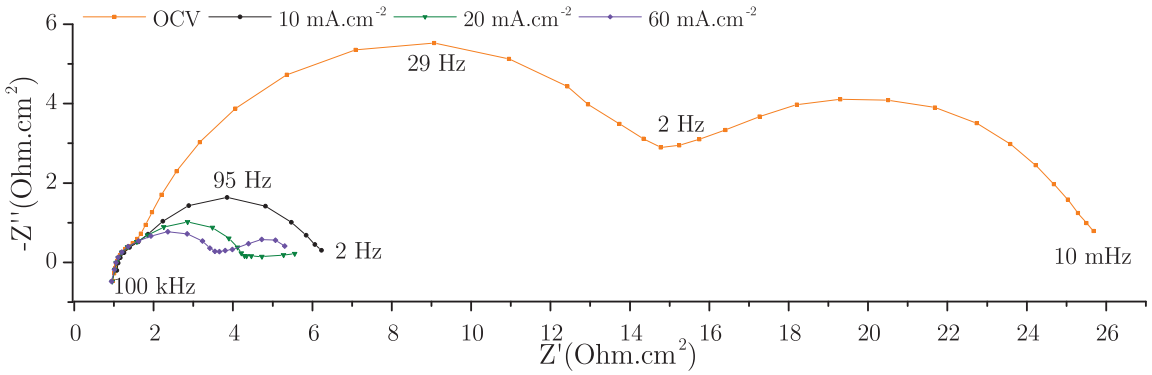

B

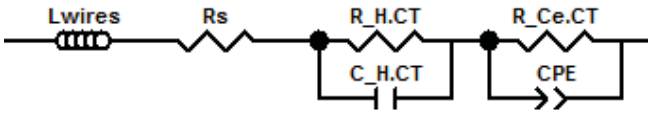

Figure 6.17: A) Nyquist representation of the EIS response of the whole cell at different current densities at 50 mL/min cerium and hydrogen flow rates. B) Equivalent circuit used to fit the EIS data from 100 kHz to 2 Hz. (Frequency range at OCV: 200 kHz to 10 mHz, frequency range under load: 100 kHz to 2 Hz).

than for the half-cell and this requires further investigation.

Having isolated some of the losses using EIS as an investigation tool to look at the half-cells separately, and the whole cell, it is now possible to combine the results found with the DC results discussed earlier. Figure 6.19 presents the cathode potential curve obtained during a polarisation test at 90 % SOC at 50 mL/min cerium and hydrogen flow rates. The associated overpotential for the resistance values extracted from the EIS spectra under load, presented in Fig. 6.13, are also displayed in Fig. 6.19. As can be seen, from the identified losses, the largest contributor to the overall overpotential is the cerium charger transfer resistance. However, there is a large residual overpotential that has not been attributed to a process, which could be attributed to mass transport losses affecting the cathode. Additionally the accuracy of the values found for the ohmic, Ce (III) adsorption and Ce charge transfer resistances can be improved by carrying out EIS under load experiments at more current densities between 0 and 60 mA cm^{-2}. Unfortunately it is harder to increase the current density beyond 60 mA cm^{-2} as mentioned previously. If enough measurements are collected then the resistance values could be meaningfully fitted with a function so that values at higher current densities could be extrapolated, as seen in.[10]

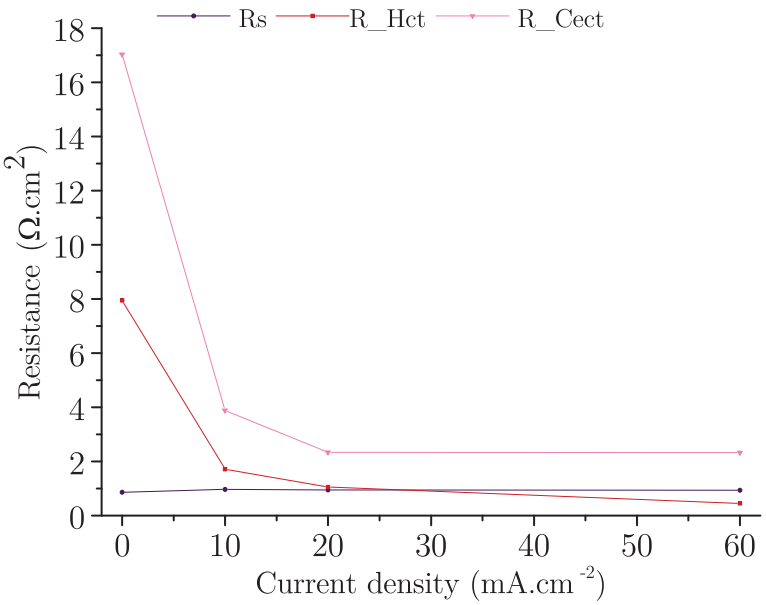

Figure 6.18: Different resistances values obtained for the whole cell at 90 % SOC at 50 mL/min cerium and hydrogen flow rate.

Figure 6.19 presents the whole cell potential curve obtained during the same polarisation test at 90 % SOC at 50 mL/min cerium and hydrogen flow rates. The overpotential associated to the resistance values extracted from the EIS under load spectra presented in Fig. 6.17 A are also displayed in Fig. 6.20.

Once again, from the identified losses, the largest contributor to the overall overpotential is the cerium charger transfer resistance. However, there is an even larger residual overpotential that has not been attributed to a process. It is likely that a portion of that residual loss is related to mass transport losses affecting the cathode as it has been determined to be the limiting process for the RHCFC. Additionally other processes related to losses on the hydrogen side could also be contributing. Besides the accuracy of the values found for the ohmic losses, hydrogen charge transfer and cerium charge transfer resistances can be improved as mentioned above.

As very little information is extracted for the hydrogen half-cell spectra, it was not possible to meaningfully represent the different overpotentials along with the anode potential obtained from the polarisation experiment.

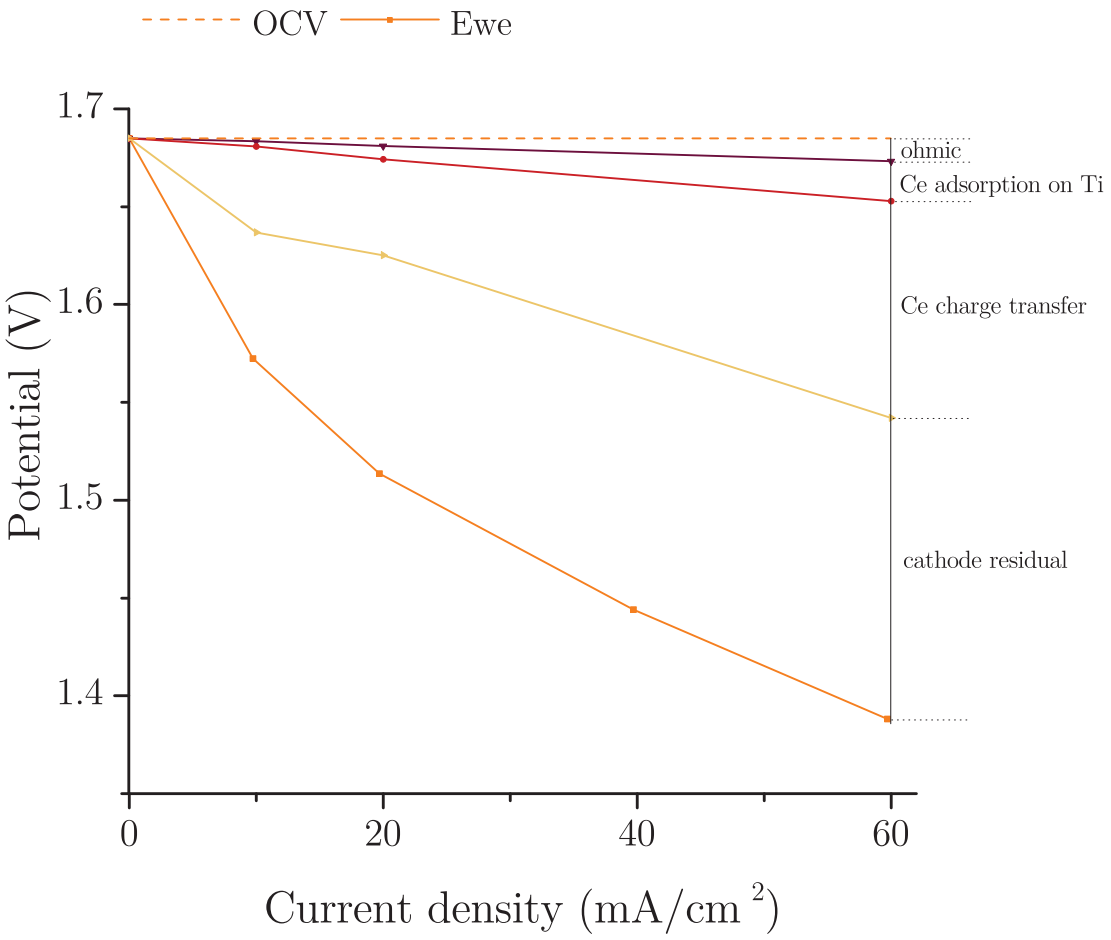

Figure 6.19: Polarisation curve for the cathode taken at 90 % SOC at 50 mL/min cerium and hydrogen with the decoupled losses.

A

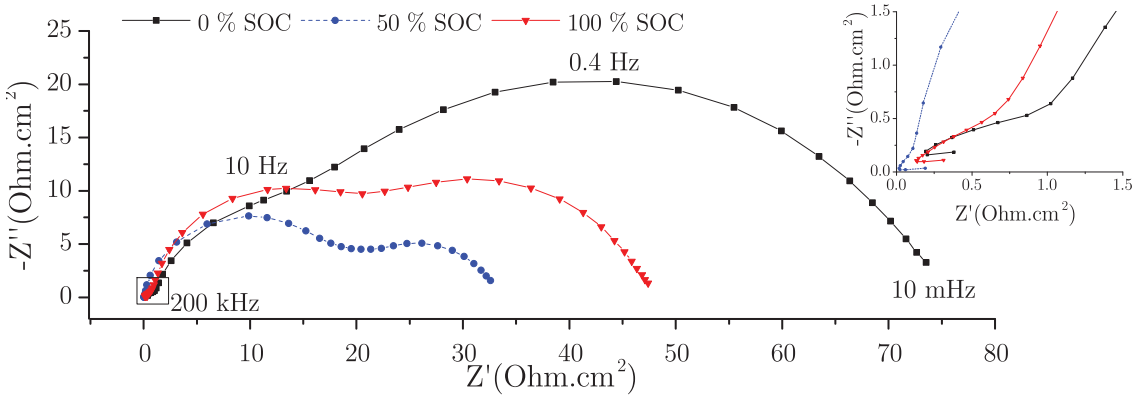

B

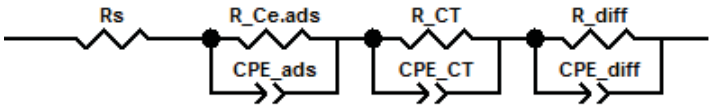

Figure 6.21: A) Nyquist representation of EIS measurements of the cathode at different SOCs with a hydrogen and cerium flow rate of 50 mL/min (frequency range: 200 kHz to 10 mHz) B) Equivalent circuit used in order to fit the EIS data.

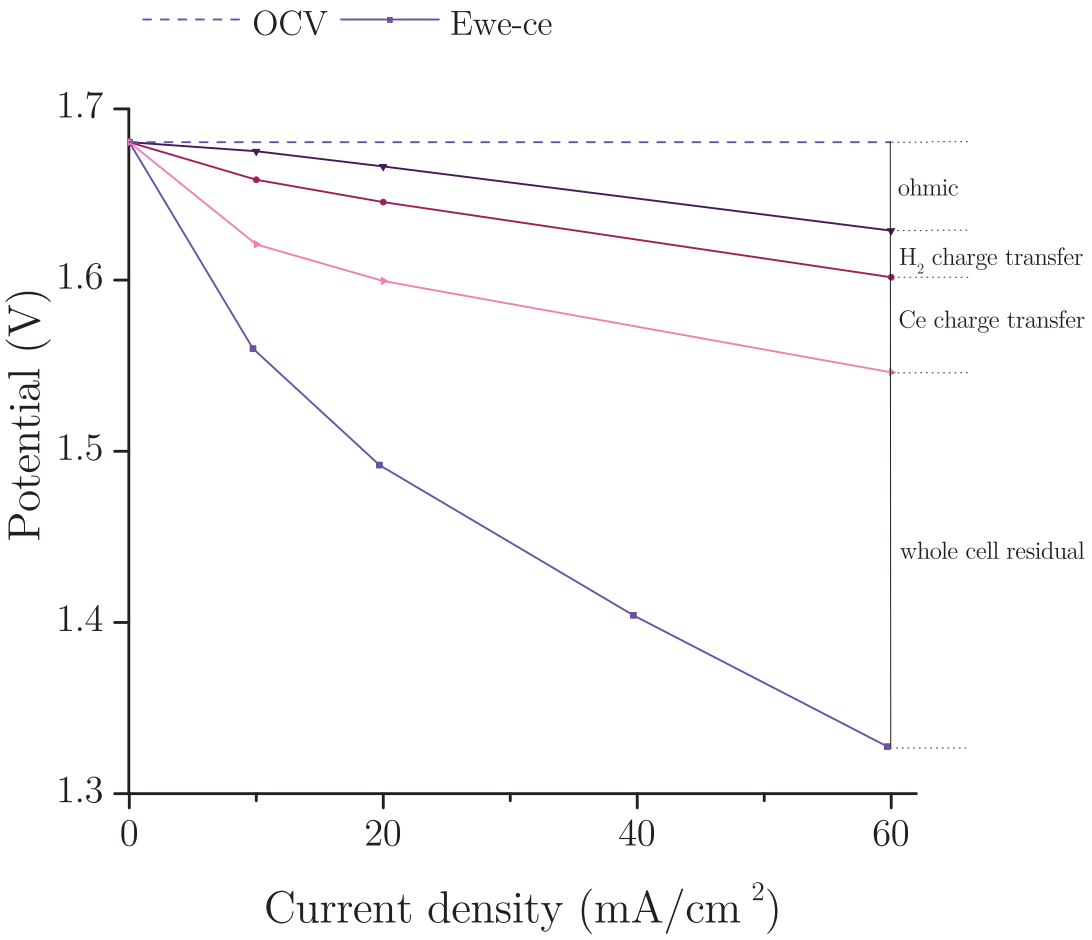

Figure 6.20: Polarisation curve for the whole cell taken at 90 % SOC at 50 mL/min cerium and hydrogen with the decoupled losses.

Like for the Gen1 cell, EIS data at OCV was collected at 0, 50 and 100 % SOC, except that the Gen2 cell allows decoupling of the cathode and anode processes. Figure 6.21 A depicts the cathode half-cell spectra where three depressed semi-circles are observed including the one displayed in the inset graph. As mentioned previously for the EIS under load data presented at 90 % SOC, the processes, going from the higher frequencies to the lower ones, correspond to the Ce (III) adsorption on the platinum, the cerium charge transfer resistance and the mass transport losses. The data was fitted with the equivalent circuit model presented in Fig. 6.21 B and the resistance values are displayed in Fig. 6.22. As it can be observed from both the spectra and the extracted resistance values, the major two contributing processes are the cerium charge transfer and diffusion resistances. High charge transfer losses can be expected for the cerium reaction given that it is only quasi-reversible. In order to improve the reversibility of the

cerium reaction and thus its kinetics, research is on-going on finding new additives, balancing acid concentration in the electrolyte and varying temperature.[4–6] The R_{CT} values found here seem to be the lowest at 0 % SOC (10 $\Omega\,cm^2$) and larger at 50 and 100 % SOC (16 and 17 $\Omega\,cm^2$). However for R_{diff}, a similar trend to the results found for the Gen1 whole cell was observed. Indeed, R_{diff} is the largest at 0 % SOC (64 $\Omega\,cm^2$) then drops to 17 $\Omega\,cm^2$ at 50 % SOC to goes up again at 100 % SOC (31 $\Omega\,cm^2$). This highlights again the asymmetry at the different SOCs that was already demonstrated in this work and in the literature.[1,11]

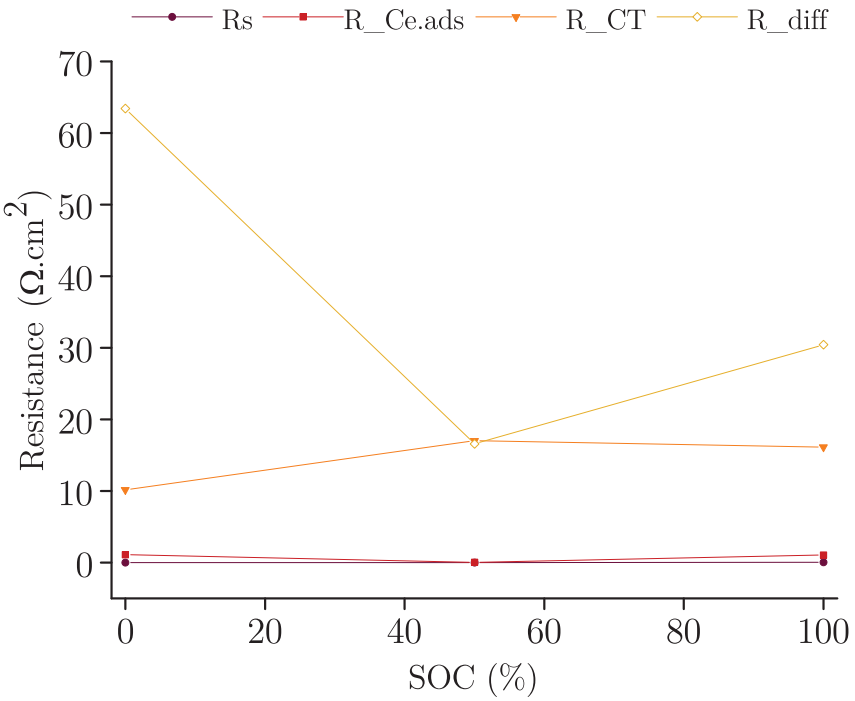

Figure 6.22: Different resistances values obtained for the cerium half-cell at 0, 50 and 100 % SOC at 50 mL/min cerium and hydrogen flow rates.

Figure 6.23 A depicts the anode half-cell spectra where two depressed semi-circles are observed at higher frequencies followed by an inductive loop at lower frequencies. As mentioned for the EIS under load data presented at 90 % SOC, the highest frequency process corresponds to the hydrogen charge transfer resistance. Then, from PEMFC studies and from the work presented for the RHVFC, the second high frequency process is attributed to hydrogen adsorption/desorption on the platinum catalyst.[12,13] It can be noted that, similarly to the hydrogen electrode in the RHVFC, the charge transfer resistance of the hydrogen reaction cannot be well resolved except at 50 % SOC. Finally, based on previous RHVFC data, along with observation of adsorption on

PEMFC cathodes, the lower frequency inductive loop is believed to arise due to the adsorption of crossing cerium species onto the platinum catalyst of the hydrogen electrode.[12–15] The data was fitted with the equivalent circuit model presented in Fig. 6.23 B and the resistance values are displayed in Fig. 6.24.

A

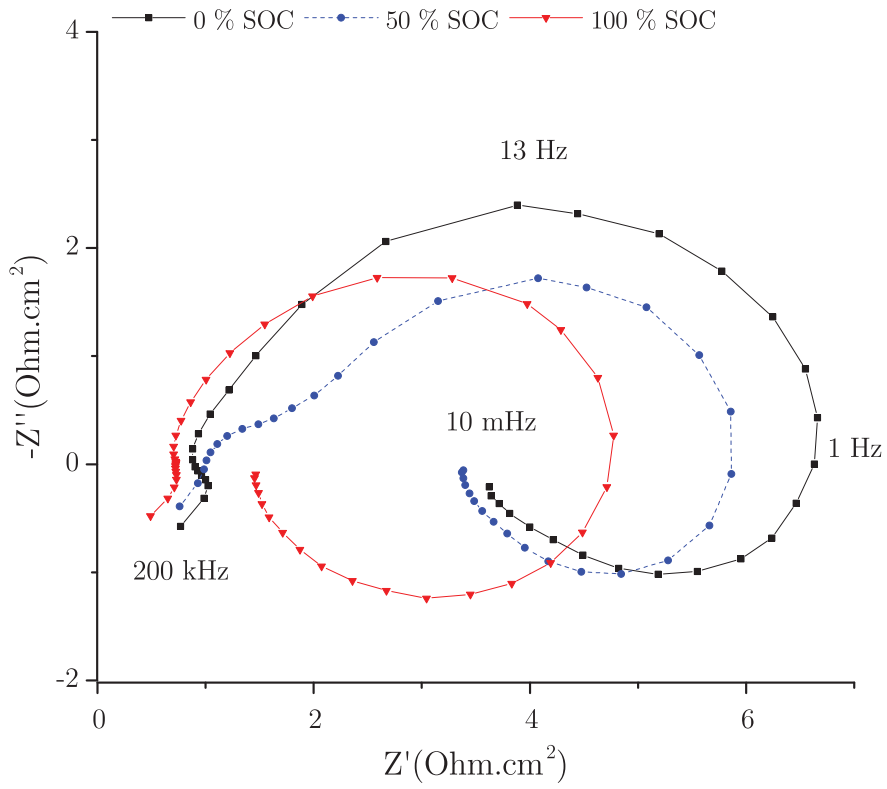

B

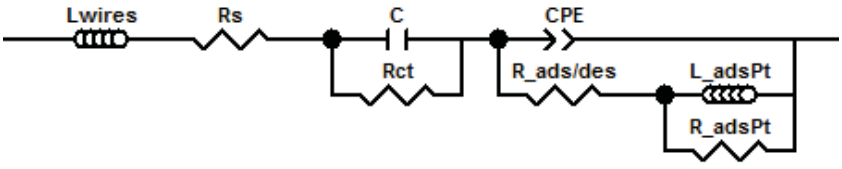

Figure 6.23: A) Nyquist representation of EIS measurements of the anode at different SOCs with a hydrogen and a cerium flow rate of 50 mL/min (frequency range: 200 kHz to 10 mHz) B) Equivalent circuit used to fit the EIS data.

As it can be observed, the ohmic resistance RS appears to be a little higher at 50 % SOC (1.0 $\Omega\,cm^2$) then at 0 % SOC (0.9 $\Omega\,cm^2$), and is the lowest at 100 % SOC (0.7 $\Omega\,cm^2$). Again the charge transfer resistance is highest at 50 % SOC (0.9 $\Omega\,cm^2$) but this time it is of similar value

for both 0 and 100 % SOC (0.8 $\Omega\,cm^2$). It is not well understood why those small variations occur, the MSA concentration varies from 3 M to 4 M going from 0 to 100 % SOC. It would be assumed that as the acid concentration gets bigger the ohmic and charge transfer resistance of the anode would increase as the Nafion uptakes more acid molecules, leading to a decrease of proton mobility as has been seen in sulphuric acid environments.[16] That said, the ohmic and charge transfer resistances are not the main contributors to losses on the anode side.

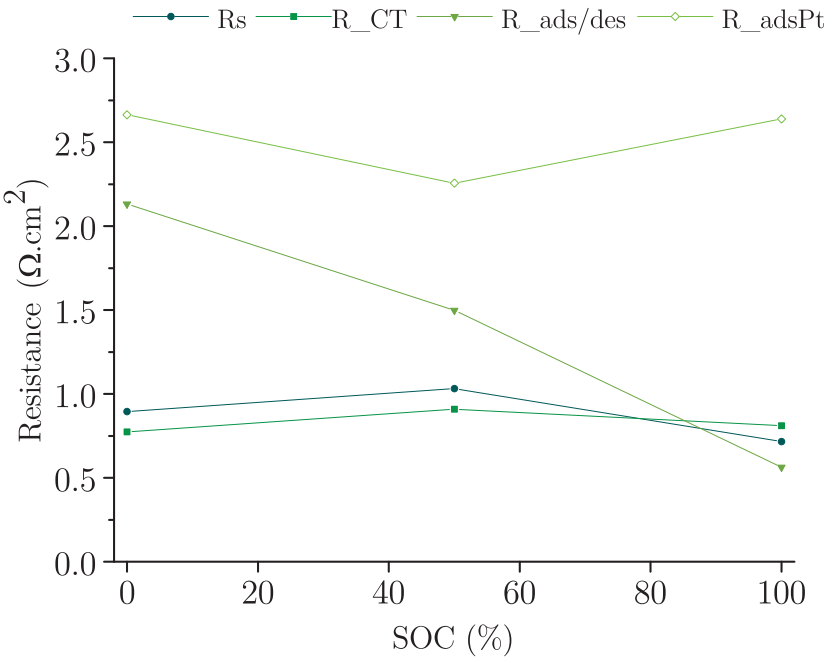

Figure 6.24: Different resistances values obtained for the hydrogen half-cell at 90 % SOC at 50 mL/min cerium and hydrogen flow rates.

The hydrogen adsorption/desorption resistance is the highest at 0 % SOC (2.1 $\Omega\,cm^2$) then drops to 1.5 $\Omega\,cm^2$ at 50 % SOC and then again to 0.6 .cm2 at 100 % SOC. As mentioned above one possible explanation is the change of the acid concentration limiting the transport of protons produced or needed at the hydrogen electrode. Besides at 0 % SOC mostly Ce (III) ions are present in the catholyte, it has been observed during experiments that the crossover collected on the hydrogen side is colourless suggesting that it is exclusively Ce (III) ions crossing over rather than Ce (IV) ones. Given that Ce (III) ions can adsorb onto the platinum on the hydrogen side, the hydrogen adsorption/desorption process might competing with this process. Finally the largest source of resistance of the hydrogen half-cell is cerium adsorption onto the platinum on the hydrogen side. It displays the lowest value at 50 % SOC (2.3 $\Omega\,cm^2$) and values

of 2.7 and 2.6 at 0 and 100 % SOC respectively. This suggest that losses due to the cerium contamination have the most adverse effects at extreme SOCs suggesting that it is best for the hydrogen half-cell if the RHCFC is operated at intermediate SOCs instead.

A

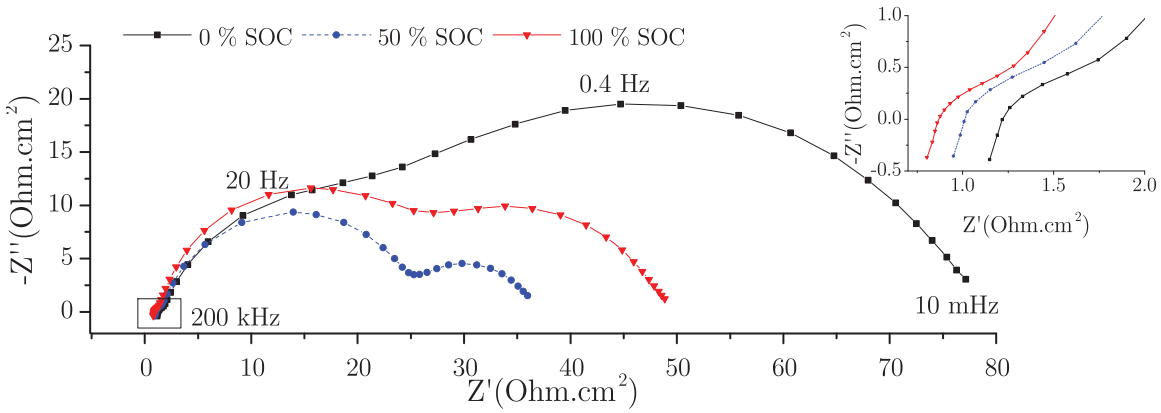

B

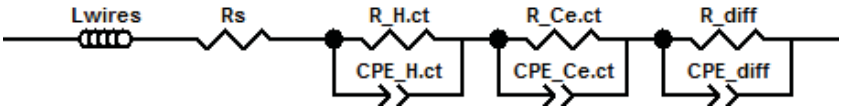

Figure 6.25: A) Nyquist representation of EIS measurements of the whole cell at different SOCs with a hydrogen and cerium flow rate of 50 mL/min (frequency range: 200 kHz to 10 mHz) B) Equivalent circuit used in order to fit the EIS data.

Finally Fig. 6.25 A depicts the whole cell spectra where, similarly to the cathode half-cell, three depressed semi-circles are observed including the one displayed in the inset graph. These processes, going from higher frequencies to lower ones, correspond to the hydrogen charge transfer resistance, the cerium charge transfer resistance and the mass transport losses. The data was fitted with the equivalent circuit model presented in Fig. 6.25 B and the resistance values are displayed in Fig. 6.26.

As can be observed graphically from the spectra and from the resistance values, the major two contributing processes are the cerium charge transfer and diffusion resistances. The values found for the $R_{Ce.CT}$ are 18.7, 23.8 and 23.9 $\Omega\,cm^2$ at 0, 50 and 100 % SOC respectively. Similarly to the EIS data at OCV and under load at 90 % SOC, these cathode charge transfer resistances are on average 1.6 times larger than the values obtained in the cathode half-cell. Finally the R_{diff} values show a similar trend to ones found for the cathode, with highest values at 0 % SOC (58 $\Omega\,cm^2$) then drops to 11 $\Omega\,cm^2$ at 50 % SOC, going up again at 100 % SOC (24 $\Omega\,cm^2$).

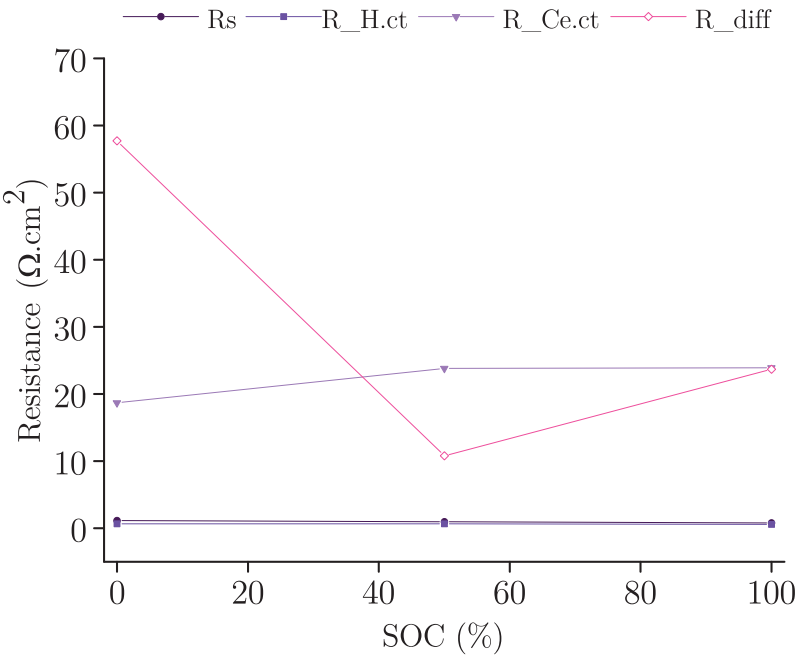

Figure 6.26: Different resistances values obtained for the whole cell at 90 % SOC at 50 mL/min cerium and hydrogen flow rates.

This is in accordance with cathode half-cell and the previous work done with the Gen1 cell.

6.2.3 Surface characterisation and imaging

SEM was used to observe the physical and chemical differences between fresh platinised meshes and used ones. As two platinised meshes were used in the RHCFC, the one facing the Nafion membrane and the one facing the titanium flow channel plates were investigated separately.

A

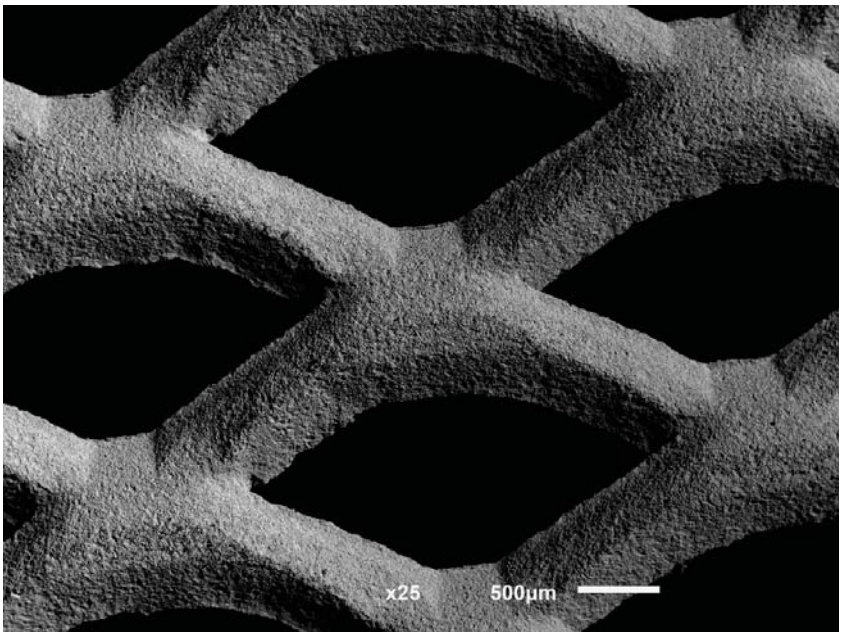

B

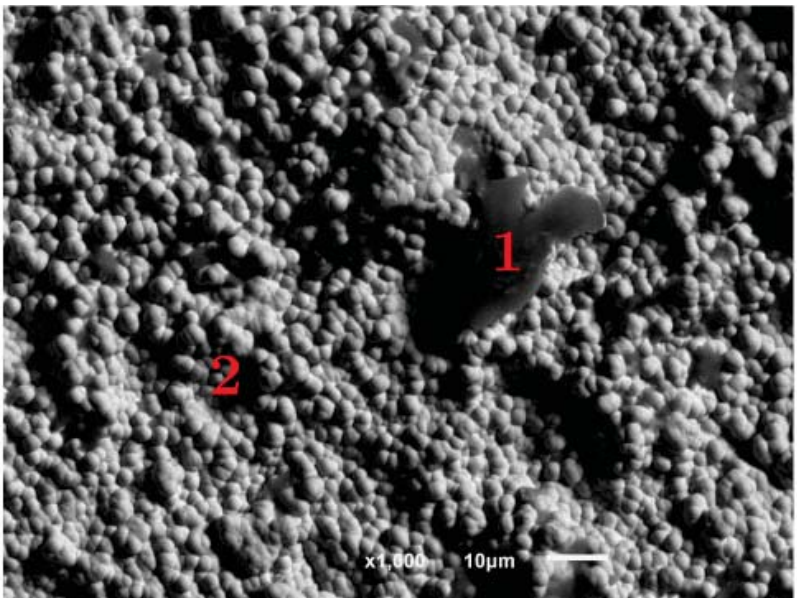

Figure 6.27: A) SEM image of a fresh platinised titanium mesh at × 25 magnification B) SEM image of a fresh platinised titanium mesh at × 1000 magnification where 1 and 2 indicate the points where EDX data was collected.

Figure 6.27 A depicts the fresh platinised mesh with no signs of wear or contamination at × 25 magnification. However from 6.27 B, it can be observed that among the spherical platinum particles are smoother irregular features. Using EDX on the points numbered 1 and 2 on 6.27 B, it was found that region 1 is mostly composed of carbon (76 %) and oxygen (19 %) with traces of other species. Region 2 contains 51 % of carbon and 33 % platinum. It is believed

that these carbon particles are impurities which could have been deposited either during the platinisation of the titanium meshes by the manufacturers, or during handling after purchase. In order to get additional information on the surface composition of the samples, XPS data was collected from the fresh platinised titanium mesh.

A

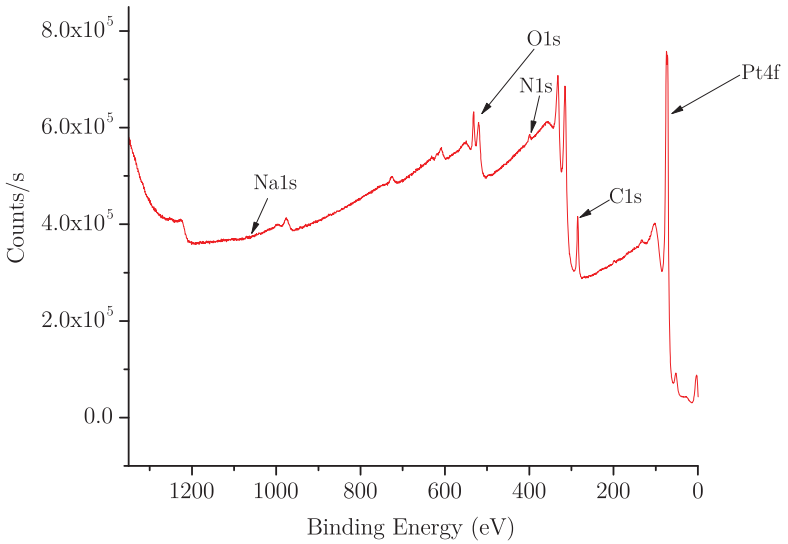

B

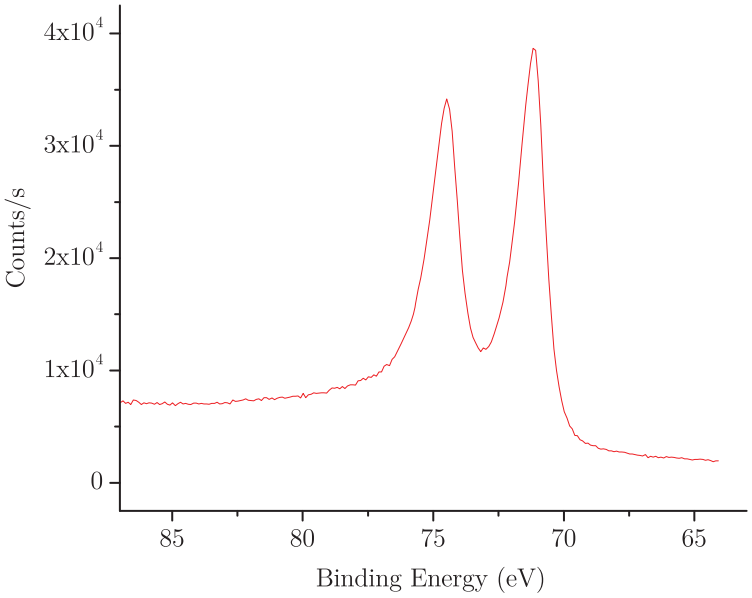

Figure 6.28: A) XPS spectrum of a fresh platinised titanium mesh with its characteristic peaks B) Pt 4f spectrum of a fresh platinised titanium mesh.

Table 6.3: Atomic composition of the area studied using XPS for a fresh, used (facing the membrane) and (used (facing the flow channels) platinised titanium meshes.

Composition	Fresh	Used - facing Nafion	Used facing Ti
	Atomic %	Atomic %	Atomic %
Pt4f	24.0	4.9	7.9
C1s	55.7	55.2	61.2
O1s	13.8	25.0	19.7
N1s	5.5	5.2	5.3
Na1s	1.1	0.8	-
F1s	-	5.1	3.3
S2p	-	3.3	2.4
Ce3d	-	0.6	0.4

As can be seem from Fig. 6.28 A, the surface of the sample shows the presence of platinum, carbon, oxygen, nitrogen and traces of sodium. The atomic percentage of each element is presented in Table 6.3. It can be observed carbon is again the main species present. Also, from Fig. 6.28 B, presenting the Pt 4f spectrum, it is confirmed that there is only platinum metal and no platinum oxides on the sample surface.

Next Fig. 6.29 A depicts the used platinised mesh that was facing the Nafion membrane during testing. Compared to the fresh sample at $\times$ 25 magnification, large regions (couple of 100s micrometers) of a dark deposit is observed on the mesh. Going to $\times$ 1000 magnification (Fig. 6.29 B), the same black phase observed previously can be identified again. It appears that the regions coated by it are now larger. Using EDX on the points numbered 1 and 2 on 6.29 C, it was found that region 1 is mostly composed of carbon (79 %), oxygen (20 %) and traces of sulphur (1 %). Region 2 is mostly composed of platinum (85 %) and carbon (15 %). These darker regions cover sections of the meshes that can be observed by the naked eye. Figure 6.29 D depicts a picture taken from the mesh by an optical microscope where it is easy to mistake those dark regions for wearing of the catalyst when in reality the SEM images demonstrate that the catalyst layer is unchanged but covered by this phase.

A

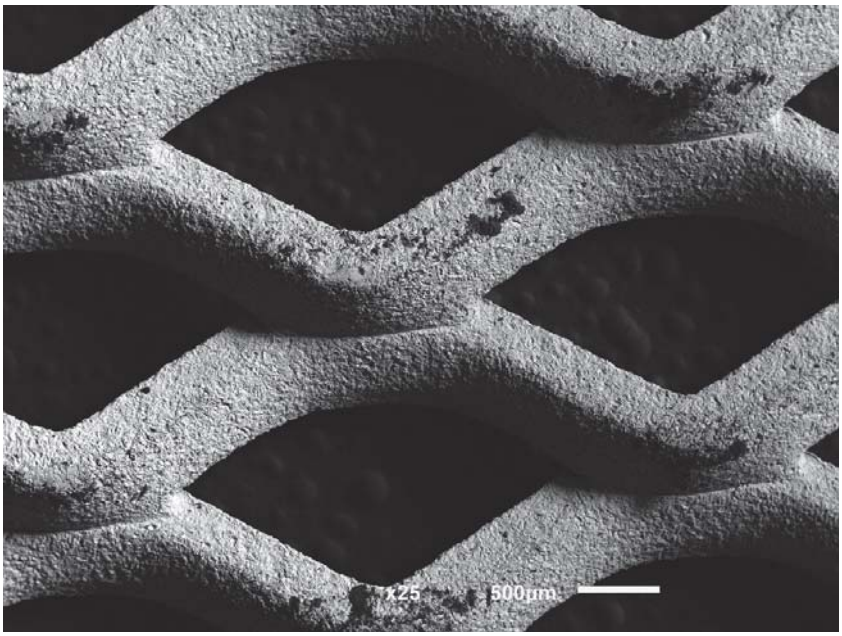

B

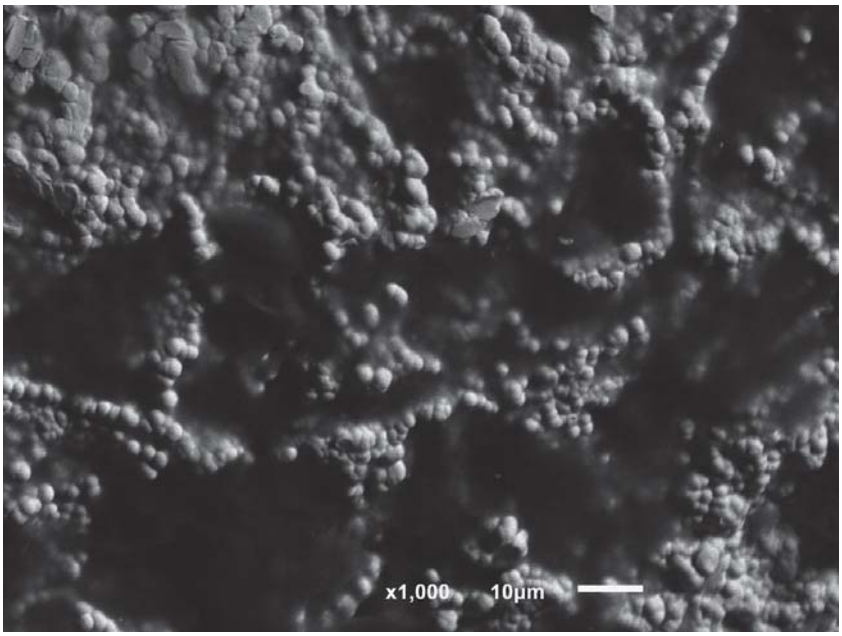

C

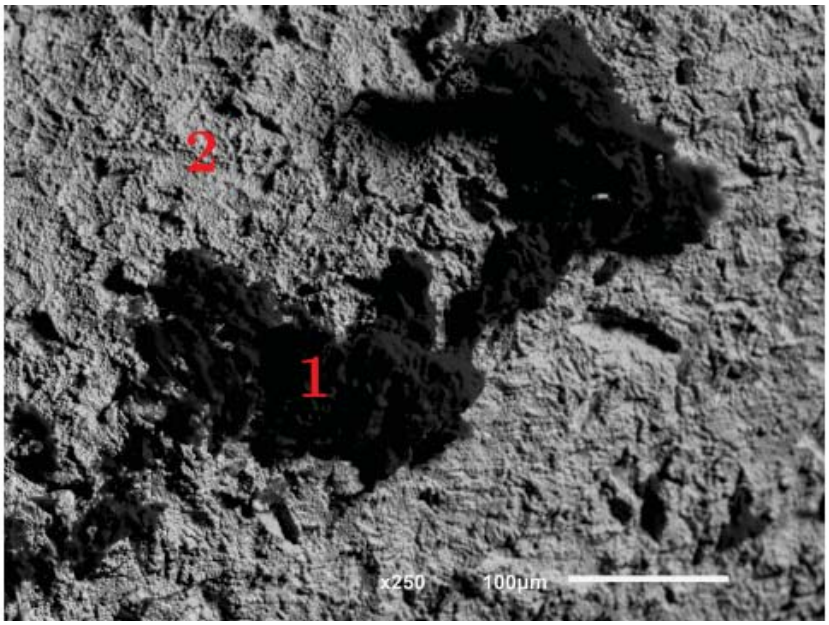

D

Figure 6.29: A) SEM image of a used platinised titanium mesh at × 25 magnification B) SEM image of a fresh platinised titanium mesh at × 1000 magnification depicting the platinum surface coated with a smooth darker phase. C) SEM image of a used platinised titanium mesh at × 1000 magnification where 1 and 2 indicate points where EDX data was collected for D) Optical microscope image of a used platinised titanium mesh where darker regions can be observed on the surface of the coating.

Using XPS analysis, as presented in Fig. 6.30 A, the surface of the sample shows evidence of the same species as previously seen for the fresh sample with some additional ones such as cerium, fluorine and sulphur. The cerium and sulphur species are present in the electrolyte the meshes

are exposed to, whereas the fluorine would have to originate from the Nafion membrane. Again the atomic percentage of each element is presented in Table 6.3. From Fig. 6.30 B, presenting the Pt 4f spectrum, it can be confirmed that the platinum metal has not oxidised after use. Moreover from 6.30 B presenting the C 1s spectrum, it can also be concluded that no carbon based oxides are present either.

A

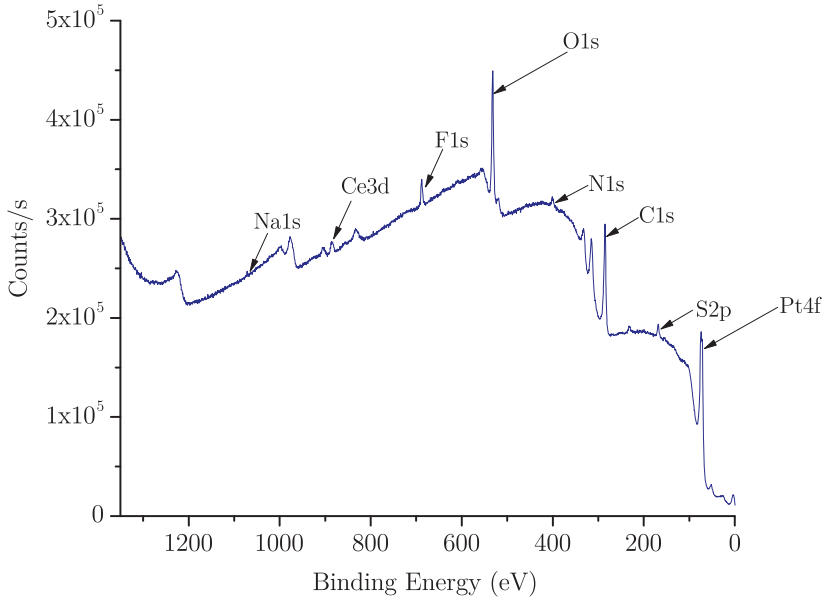

B

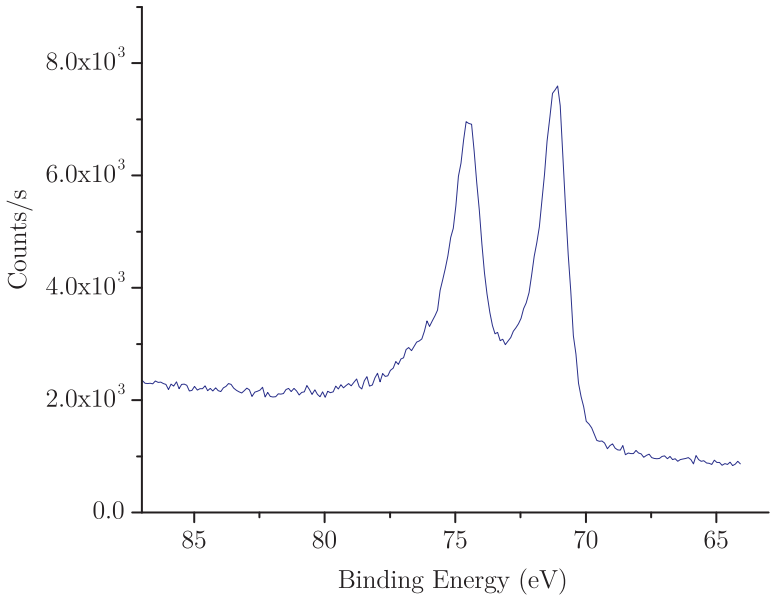

C

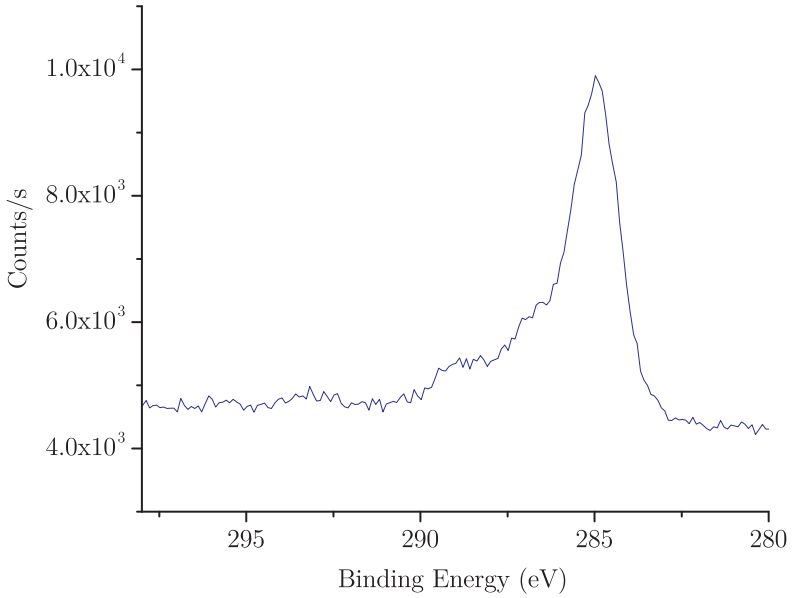

Figure 6.30: A) XPS spectrum of a used platinised titanium mesh with its characteristic peaks B) Pt 4f spectrum C) C 1s spectrum of a used platinised titanium mesh facing the Nafion membrane.

Finally Fig. 6.31 A depicts the used platinised mesh that was facing the titanium flow channel plate during testing. Compared to the used sample facing the membrane, no large regions of the dark carbon deposit is observed on the mesh. Instead small particles (tens of microns) of black residue can be seen. It should be noted that the streaks observed on the image are not due to degradation during the use of the mesh but during sample preparation for SEM imaging. On going to $\times$ 1000 magnification (Fig. 6.31 B), that same black phase observed previously can be identified again. EDX analysis on the points numbered 1 and 2 on 6.31 C, gave very similar results to the used sample discussed above. XPS analysis did not reveal any significant changes in the surface composition, as can be seen from the atomic composition data presented in Table 6.3.

A

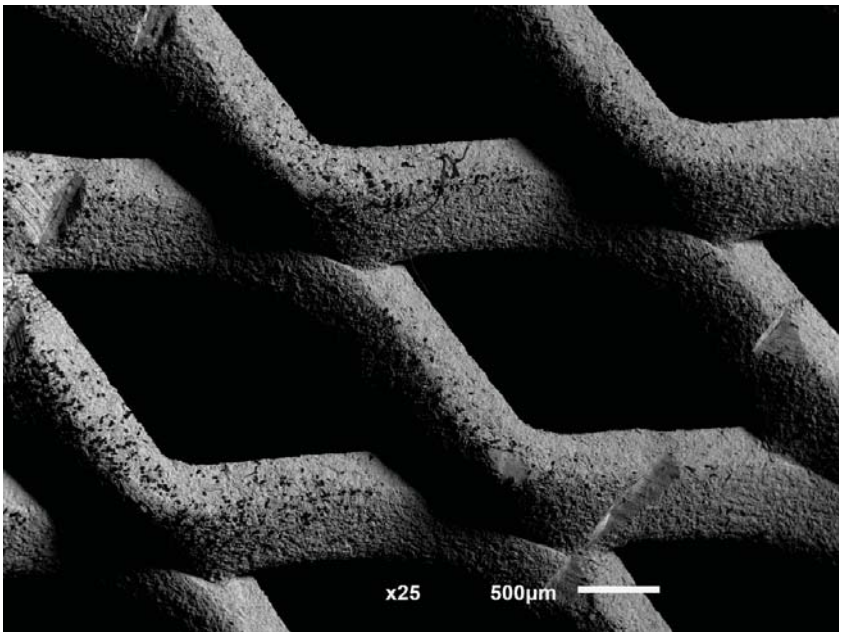

B

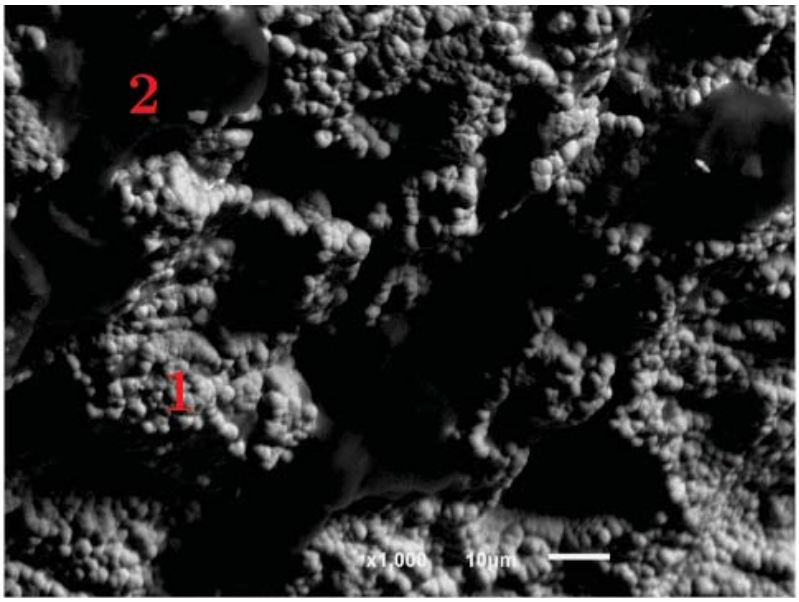

Figure 6.31: A) SEM image of a used platinised titanium mesh at × 25 magnification B) SEM image of a used platinised titanium mesh at × 1000 magnification where 1 and 2 indicates points where EDX data was collected.

6.3 Conclusions

In this chapter, the feasibility of a novel RHCFC was demonstrated. The experiments highlighted the asymmetry between charging and discharging the cell, where the charging step is limited due to the contribution of the oxygen evolution reaction at high voltages. However a peak power

density of 148 mW cm^{-2} was achieved at 100 % SOC, demonstrating promising results for a proof-of-concept cell. It was also identified from whole cell EIS measurements carried out at OCV and under load that the RHCFC is suffering from high mass transport losses related to the catholyte.

Next the Gen2 cell was built to accommodate a non-disruptive reference electrode (RE) which was presented in Chapter 4, and successfully tested on the RHVFC in Chapter 5. Using the RE, half-cell measurements could be collected thus allowing decoupling of some of the processes taking place. It was first demonstrated that the Gen2 cell could be successfully charged and discharged at current densities up to 40 mW cm^{-2}. However the results show that a maximum of only 73 % of the available theoretical capacity can be accessed when charged at 5 mA cm^{-2}. This under-utilisation of the cerium electrolyte represent a challenge to overcome if the RHCFC is to be further developed. Energy efficiencies between 85 to 71 % were observed when charging at current densities up to 20 mA cm^{-2}. Looking at the decoupled polarisation data, it is clear that the performance of the cell is limited by the cathode which suffers large diffusion losses as the current density increases. However, by replacing the graphite flow channel plates with titanium ones in Gen2, a peak power density of 198 mW cm^{-2} was achieved, showing an improved performance compared to the Gen1 cell.

From CV data it was observed that no anodic peak could be seen (Ce(III) to Ce(IV) reaction). This reaffirms that the charging step suffers from the oxygen evolution reaction, but also that the cerium redox reaction shows poor reversibility. Diffusion coefficients from the cathodic peak were calculated for the Ce (IV) ions which ranged between 4.6–5.6 $\times 10^{-6}$ cm^2 s^{-1} for scan rates going from 10 to 50 mV/s.

From combining polarisation data obtained at 90 % SOC and EIS under load measurements it was possible to show some sources of overpotential losses for the RHCFC. As expected, the major contributors to losses of the whole cell are the cerium charge transfer and diffusion resistances. As seen from CV and charging/discharging experiments the cerium reaction shows poor kinetics which translates into high charge transfer resistance. The solubility of both Ce (III) and Ce (IV) ions in acidic media is limited, leading to a high dependence of the RHCFC on the catholyte flow rate.

Additionally, EIS tests at OCV at various SOCs lead to the conclusion that the cell presents the largest overall resistance at 0 % SOC followed by 100 % SOC. Thus in order to improve losses it is best to operate the RHCFC in mid-range SOCs in the future.

Finally from imaging and surface characterisation techniques the presence of carbon deposits were observed on fresh samples, which increase after use. It was also demonstrated that the platinum does not oxidise during use and that the additional phase observed is made of carbon rather than carbon based oxides. More of this phase was observed on the mesh facing the Nafion membrane rather the titanium flow channel plate. Further work is necessary in order to understand the cause and risks of these impurities being present.

References

[1] H. Hewa Dewage, B. Wu, A. Tsoi, V. Yufit, G. Offer and N. Brandon, *J. Mater. Chem. A*, 2015, **3**, 9446–9450.

[2] J.-L. Burgot, *Ionic Equilibria in Analytical Chemistry*, Springer, Springer edn., 2012, p. 227.

[3] P. Trinidad, C. P. de León and F. C. Walsh, *Journal of environmental management*, 2008, **88**, 1417–25.

[4] P. Leung, C. Ponce de León, C. Low and F. Walsh, *Electrochimica Acta*, 2011, **56**, 2145–2153.

[5] Z. Xie, D. Zhou, F. Xiong, S. Zhang and K. Huang, *Journal of Rare Earths*, 2011, **29**, 567–573.

[6] G. Nikiforidis, L. Berlouis, D. Hall and D. Hodgson, *Electrochimica Acta*, 2014, **115**, 621–629.

[7] V. Devadoss, C. A. Basha and K. Jayaraman, *Industrial & Engineering Chemistry Research*, 2008, **47**, 4607–4616.

[8] T. Vijayabarathi, D. Velayutham and M. Noel, *Journal of Applied Electrochemistry*, **31**, 979–986.

[9] O. Himanen, T. Hottinen, M. Mikkola and V. Saarinen, *Electrochimica Acta*, 2006, **52**, 206–214.

[10] C.-N. Sun, F. M. Delnick, D. S. Aaron, A. B. Papandrew, M. M. Mench and T. A. Zawodzinski, *ECS Electrochemistry Letters*, 2013, **2**, A43–A45.

[11] P. Leung, C. Ponce-de León, C. Low, A. Shah and F. Walsh, *Journal of Power Sources*, 2011, **196**, 5174–5185.

[12] H. Kuhn, B. Andreaus, A. Wokaun and G. Scherer, *Electrochimica Acta*, 2006, **51**, 1622–1628.

[13] H. Hewa Dewage, V. Yufit and N. P. Brandon, *Journal of The Electrochemical Society*, 2015, **163**, A5236–A5243.

[14] I. A. Schneider, H. Kuhn, A. Wokaun and G. G. Scherer, *Journal of The Electrochemical Society*, 2005, **152**, A2092.

[15] V. F. Lvovich, *Impedance Spectroscopy: Applications to Electrochemical and Dielectric Phenomena*, Wiley, 2012.

[16] P. Leung, X. Li, C. Ponce de León, L. Berlouis, C. T. J. Low and F. C. Walsh, *RSC Advances*, 2012, **2**, 10125.

Chapter 7

Conclusions

This thesis describes the investigation of hydrogen based redox flow batteries, more specifically a novel Regenerative Hydrogen Vanadium Fuel Cell (RHVFC) and Regenerative Hydrogen Cerium Fuel Cell (RHCFC). Firstly a new reference electrode positioning method has been developed in order to decouple anode and cathode processes in RFBs. Secondly this work seeks to understand further the RHVFC by identifying the processes and losses occurring in the cell using this alternative reference electrode positioning method. Finally, the RHCFC was developed and characterised in this study.

7.1 Reference electrode positioning method

Following a discussion on current reference electrode (RE) positioning methods in RFBs and PEMFCs, it was identified that the sandwich and edge type RE positioning methods are the two mainstream methods used. However the sandwich method presents drawbacks such as an increase of ohmic losses by the insertion of a secondary membrane into the cell, as well as disturbing the transport of species in the membrane. The edge method suffers from the dehydration of the membrane region in contact with the RE leading to a poor inonic conducting path between the membrane and the RE. Additionally this set-up can also suffer from non-uniform current distribution due to edge effects.

Thus an alternative reference electrode positioning method using a salt bridge between the membrane and the reference electrode container was designed. This method affects neither the

operation of the cell nor the measurements collected. By collecting distinctive half-cell EIS spectra for cathode, anode and the whole cell, as well as correlating the EIS data with DC data, the successful operation of the RE set-up was established.

7.2 RHVFC

Using the new reference electrode set-up, the processes occurring within the RHVFC were decoupled, and the obtained EIS data was fitted using equivalent circuit models to establish the meaning of the different processes.

From the experiments it was concluded that the cathode diffusion and ohmic losses represent the largest contribution to irreversible losses in the RHVFC. Vanadium crossover to the anode could be detected through vanadium adsorption onto the platinum catalyst. Finally, it has been demonstrated that both the anolyte flow rate and the anolyte composition (*i.e.* hydrogen and nitrogen mixtures) have only minor effects on the cell in comparison with the catholyte flow rate and/or catholyte composition (*i.e.* different vanadium and sulphuric acid concentration). There is potential to minimize these losses by optimizing the catholyte composition, as a balance must be found between acid and vanadium concentration in order to avoid membrane dehydration, large diffusion losses due to high viscosity of the electrolyte, or excess vanadium cross over. This work also suggests that minimising vanadium crossover through improved ion selectivity of the membrane is crucial as the long term effect of vanadium on the hydrogen electrode is not yet understood.

7.3 RHCFC

The feasibility of a novel RHCFC was demonstrated. The initial experiments highlighted the asymmetry between the charging and discharging of the cell, where the charging step is limited due to the contribution of the oxygen evolution reaction at high voltages. However a peak power density of 148 $\mathrm{mW\,cm^{-2}}$ was achieved at 100 % SOC, demonstrating promising results for a proof-of-concept cell. It was also identified from whole cell EIS carried out at OCV and under load that the RHCFC was suffering from high mass transport losses related to its catholyte.

Next an optimised cell was built to accommodate the new RE set-up. Using the RE, similarly to the RHVFC, half-cell measurements could be collected allowing the irreversible losses in the cell to be identified. It was first demonstrated that the optimised cell could be successfully charged and discharged at current densities up to 40 $mA\,cm^{-2}$. However the results showed that only a maximum of 73 % of the available theoretical capacity could be accessed when charged at a current density as low as 5 $mA\,cm^{-2}$. This underutilisation of the cerium electrolyte represent a challenge to overcome if the RHCFC is be commercialised. Energy efficiencies between 85 to 71 % were observed when charging at current densities up to 20 $mA\,cm^{-2}$. Looking at the decoupled polarisation data, it was confirmed that the performance of the cell was limited by the cathode that suffers large diffusion losses as the current density increases. However, by replacing the graphite flow channel plates with titanium ones in a new cell, a peak power density of 198 $mW\,cm^{-2}$ was achieved showing improved performance.

From cyclic voltammetry data is was evident that no anodic peak could be resolved, indicating that the charging step occurs in parallel with oxygen evolution reaction, and that the cerium redox reaction shows poor reversibility.

By combining polarisation data obtained at 90 % SOC and EIS under load measurements it was possible to show some sources of overpotential for the RHCFC. As expected the major contributors to losses of the whole cell are the cerium charge transfer and diffusion resistances. As seen from cyclic voltammetry and charging/discharging experiments the cerium reaction shows poor kinetics which translates into high charge transfer resistance. The solubility of both Ce (III) and Ce (IV) ions in acidic media is relatively low (1 M for both Ce(III) and Ce(IV) ions in 4 M MSA at room temperature[1]), leading to a high dependence of the RHCFC on the catholyte flow rate thus high diffusion losses.

Additionally, EIS tests at OCV at various SOCs lead to the conclusion that the RHCFC presents the largest overall resistance at 0 % SOC followed by 100 % SOC. Hence in order to improve losses it is best to operate the RHCFC in the mid-range SOCs in the future.

Finally from imaging and surface characterisation techniques carbon deposits were seen on fresh electrode surfaces, which seemed to increase after use. It was also demonstrated that the platinum does not oxidise during use and that the deposits are of carbon rather than

carbon based oxides. At last, more of these deposits were observed on the mesh facing the Nafion membrane rather the titanium flow channel plate. Further work is necessary in order to understand the cause and implications of these.

7.4 Future work

Future work for the RHVFC can look into optimising the cathode electrode structure to enhance mass transport to and within the electrode. Improving the cell design for the next RHVFC generation in order to minimise high ohmic losses due to poor current collection is crucial. Such a cell would deliver better performance overall and EIS under load tests would provide insight into the losses under such conditions. Additionally it is necessary to understand the performance and losses of individual cells in a RHVFC stack. The RE set-up could be redesigned for application in a stack, making it a useful tool not only to understand electrochemical processes as the single cell level but disparities between cells in an RFB stack.

It is evident from the optimised RHCFC that the cerium cathode remains the limiting electrode. Thus work needs to be done to improve the electrodes used on the cathode. This may involve finer meshes, alternative catalyst or even well engineered structures produced from metal laser sintering of titanium. Secondly the catholyte could include current promising additives presented in the literature in order to improve the reversibility of the cerium reaction (*ie.*: sulfosalicyclic acid, ethylenediaminetetraacetic, diethylenetriaminepentaacetate, etc.)[2]

Further work needs to be done using EIS under load and correlating this to polarisation experiments. Unfortunately it is harder to undertake EIS under load at high current densities. However if enough measurements are collected, across the possible current density range, the resistance values could be meaningfully fitted with a function so values at higher current densities could be extrapolated.

For both RHVFC and RHCFC, although the hydrogen anode is not the limiting electrode, it would be useful to understand better the long term effects of catholyte crossover to the hydrogen side. It is necessary to cycle these cells to make sure that no new sources of losses appear over time.

7.5 Dissemination

Papers

H. Hewa Dewage, B. Wu, A. Tsoi, V. Yufit, G. Offer, and N. Brandon, "A novel regenerative hydrogen cerium fuel cell for energy storage applications", *J. Mater. Chem. A*, vol. 3, no. 18, pp. 94469450, Apr. 2015.

H. H. Dewage, V. Yufit, and N. P. Brandon, "Study of Loss Mechanisms Using Half-Cell Measurements in a Regenerative Hydrogen Vanadium Fuel Cell", *J. Electrochem. Soc.*, vol. 163, no. 1, pp. A5236A5243, Dec. 2015.

In preparation

H. Hewa Dewage, G. Owen-Jones, V. Yufit, I. Villar-Garcia and N. P. Brandon, "Optimisation and Investigation of Half-Cell Losses in a Hydrogen-Cerium Redox Flow Battery", *In preparation.*

Conference presentations by the author

H. Hewa Dewage, V. Yufit, and N. P. Brandon *"Study of Loss Mechanisms in a Regenerative Hydrogen Vanadium Fuel Cell"*, International Flow Battery Forum 2014 (July, Hamburg).

V. Yufit, **H. Hewa Dewage**, B. Wu, F. Tariq, S.J. Cooper, and N. Brandon *"Study of Loss Mechanisms in a Regenerative Hydrogen VanadiumFuel Cells"*, ECS 226th Meeting (October 2014, Cancun).

H. Hewa Dewage, V. Yufit, B. Wu, A. Tsoi, G. Offer, and N. Brandon *"Study of Loss Mechanisms in Regenerative Hydrogen based Fuel Cells"*, UK Energy Storage 2014 (November, Warwick).

H. Hewa Dewage, V. Yufit, B. Wu, A. Tsoi, G. Offer, and N. Brandon *"Study of Loss Mechanisms in Regenerative Hydrogen based Fuel Cells"*, MRS Fall 2014 (December, Boston).

H. Hewa Dewage, V. Yufit, B. Wu, A. Tsoi, G. Offer, and N. Brandon *"Study of Loss Mechanisms in Regenerative Hydrogen based Fuel Cells"*, Early Career Reaserchers Conference 2015 (April, Abingdon).

H. Hewa Dewage, V. Yufit, B. Wu, A. Tsoi, G. Offer, and N. Brandon *"Study of Loss*

Mechanisms in Regenerative Hydrogen based Fuel Cells", International Flow Battery Forum 2015 (June, Glasgow).

V. Yufit, **H. Hewa Dewage** and N. Brandon *"Regenerative Fuel Cells for Energy Storage Application: Performance Limitation Studies"*, ECS Conference on Electrochemical Energy Conversion & Storage with SOFC-XIV (July 2015, Glasgow).

Posters

H. Hewa Dewage, V. Yufit, B. Hale, M. Matian, P. Mazur and N.P. Brandon *"Performance Optimisation of a Regenerative Hydrogen-Vanadium Fuel Cell for Energy Storage Applications"*, ModVal 11 (March 2014, Winterthur).

H. Hewa Dewage, G. Owen-Jones, V. Yufit and N.P. Brandon *"Go with the Flow. Investigation of the Positive and Negative Half-Cells in a Regenerative Hydrogen Cerium Fuel Cell"*, ECS 226th Meeting (November, Birmingham)

References

[1] P. Leung, C. Ponce-de León, C. Low, A. Shah and F. Walsh, *Journal of Power Sources*, 2011, **196**, 5174–5185.

[2] Z. Xie, Q. Liu, Z. Chang and X. Zhang, *Electrochimica Acta*, 2013, **90**, 695–704.